

# **Heterogeneous nature of the carbonaceous chondrite breccia Aguas Zarcas – cosmochemical characterization and origin of new carbonaceous chondrite lithologies**

Imene Kerraouch<sup>1,2</sup>, Yoko Kebukawa<sup>3</sup>, Addi Bischoff<sup>1</sup>, Michael E. Zolensky<sup>2</sup>, Elias Wölfer<sup>1</sup>,  
Jan L. Hellmann<sup>1</sup>, Motoo Ito<sup>4</sup>, Ashley King<sup>5</sup>, Mario Trierhoff<sup>6</sup>, Jean-Alix Barrat<sup>7</sup>, Phillipe  
Schmitt-Kopplin<sup>8,9</sup>, Andreas Pack<sup>10</sup>, Markus Patzek<sup>1</sup>, Romy D. Hanna<sup>11</sup>, Thomas  
Fockenberg<sup>12</sup>, Yves Marrocchi<sup>13</sup>, Marc Fries<sup>2</sup>, Jérémie Mathurin<sup>14</sup>, Emmanuel Dartois<sup>15</sup>, Jean  
Duprat<sup>16</sup>, Cécile Engrand<sup>17</sup>, Ariane Deniset<sup>18</sup>, Alexandre Dazzi<sup>18</sup>, Kento Kiryu<sup>3</sup>, Motoko  
Igisu<sup>19</sup>, Takazo Shibuya<sup>19</sup>, Daisuke Wakabayashi<sup>20</sup>, Shohei Yamashita<sup>20</sup>, Yasuo Takeichi<sup>20</sup>,  
Yoshio Takahashi<sup>21</sup>, Takuji Ohigashi<sup>22</sup>, Yu Kodama<sup>23</sup>, Masashi Kondo<sup>24</sup>.

<sup>1</sup>Institut für Planetologie, University of Münster, Wilhelm-Klemm-Str. 10, D-48149 Münster,  
Germany.

<sup>2</sup>Astromaterials Research and Exploration Science, NASA Johnson Space Center, Houston  
TX, 77058, USA.

<sup>3</sup>Graduate School of Engineering Science, Yokohama National University, 79-5 Tokiwadai,  
Hodogaya-ku, Yokohama 240-8501, Japan.

<sup>4</sup>Kochi Institute for Core Sample Research, JAMSTEC, B200 Monobe, Nankoku, Kochi 783-  
8502, Japan.

<sup>5</sup>Planetary Materials Group, Department of Earth Sciences, Natural History Museum, Cromwell Road,  
London, SW7 5BD, UK.

<sup>6</sup>Klaus-Tschira-Labor für Kosmochemie, Institut für Geowissenschaften, Universität  
Heidelberg, Im Neuenheimer Feld 234-236, 69120 Heidelberg, Germany.

<sup>7</sup>Université de Bretagne Occidentale, Institut Universitaire Européen de la Mer, Place Nicolas  
Copernic, F-29280 Plouzané Cedex, France.

<sup>8</sup>Helmholtz Zentrum Muenchen - German Research Center for Environmental Health,  
Research Unit Analytical BioGeoChemistry, D-85764 Neuherberg, Germany

<sup>9</sup>Technische Universität München, Chair of Analytical Food Chemistry, D85354, Freising-  
Weihenstephan, Germany

<sup>10</sup>Universität Göttingen, Geowissenschaftliches Zentrum, Goldschmidtstr. 1, D-37077  
Göttingen, Germany.

<sup>11</sup>Jackson School of Geosciences, University of Texas, Austin, TX, USA.

<sup>12</sup>Institut für Geologie, Mineralogie und Geophysik, Ruhr-Universität Bochum, D-44780  
Bochum, Germany.

- 34 <sup>13</sup>Université de Lorraine, CNRS, CRPG, UMR 7358, Vandœuvre-lès-Nancy, 54501, France.
- 35 <sup>14</sup>Université Paris-Saclay, CNRS/IN2P3, IJCLab, 91405 Orsay, France. Université Paris-  
36 Saclay, CNRS, Institut de Chimie Physique, UMR 8000, 91405, Orsay, France.
- 37 <sup>15</sup>Institut des Sciences Moléculaires d'Orsay, UMR8214, CNRS, Université Paris-Saclay,  
38 91405 Orsay, France
- 39 <sup>16</sup>Institut de Minéralogie, de Physique des Matériaux et de Cosmochimie, CNRS-MNHN-  
40 Sorbonne Université, 57 rue Cuvier 75005 Paris, France
- 41 <sup>17</sup>Université Paris-Saclay, CNRS/IN2P3, IJCLab, 91405 Orsay, France
- 42 <sup>18</sup>Université Paris-Saclay, CNRS, Institut de Chimie Physique, UMR 8000, 91405, Orsay,  
43 France
- 44 <sup>19</sup>Super-cutting-edge Grand and Advanced Research (Sugar) Program, Institute for Extra-  
45 cutting-edge Science and Technology Avant-garde Research (X-star), Japan Agency for  
46 Marine-Earth Science and Technology (JAMSTEC), 2-15 Natsushima-cho, Yokosuka 237-  
47 0061, Japan.
- 48 <sup>20</sup>Institute of Materials Structure Science, High-Energy Accelerator Research Organization, 1-  
49 1 Oho, Tsukuba, Ibaraki 305-0801, Japan.
- 50 <sup>21</sup>Department of Earth and Planetary Science, The University of Tokyo, Hongo, Bunkyo-ku,  
51 Tokyo 113-0033, Japan
- 52 <sup>22</sup>UVSOR Synchrotron, Institute for Molecular Science, 38 Nishigo-Naka, Myodaiji, Okazaki,  
53 444-8585, Japan
- 54 <sup>23</sup>Marine Works Japan Ltd., B200 Monobe, Nankoku, Kochi 783-8502, Japan
- 55 <sup>24</sup>Instrumental Analysis Center, Yokohama National University, 79-5 Tokiwadai, Hodogaya-  
56 ku, Yokohama 240-8501, Japan.
- 57 ***Corresponding author:*** Imene Kerraouch, Institut für Planetologie, University  
58 of Münster, Wilhelm-Klemm-Str. 10, D-48149 Münster, Germany. Phone: +49-  
59 170 6012357; E-mail: "ikerraou@uni-muenster.de"

## Abstract

On April 23rd, 2019, the Aguas Zarcas meteorite fall occurred in Costa Rica. Because the meteorite was quickly recovered, it contains valuable extraterrestrial materials that have not been contaminated by terrestrial processes. Our X-ray computed tomography (XCT) and scanning electron microscopy (SEM) results on various pre-rain fragments from earlier work (Kerraouch et al., 2020; 2021) revealed several distinct lithologies: Two distinct metal-rich lithologies (Met-1 and Met-2), a CM1/2 lithology, a C1 lithology, and a brecciated CM2 lithology consisting of different petrologic types. Here, we further examined these lithologies in the brecciated Aguas Zarcas meteorite and report new detailed mineralogical, chemical, isotopic, and organic matter characteristics. In addition to petrographic differences, the lithologies also display different chemical and isotopic compositions. The variations in their bulk oxygen isotopic compositions indicate that the various lithologies formed in different environments and/or under diverse conditions (e.g., water/rock ratios). Each lithology experienced a different hydration period during its evolution. Together, this suggests that multiple precursor parent bodies may have been involved in these processes of impact brecciation, mixing, and re-assembly. The Cr and Ti isotopic data for both the CM1/2 and Met-1 lithology are consistent with those of other CM chondrites, even though Met-1 displays a significantly lower  $\epsilon^{50}\text{Ti}$  isotopic composition that may be attributable to sample heterogeneities on the bulk meteorite scale and may reflect variable abundances of refractory phases in the different lithologies of Aguas Zarcas. Finally, examination of the organic matter of the various lithologies also suggests no strong evidence of thermal events, but a short-term heating cannot completely be excluded. Raman parameters indicate that the peak temperature has been lower than that for Yamato-793321 (CM2,  $\sim 400^\circ\text{C}$ ). Considering the new information presented in this study, we now better understand the origin and formation history of the Aguas Zarcas daughter body.

**Keywords:** Aguas Zarcas; Carbonaceous chondrites; Metal-rich lithology; Cr, Ti, Te isotopes; Organic matter.

## 88        **1. Introduction**

89            Carbonaceous chondrites are samples of primitive asteroids formed during the early  
90 Solar System, and thus they can provide insights into the Solar System's early history (e.g.,  
91 Anders and Grevesse 1989; Wasson and Kallemeyn 1988; Greenwood et al., 2020). They  
92 make up only 3.8% of the meteorites collected after being seen to fall to Earth (The  
93 Meteoritical Bulletin). They are crucial to understanding the transport of water and organic  
94 matter into the region of terrestrial planet formation in the early Solar System due to their  
95 diverse extraterrestrial chemistry and abundance of hydrated minerals. Like other chondrites,  
96 carbonaceous chondrites have experienced a wide range of processes, such as various degrees  
97 of aqueous alteration, thermal metamorphism, brecciation, or a combination thereof (e.g.,  
98 Grimm and McSween, 1989; Metzler et al., 1992; Zolensky et al., 1993; Browning et al.,  
99 1996; Brearley and Jones 1998; Nakamura et al., 2005; Bischoff et al., 2006; Brearley, 2006;  
100 Lentfort et al., 2021). While these processes provide important information about the  
101 environment of the chondrites' evolution, evidence for these processes is often not well  
102 preserved because they are highly susceptible to weathering, meaning most of them have been  
103 modified to some extent by the terrestrial environment.

104            The Aguas Zarcas meteorite fell at 21:07 local time on 23rd April 2019 in Aguas  
105 Zarcas, San Carlos County, Alajuela province, Costa Rica. It is a brecciated carbonaceous  
106 chondrite with a total mass of at least 27 kg. The rapid recovery of the Aguas Zarcas  
107 meteorite after its fall provides an opportunity to investigate a freshly fallen, least  
108 contaminated, highly brecciated meteorite. The large Aguas Zarcas fall delivered a wide  
109 variety of carbonaceous chondrite lithologies, some of which are familiar as CM lithologies  
110 (Pizzarello et al., 2020; Garvie, 2021), but others are unique, and thus offer an important  
111 opportunity to explore the history of their formation (Kerrouch et al., 2020; 2021). An earlier  
112 study by Kerrouch et al., (2021), based on petrographic and mineralogical descriptions and  
113 oxygen isotope data of several fragments of the Aguas Zarcas meteorite, revealed new  
114 lithologies that have some unique characteristics and, therefore, were pursued further  
115 examination in order to provide more information about this fascinating breccia.

116            From our previous work, we have classified the Met-1 as a new and unique  
117 carbonaceous chondrite lithology which bears similarities to CR and CM chondrite groups,  
118 but it is distinct from both based on oxygen isotope data. Furthermore, Met-1 contains a high  
119 abundance of metal (kamacite and taenite), suggesting a relatively low degree of aqueous  
120 alteration, but also a high overall abundance of phyllosilicates and carbonates that implies this  
121 lithology has undergone a moderate to high degree of aqueous alteration. Met-2 also

represents a new type of carbonaceous chondrite with a higher abundance of metal and sulfides. The Met-1 and Met-2 lithologies showed some similarities but are distinct. The C1 and CM1/2 Aguas Zarcas lithologies are very altered and possibly related to the CM chondrite group. The brecciated CM lithology has two primary components: a chondrule-poor lithology and a chondrule-rich lithology showing different petrologic subtypes (from 2.1 to 2.8; e.g., Rubin et al., (2007); Bischoff et al., (2017); Lentfort et al., (2021)).

In this study, we present new details regarding the mineralogy, chemistry, isotopic compositions, and soluble organic components of the different lithologies in Aguas Zarcas. Based on these characteristics we discuss the alteration history of the lithologies, their affinities with other carbonaceous chondrite groups, and the origin and evolution of the Aguas Zarcas parent body. Overall, this study sheds new light on the large petrological diversity and processing of hydrous carbonaceous asteroids in the early Solar System.

## 2. Samples and analytical methods

Many fragments were recovered after the fall of the breccia Aguas Zarcas, some before and some after rainfall. In this study, we investigate several pre-rain samples that contain five different lithologies that were identified in our previous study (Kerraouch et al., 2021) of this brecciated chondrite: (1) Met-1, a metal-rich lithology, (2) Met-2, a second metal-rich lithology, (3) a CM1/2 lithology, (4) a C1 lithology, and (5) some fragments and clasts of typical CM2 chondrite lithology (clasts from section PL19111: CM-clast1, CM-clast2 and CM-clast3; which are associated with Met-1; Fig. 1c, and CM fragment from CR19-001). PL91165 thin section from CR chondrite (Acfer 209) is used here for comparison.

Different analytical methods were applied to analyze and characterize each lithology. We briefly summarize hereafter the methods applied; further details are included in the Supplementary Material (SM). Due to insufficient quantities for some samples, we were not able to perform all of the analyses cited below for each of the five lithologies studied. Table 1 summarizes the different lithologies of Aguas Zarcas studied together with the corresponding analyses performed.

We studied bulk powders and several thick and thin sections of Aguas Zarcas: PL19111, PL19112, PL19125, and PL22032 prepared from the fragment #MS-2 (MS = Münster), a 2.5-g pre-rain fragment at the Institut für Planetologie (IfP), University of Münster. Polished mounts of separate pre-rain stones provided by Robert Ward, called JSC-Mount1, JSC-Mount2, and JSC-Mount3, were provided by the Astromaterials Research and Exploration Science (ARES), NASA Johnson Space Center. Additionally, two pre-rain samples #CR19.19 (section PL19149) and #CR19.29 were provided by Robert Ward.

All sections were characterized by Scanning Electron Microscopy with Energy Dispersive Spectroscopy (SEM/EDS) at the IfP and at the E-Beam Laboratories of ARES, NASA JSC. Quantitative mineral analyses were obtained using a JEOL JXA 8530F electron microprobe (EPMA) Institut für Mineralogie (University of Münster) and a JEOL 8530-FE electron microprobe at ARES. The mineralogy of Met-1 lithology was also characterized using a PANalytical X'Pert Pro scanning X-ray diffractometer (XRD) and position-sensitive-detector (PSD) XRD at the Natural History Museum (NHM), London.

We subsequently measured the oxygen isotopic compositions of several calcite grains in PL19111 (Met-1 and the CM-clasts) and PL19149 (CM1/2 lithology). The in-situ oxygen isotope analyses were carried out using the Heidelberg Ion Probe (Cameca IMS 1280-HR) at the Institute of Earth Sciences, Heidelberg University. We have also performed Mn-Cr

isotope analyses of the carbonates by ion probe (SIMS), but these did not yield resolvable Cr isotopic anomalies.

Several aliquots of bulk powder of the Met-1 sample were used to determine the bulk water/OH content and carbon concentration of the Met-1 lithology (#MS-2) at the Institute for Geology, Mineralogy and Geophysics, Ruhr-University Bochum using a Mitsubishi CA 200 moisture meter. Trace element compositions of the Met-1 and CM1/2 samples were obtained using Inductively Coupled Plasma Atomic Emission Spectroscopy (ICP-AES) and Inductively Coupled Plasma Sector Field Mass Spectrometry (ICP-SFMS) at the Institut Universitaire Européen de la Mer, Université de Bretagne Occidentale in Plouzané, France.

Titanium and chromium isotope analyses of the Met-1 and CM1/2 lithologies were performed on the Thermo Scientific Neptune *Plus* MC-ICPMS at the IfP. The analytical procedures followed previously established routines (Zhang et al., 2011; Gerber et al., 2017 for Ti; Trinquier et al., 2008a,b; Yamakawa et al., 2009; Schneider et al., 2020 for Cr). Ti and Cr isotope anomalies are reported as  $\epsilon$ -values (parts-per-10<sup>4</sup> deviations from terrestrial standard values) after internal normalization of measured isotope ratios to  $^{49}\text{Ti}/^{47}\text{Ti} = 0.749766$  and  $^{50}\text{Cr}/^{52}\text{Cr} = 0.051859$ , respectively. A detailed description of the chemical purification and isotope measurements of Ti and Cr is provided in the SM. The mass-dependent tellurium isotopic composition of a ~70-mg aliquot from the Met-1 sample powder was determined by applying a  $^{123}\text{Te}$ – $^{125}\text{Te}$  double spike method (Hellmann et al., 2020) and using a Thermo Scientific Neptune *Plus* MC-ICPMS at the IfP. Analytical procedures followed previously established routines by Hellmann et al., (2020). Results are reported as  $\delta^{128/126}\text{Te}$  values (per-mil deviation from the NIST SRM 3156 standard solution).

Finally, we studied the organic matter (OM) in Met-1, Met-2, C1, and CM lithologies using different methods. A small fragment of Met-1 was sent to the Research Center for Environmental Health, Munich, Germany, and studied by soluble organic matter (SOM) analysis. Subsamples of Met-2, C1, and CM lithologies (CM from CR19.01) were sent to Yokohama National University (YNU), Japan, and then studied by a combination of several methods involving multiple institutions for microscopic analyses of organic matter.

The SOM content of small fragments of the Met-1 lithology was analyzed following the same procedures used previously to enable a comparison of the compositional profiles (Schmitt-Kopplin et al., 2010; Popova et al., 2013), and the data were obtained from a solid specimen with a weight of 2 milligrams.

Raman analysis and peak fitting were conducted following the procedure described in Kiryu et al., (2020). Small fragments of Met-2, the CM lithology (CR19.01), and the C1

lithology were pressed onto clean Au or KBr substrates and analyzed using a Raman microspectrometer (RAMANtouch; Nanophoton) at JAMSTEC, Yokosuka, with a 532 nm laser. Raman mapping measurements were also performed on the same microtome section as the one used for AFM-IR measurements (see AFM-IR section and SM).

Fourier Transform Infrared Spectroscopy (FTIR) analysis was conducted following the procedure described in Kebukawa et al., (2020). Small particles (a few 100  $\mu\text{m}$ ) of the Met-2, CM, and C1 lithologies were pressed onto KBr plates ( $\sim 5 \times 5 \times 1 \text{ mm}^3$ ). IR absorption spectra were collected at Yokohama National University using a micro-FTIR (JASCO FT/IR-6100+IRT-5200) equipped with a ceramic IR light source, a germanium-coated KBr beam splitter, a mercury-cadmium-telluride (MCT) detector, and  $\times 16$  Cassegrain mirrors.

Sulfur-embedded ultramicrotomed thin sections ( $\sim$  few 100 nm-thick) from the CM lithology (CR19-001) were prepared for atomic force microscope-infrared spectroscopy (AFM-IR). We then performed AFM-IR analysis using a NanoIR2 system from Bruker at the Institut de Chimie Physique, CNRS, Université Paris-Saclay, France. In such a setup, the IR laser was focused on the top side of the sample probed by the the AFM cantilever.

We also selected typical areas in the Met-2, CM, and C1 lithologies for preparing ultra-thin sections utilizing two focused ion beams (FIBs; Hitachi Tech SMI-4050 and SMJ-4000L) at the Kochi Institute of Core Sample Research, JAMSTEC. Subsequently, these sections were transferred into a FIB-SEM SMJ-4000L to remove damaged layers on the surface of the sections with a broad Ar-ion beam at 1 kV. Carbon X-ray absorption near-edge structure (C-XANES) analyses were performed using the scanning transmission X-ray microscopes (STXM) at BL-19A of the Photon Factory, High Energy Accelerator Research Organization (KEK) (Takeichi et al., 2016) and the STXM beam line, BL4U, at the UVSOR Synchrotron Facility, Institute for Molecular Science (Ohgashi et al., 2013).

Small fragments from the Met-2 and C1 lithologies were pressed onto 00 Au thin foil or KBr plates, and matrix areas on the thin sections were chosen for analysis by a raster ion imaging with the JAMSTEC NanoSIMS 50L at the Kochi Institute for Core Sample Research, JAMSTEC. The  $^{12}\text{C}$ ,  $^{13}\text{C}$ ,  $^{16}\text{O}$ ,  $^{12}\text{C}^{14}\text{N}$ ,  $^{12}\text{C}^{15}\text{N}$  and  $^{32}\text{S}$  were measured as negative secondary ions simultaneously in six electron multipliers. In a separate analysis, the H isotopes ( $^1\text{H}$  and  $^2\text{D}$ ) and  $^{12}\text{C}$  were subsequently measured as negative secondary ions together with secondary electrons. The OM regions were chosen by noting distributions of  $^{12}\text{C}$  within a section applying a 10% threshold of total  $^{12}\text{C}$  ion counts. The H, C and N isotopic compositions of OM in the measured areas were calculated following analytical routines using a standard organic material (1-hydroxybenzotriazole hydrate;  $\text{C}_6\text{H}_5\text{N}_3\text{O} \cdot x\text{H}_2\text{O}$ : HOBT) (Ito et al., 2014).



### 3. Results

#### 3.1. MINERALOGY AND PETROGRAPHY

Details of the mineralogy of the various lithologies are given in Kerraouch et al., (2021). The main results are summarized in the following paragraphs and in Table 2.

##### 3.1.1. General description of Aguas Zarcas lithologies

###### *Met-1 (Metal-rich lithology 1)*

The bulk mineralogy of the Met-1 lithology determined by PSD-XRD in this study was found to be (Fig.1a and Fig. 2) phyllosilicates (~55 vol%), olivine (~20 vol%), pyroxene (~20 vol%), magnetite (~1 vol%), metal (~2 vol%), sulfides (~1 vol%) and carbonates (~1 vol%).

Electron microscopy showed that olivine (Fa<sub>0-65</sub>), low-Ca pyroxene (Fs<sub>2.4±3.3</sub> En<sub>95.1±4.9</sub> Wo<sub>2.5±2.4</sub>) and diopside (Fs<sub>1.9±1.5</sub> En<sub>60.8±6.1</sub> Wo<sub>37.3±6.0</sub>) grains of similar compositions are found both in the chondrules and as clasts in the matrix. Isolated olivine grains in the matrix range in size from a few microns up to 100 µm. Metal grains range in size from a few microns up to 550 µm, present as kamacite and taenite, in both the chondrules and matrix. Carbonate phases occur within the matrix and in the complex Ca,Al-rich inclusions (CAIs). The chemical composition is very close to that of pure CaCO<sub>3</sub>, and Raman spectra show that it is all calcite. This is also consistent with the XRD data.

Most chondrules contain a high abundance of metal and sulfide grains either inside and/or at their edges similar to chondrules in CR2 chondrites (Weisberg et al., 1993), but on a different size scale. Chondrule sizes in Met-1 range from 14 to 800 µm. They have a mean size of about 186 µm, an abundance of ~30 vol%, and have fine-grained rims (FGRs) (e.g., Metzler et al., 1992; Metzler and Bischoff, 1996). Some chondrules are altered and partially replaced by phyllosilicates. The abundance of CAIs in the Met-1 lithology is 0.66 vol% and two types can be distinguished: (a) CAIs with a rounded shape (~80 to 140 µm in diameter), which are spinel-rich and hibonite-rich objects, and (b) irregularly-shaped CAIs (~500 µm), which are complex and unusual in mineralogy, typically composed of calcite (~53 vol%) and spinel, perovskite and sometimes with minor grossmanite. An Al-rich diopside rim of constant thickness typically surrounds these CAIs. Based on the mean TCI compositions of the Met-1 lithology, the petrologic subtype relating to the degree of aqueous alteration can be defined as 2.5 for Met-1 (Rubin et al., 2007; Lentfort et al., 2021). This value is lower than

the XRD data suggest (sub-type 1.9 (based on the scale of Howard et al., (2015), which corresponds to about 2.8 on the Rubin et al., (2007) scale).

#### *Met-2 (Metal-rich lithology 2)*

The Met-2 (Fig. 1b) lithology shows a close similarity to Met-1, but it is clearly distinct based on its higher metal and sulfide abundance (~5 vol%) and the lack of FGRs around coarse-grained components. Olivine and pyroxene were also found in the chondrules and as isolated grains in the matrix, with similar composition and grain sizes as in Met-1.

The metals are a mixture of kamacite and taenite and have similar morphologies and characteristics as in Met-1 (Fig. 3), although their sizes are smaller in Met-2 (ranging from a few microns up to 250  $\mu\text{m}$ ). The chondrules have a modal abundance of about 20 vol% and a mean diameter of 136  $\mu\text{m}$  (n=166) and are often fragmented. Considering refractory inclusions, we observed neither carbonate-rich CAIs nor fully intact CAIs. Only some Al-rich phases were detected.

#### *CM1/2 lithology*

The CM1/2 lithology (Fig. 1d) contains abundant matrix (~80 vol%) phyllosilicates with minor amounts of magnetite (<1 vol%), sulfides (<2 vol%), olivine and low-Ca pyroxene (each ~3 vol%), calcite (<2 vol%), and some metal grains. These mineral abundances are consistent with other CM1/2s analysed by PSD-XRD (e.g. King et al., 2017). The CM1/2 lithology contains highly altered chondrules, some containing relic grains of olivine (mean:  $\text{Fa}_{2.1\pm 2.1}$ ; n=7) and/or pyroxene ( $\text{Fs}_{10.8}\text{En}_{60.5}\text{Wo}_{28.7}$ ) and having a  $\text{SiO}_2$ - and S-rich mesostasis. The mean diameter of relict chondrules is 256  $\mu\text{m}$  and their abundance is ~15 vol%. The CM1/2 lithology contains one type of CAI mainly composed of spinel and phyllosilicates and surrounded by an Al-rich diopside rim. The matrix represents about 70 vol% of TCIs and consists of both Fe-rich and S-rich regions. The most abundant type of TCIs consists of acicular fibers rich in Fe, often associated with calcite. Cronstedtite appears to be the dominant phyllosilicate phase. Based on its average TCI compositions, the CM1/2 lithology shows a low petrologic subtype of 2.2 indicating a high degree of aqueous alteration (Rubin et al., 2007; Lentfort et al., 2021). In addition, most metal and pentlandite shows pre-terrestrial aqueous alteration.

#### *C1 lithology*

The C1 lithology (Fig. 1e) contains abundant matrix phyllosilicates (~90 vol.%), magnetite, sulfides, and some Ca-carbonate grains. The bulk composition of the phyllosilicates in this lithology lies between that of serpentine and saponite, but closer to the latter as is the case for CI and CR chondrites. However, in contrast to phyllosilicates in CI and CR chondrites, the FeO content is quite uniform (11-20 wt% FeO). Analytical EPMA totals for the phyllosilicates are low (65-86 wt%), as expected for fully hydrated material. Abundant framboidal to plaquette magnetites are set within the phyllosilicates as well as fine-grained pyrrhotite and pentlandite. The latter two exhibit their typical exsolution texture. This lithology contains no anhydrous silicates, chondrules, CAIs, or pseudomorphs of these objects.

### *CM lithologies*

The CM chondrite lithologies within the Aguas Zarcas meteorite occur as clasts within brecciated pieces or as the main lithology in some fragments. The olivine grains in three CM-clasts (Fig. 1c) have highly variable Fa contents (Fa<sub>0-60</sub>). All three CM clasts have mean Fs contents of ~2 mol%. The compositions are similar to those within the Met-1 and Met-2 lithologies. The CM clasts also contain some small grains (few microns) of metal and sulfides. The composition of the matrix is similar to that of serpentine (Kerraouch et al., 2021). Based on their average TCI compositions, CM-clast1 and CM-clast2 are petrologic subtype 2.6, while CM-clast 3 is the least altered and is assigned to petrologic subtype 2.8 (Rubin et al., 2007; Lentfort et al., 2021).

## 3.2. CHEMISTRY AND ISOTOPIC COMPOSITIONS

### 3.2.1. Isotopic studies on carbonates

The O isotopic compositions of the calcite grains analyzed in this study are given in Table S1 and shown in Figure 4.

Carbonates from the matrix within the Met-1 lithology plot into two groups. The first group ranges in  $\delta^{18}\text{O}_{\text{VSMOW}}$  from +16.2 to +22‰ and in  $\Delta^{17}\text{O}_{\text{VSMOW}}$  from -3.3 to -0.3‰, defining a line with a slope of  $0.19 \pm 0.26$ . The second group ranges in  $\delta^{18}\text{O}_{\text{VSMOW}}$  from +31.8 to +41.6‰ and in  $\Delta^{17}\text{O}_{\text{VSMOW}}$  from -2.7 to -0.5‰, whereby the slope is  $0.57 \pm 0.09$  (Fig. 4a). Despite falling into two isotopic groups, there is no clear petrologic difference between calcite grains of group 1 and group 2.

The calcite grains in the Met-1 CAIs are aggregates of small crystals (Fig. 5). Their  $\delta^{18}\text{O}_{\text{VSMOW}}$  and  $\Delta^{17}\text{O}_{\text{VSMOW}}$  values are less variable and plot into one group that ranges from +32.06 to +37.5‰ and from -2.7 to -0.7‰, respectively. The CAI carbonates define a line with a slope of  $0.70 \pm 0.21$  (Fig. 4b). Some spinel grains within the CAIs of Met-1 were also measured, showing low  $\delta^{18}\text{O}_{\text{VSMOW}}$  and  $\Delta^{17}\text{O}_{\text{VSMOW}}$  values (about -50‰ for both) that plot on the CCAM line.

The oxygen isotopic compositions of the calcite grains within matrices of the three different CM clasts from Met-1 are similar and show significant variation, with  $\delta^{18}\text{O}_{\text{VSMOW}}$  and  $\Delta^{17}\text{O}_{\text{VSMOW}}$  values ranging from +28.3 to +38.8‰ and from -1.8 to +0.1‰, respectively. These carbonates define a line with a slope of  $0.47 \pm 0.15$ , which is nominally less steep than the terrestrial fraction line (TFL), however, indistinguishable within errors (Fig. 4c).

Finally, the analyzed calcite grains in the matrix of the CM1/2 lithology also show a significant variation, ranging in  $\delta^{18}\text{O}_{\text{VSMOW}}$  from +25.2 to +42.2‰ and in  $\Delta^{17}\text{O}_{\text{VSMOW}}$  from -2.9 to -0.3 ‰. They define a line of slope  $0.55 \pm 0.24$  (Fig. 4d).

### 3.2.2. Bulk composition

The bulk chemical compositions (major, trace and rare-earth elements) of the Met-1 and CM1/2 lithologies of Aguas Zarcas are given in Table 3 and shown in Figure 6. The major oxides of Met-1 display a good match with mean CM carbonaceous chondrites (Braukmüller et al., 2018), except for FeO and CaO, which are slightly more abundant in Met-1 with values of 31.2 wt% and 1.87 wt%, respectively. The trace elements are similar in both lithologies (except for an Sc depletion in Met-1 of about <5 ppm) and agree with CM

chondrites (Fig. 6). The CI chondrite-normalized (Barrat et al., 2012) rare-earth element (REE) patterns of Met-1 and CM1/2 lithologies are extremely flat, with 1.4× and 1.09×CI abundances, respectively. The REE patterns of the Met-1 lithology are comparable to abundances in Paris (Hewins et al., 2014), while the CM1/2 lithology has a flat pattern but with much lower values.

### 3.2.3. Bulk water content and CO<sub>2</sub> analyses

The water contents of the Met-1 lithology from three independent measurements are 7.52, 8.34 and 7.85 wt% (mean: 7.90 wt%) for the dried sample (dried to 110°C prior to analysis). Another sample of Met-1 was stored at room conditions for some days prior to analysis, and adsorbed terrestrial water may have been present, raising values. This measurement revealed a similar value of 8.13 wt% H<sub>2</sub>O. The carbon content of the Met-1 lithology has a high C<sub>total</sub> of 2.74 wt%.

### 3.2.4. Ti, Cr, and Te isotopic compositions

The Ti and Cr isotopic compositions of the Met-1 and CM1/2 lithologies as well as the mass-dependent Te isotope data of the Met-1 lithology are provided in Table 4 and plotted in Figure 7. The Met-1 lithology has a  $\epsilon^{53}\text{Cr}$  value of  $0.19 \pm 0.11$  and a  $\epsilon^{54}\text{Cr}$  value of  $1.05 \pm 0.18$  ( $n = 6$ ; all uncertainties are student-t 95% CI), which is close to the average Cr isotopic composition of CM chondrites (e.g., Trinquier et al., 2009; Torrano et al., 2021). Its Ti isotopic composition of  $\epsilon^{46}\text{Ti} = 0.55 \pm 0.08$ ,  $\epsilon^{48}\text{Ti} = 0.00 \pm 0.04$ , and  $\epsilon^{50}\text{Ti} = 2.57 \pm 0.11$  ( $n = 12$ ) agrees within error with literature values for both CM and CR chondrites (Trinquier et al., 2009; Zhang et al., 2012; Torrano et al., 2021). In a combined diagram of  $\epsilon^{50}\text{Ti}$  vs.  $\epsilon^{54}\text{Cr}$  (Fig. 7a), Met-1 plots within the compositional field of CM chondrites, at the very lower end towards the compositional field of CR chondrites. For the CM1/2 lithology, the Cr isotopic composition is  $\epsilon^{53}\text{Cr} = 0.07 \pm 0.17$  and  $\epsilon^{54}\text{Cr} = 0.97 \pm 0.11$ , while the Ti isotopic composition is  $\epsilon^{46}\text{Ti} = 0.54 \pm 0.09$ ,  $\epsilon^{48}\text{Ti} = -0.04 \pm 0.05$ , and  $\epsilon^{50}\text{Ti} = 3.02 \pm 0.07$ . Both the Ti and Cr data overlap with the isotopic compositions reported for CM chondrites and, therefore, in  $\epsilon^{54}\text{Cr}$  vs.  $\epsilon^{50}\text{Ti}$  space (Fig. 7a) the CM1/2 lithology plots within the compositional field of CM chondrites.

The mass-dependent Te isotopic composition ( $\delta^{128/126}\text{Te} = 0.08 \pm 0.02$ ) and the Te concentration ( $1387 \pm 37 \text{ ng g}^{-1}$ ) of the Met-1 lithology are indistinguishable from those of CM chondrites, and they overlap with the values of Tagish Lake (Fig. 7c-d). The Te isotopic

data, therefore, seem to link the Met-1 lithology to CM chondrites and other volatile-rich carbonaceous chondrites.

### **3.3. ORGANICS**

#### **3.3.1. Soluble organic matter analysis (Met-1)**

The analysis of the SOM of Aguas Zarcas pre-and post-rain as well as the Met-1 samples with ultra-high-resolution mass spectrometry revealed a high signal density comparable to CM chondrite such as Murchison or Maribo organic chondrites (Schmitt-Kopplin et al., 2010; Haack et al., 2012) and typical of non-thermal stressed and low water-altered CM2 SOM. The pre- and post-rain samples (see supplement) showed almost identical signal profiles and elementary compositions in each nominal mass (Fig. 8A). Similarly, the Met-1 fraction showed a superimposable  $m/z$  signature with additional and increased intensive signals corresponding to polysulfurized compounds (Fig. 8B). The conversion of the exact masses into compositional formulas involving the elements C, H, N, O, S and Mg enabled a visualization in Figure 9 of the whole mass spectrometric profiles in van Krevelen diagrams (Schmitt-Kopplin et al., 2010). Aguas Zarcas showed more than 13,000 elementary compositions, and the metal-rich fraction more than 10,000. The main differences between the Met-1 fraction and the Aguas Zarcas is that the Met-1 fractions have fewer of the higher-mass compounds (Fig. 9A) and a higher number of polysulfurized chemical species (CHOS and CHNOS). Also, the Met-1 fraction shown in Fig. 9B contains more organomagnesium compounds (730 CHOMg) than the pre-rain samples (400 CHOMg) as a possible result of relative higher pressure/thermal stress. In the Met-1 fraction, we observed more oxidized CHO compounds as well as a higher amount of sulfur-rich molecules (Fig. 9C) reflecting a more reduced environment in which metal may be involved as catalysts, being reduced while the available soluble organic phase oxidized possibly in an aqueous environment and/or higher temperatures.

#### **3.3.2. Raman and IR microspectroscopy**

The Raman spectra from carbonaceous materials in the CM lithology, Met-2, and C1 lithology are shown in Figure 10. All spectra show fluorescence background. The D band ( $\sim 1355\text{ cm}^{-1}$ ) and G band ( $\sim 1585\text{ cm}^{-1}$ ) parameters of three lithologies from Aguas Zarcas plot close to Murchison (CM2), which was collected under the same conditions (Kiryu et al., 2020) (Fig. 11).

Micro-FTIR absorption spectra of Met-2, the CM lithology, and the C1 lithology are shown in Figure 12. The IR spectrum of the C1 lithology is similar to CI chondrites, and the CM lithology and Met-2 lithology are similar to CM chondrites (Kebukawa et al., 2019a). The IR spectrum of the C1 lithology shows features at 2965, 2930, and 2860  $\text{cm}^{-1}$  due to aliphatic C-H, indicating that the C1 lithology is rich in primitive OM. The  $\text{CH}_2/\text{CH}_3$  peak height ratio is 2.3, which is much higher than the typical ratio of type 1 and 2 chondrites (1.1-1.4) (Kebukawa et al., 2019a). The higher  $\text{CH}_2/\text{CH}_3$  ratio may indicate short/weak heating as shown in some heated CMs (Quirico et al., 2018). In contrast, no or only weak aliphatic C-H features are observed in the IR spectra of the Met-2 and CM lithologies. Mapping analysis of the Met-2 lithology revealed a local concentration (one pixel from the mapping area;  $\sim 50 \mu\text{m}$ ) of OM (Fig. 13). All the spectra in Figure 12 show a large band at around 1000  $\text{cm}^{-1}$  due to silicate Si-O stretching and a broad band at around 3400  $\text{cm}^{-1}$  due to water (mostly terrestrial adsorbed water but maybe some indigenous to interlayer water in phyllosilicates), with some showing a sharp peak at 3680  $\text{cm}^{-1}$  due to structural OH in phyllosilicates. These features are typical for phyllosilicate-rich aqueously altered carbonaceous chondrites (e.g., Osawa et al., 2005; Beck et al., 2010; Hanna et al., 2020). The C1 lithology shows a clear feature of structural OH in phyllosilicates at 3680  $\text{cm}^{-1}$ , which is consistent with CI1 chondrites (Osawa et al., 2005). CM chondrites show no such feature when IR spectra are collected on powdered samples (Osawa et al., 2005), and are consistent with the Aguas Zarcas CM lithology and Met-2. CM chondrites also have structural OH, but it is mostly hidden by a large water absorption features and is not obvious under ambient conditions unless mild heating is applied to eliminate the adsorbed water (Beck et al., 2010) or the IR spectra are collected on a thin section (Hanna et al., 2020).

In order to overcome the spatial resolution of conventional IR, which is limited to a few tens of microns, we applied the state-of-the-art tapping AFM-IR (Mathurin et al., 2018). We present the results obtained for two different areas of  $1 \mu\text{m} \times 3 \mu\text{m}$  (their locations are shown in Fig. 14) from the Aguas Zarcas CM lithology. In the first area (Figure 15), two acquisitions were obtained at different wavenumbers corresponding to the spectral range of organics' absorption (at 1600  $\text{cm}^{-1}$  and 1710  $\text{cm}^{-1}$ ; Fig. 15a, b) and the spectral range of silicate absorption (1020  $\text{cm}^{-1}$  and 960  $\text{cm}^{-1}$ ; Fig. 15c, d). The IR mappings obtained here present both a first order correlation between the 1710  $\text{cm}^{-1}$  and 1600  $\text{cm}^{-1}$  IR mapping and no clear correlation with any of the silicate absorption mapping. An equivalent result is observed on the second area with the comparison of the IR map at 1020  $\text{cm}^{-1}$  for the silicate absorption and 1600  $\text{cm}^{-1}$  for the organic one. The OM localization is confirmed by local AFM-IR

spectra recorded at two different positions in the second area (Fig. 15 with localization indicated by colored arrows in Fig. 16a)). The first spectrum (blue line) is taken in the area where the 1600  $\text{cm}^{-1}$  is the highest on the composite image and show an excess in the 1600  $\text{cm}^{-1}$  region compared to the second one (green line) which was taken next to the previous one (at a few tens of nanometers) where the 1600  $\text{cm}^{-1}$  absorption is the lowest. These correlating results from IR mappings and local spectra demonstrate the IR absorption at 1600  $\text{cm}^{-1}$  is mainly related to OM absorption (with a possible, but limited OH contribution in the bright 1600  $\text{cm}^{-1}$  IR map regions).

To study the OM distribution in the maps, composite color images which merge the main signal for the OM at 1600  $\text{cm}^{-1}$  (red scale) with that of the silicates at 1020  $\text{cm}^{-1}$  (green scale) are shown for both areas in Fig. 15e and Fig. 16c. In these composite images, it is possible to identify two different distributions of the OM at the sub-micrometric level, where some OM is distributed in grain boundaries or in the matrix (<500 nm hot spots highlighted with yellow dotted circles in Fig. 15e and Fig 16c), while some appears as more extended and diffuse patches spread among the silicates.

Raman measurements were performed on the same microtome section as the one used for AFM-IR measurements. The region mapped with Raman is shown by a white rectangle in Figure 14, overlaid on an optical image of the section. The locations where the two AFM-IR maps were acquired are shown by light blue rectangles. At the bottom of the Raman map, we identified a mineral with spectral features in reasonable agreement with tochilinite (the lower left green spectrum is the one recorded in the Raman brightest spot; the gray spectrum is from an unoriented sample from the ruff database measured at the same laser wavelength, ref R060887 (Lafuente et al., 2015)). The lower right green spectrum shows additional bands to the tochilinite contribution that most likely arose from the other mineral contribution. The red spectra are two bright Raman organic spectra in the Raman map, which is a typical signature showing D and G bands found in carbonaceous meteorites. The upper right green spectrum comes from a very localized region that, in addition to the organic contribution at higher wavenumbers, shows a main peak that can be tentatively associated with a Ca-Mg-, Fe-bearing hydrated silicate (the gray spectrum is from an unoriented actinolite sample from the ruff database measured at the same laser wavelength, ref R060189 (Lafuente et al., 2015)). An image obtained by integrating the signal in the 350-200  $\text{cm}^{-1}$  range is displayed in Figure 14a, showing the spatial distribution of the tochilinite signal. Figure 14b shows the spatial distribution of the organic signal integrated over the 1650-1200  $\text{cm}^{-1}$  range.



The tochilinite region could be mapped with the Raman method because of the absence of a significant carbonaceous/organic component. In addition, the overall AFM-IR and FTIR spectra show the ubiquitous presence of phyllosilicates in Aguas Zarcas that are not necessarily detected in the Raman maps; the lack of these phyllosilicates in the Raman maps occurred not because they are absent but because of several factors. The first is that we voluntarily set a low laser power (0.3 mW) for these measurements to preserve the most fragile components of this sample, as they might have been altered by a higher laser power. In addition, the polyaromatic carbonaceous component is Raman resonant, contrary to the behavior for most minerals; thus, it gives a relatively intense signal that dominates the spectrum and can mask the signal of underlying additional embedded mineral components. Thus, the Raman probing depth depends on the nature of the sample being examined. Nevertheless, these measurements show the variations of chemical information at high spatial resolution, at least at the micron level (given here by the sampling step; the Raman spot is probably slightly smaller than a micron). Overall, the Raman map can be a useful guideline to select certain regions to map in more detail using higher spatial resolution techniques, such as AFM-IR.

### 3.3.3. STXM/C-XANES

STXM elemental maps (C–O–Fe) of the FIB sections taken from Met-2 are shown in Figure 18a,c,e. C-XANES spectra from C-rich spots (OM1 and OM2) show peaks at 285.0 eV due to aromatic carbon, 286.5 eV due to C=O groups, 287.5 eV due to aliphatic carbon, 288.7 eV due to C(=O)O groups, and 290.7 eV due to carbonate (either organic or inorganic) (Fig. 18b, d, f). These peaks are commonly observed in the type 1 and 2 carbonaceous chondrites (Le Guillou et al., 2014) as well as in the least-altered CMs (Vinogradoff et al., 2017; Vollmer et al., 2020). While OM1 and OM2 exhibit common peaks, their intensities vary. Figure 19 shows the peak intensity ratios of 288.7 or 288.5 eV (C(=O)O) over 285.0 eV (aromatic) vs. 287.5 eV (aliphatic) over 285.0 eV (aromatic), obtained after linear baseline subtraction between 280 to 283 eV. OM1 appeared as a condensed smaller particle less than 500 nm and was more aromatic than OM2. OM2 was a diffuse ~1  $\mu\text{m}$  area and was richer in C(=O)O and aliphatic groups than OM1. Such characteristics are also similar to the type 1 and 2 carbonaceous chondrites—diffused OM was found to be less aromatic and O-rich compared to condensed OM (Le Guillou et al., 2014). Thermally metamorphosed chondrites are known to exhibit a sharp  $1s\text{-}\sigma^*$  exciton peak at 291.7 eV accompanied by a broad peak at 292–293 eV, indicating development of graphene structures (Cody et al., 2008). OM2 may contain this

feature, but it is not obvious. The small amount of OM and the high baseline due to the thickness of the FIB section hampered efforts to obtain better signal-to-noise spectra and made it difficult to evaluate this feature. The C-XANES features indicate that this sample only experienced low temperature processes similar to type 1 and 2 chondrites.

We performed additional STXM/C-XANES analyses on FIB sections of the CM lithology (Fig. 14g, h) and the C1 lithology. We found OM particles in the CM lithology to be typically larger than in the Met-2 lithology (Fig. 14g), but the differences in C-XANES features among the Met-2, CM, and C1 lithologies are within the range of heterogeneity within a lithology (Fig. 18). In general, condensed OM tends to be aromatic rich, and diffuse OM tends to be aromatic poor, and the C1 lithology tends to be aromatic poor compared to Met-2 and the CM lithologies (Fig. 18).

#### 3.3.4. H, C, and N isotopic imaging analyses by NanoSIMS

Carbon, nitrogen, and hydrogen stable isotopes images from the Aguas Zarcas Met-2 and C1 lithologies were obtained by the JAMSTEC NanoSIMS (Fig. 20). In the case of Met-2, oxygen and hydrogen were detected across the entire analyzed areas, while sulfur and carbon were heterogeneously distributed, and the distribution of carbon mostly anticorrelated with sulfur. This is consistent with the Raman maps showing the absence of a significant organic component in the tochilinite-rich region (Fig. 14), although sulfur could be due to sulfides as well. The distribution of nitrogen generally correlates well with carbon, but some areas rich in nitrogen are poor in carbon (circled regions in the areas #1 and #3, Fig. 20a). In contrast, carbon is distributed across almost entire regions in the C1 lithology, and, in general, this lithology is more homogeneous than Met-2 (Fig. 20b). Average  $\delta^{13}\text{C}$ ,  $\delta^{15}\text{N}$  and  $\delta\text{D}$  values of entire analyzed regions as well as C-rich regions are shown in Table 5. The  $\delta^{13}\text{C}$  values of Met-2 were between  $-30\text{‰}$  to  $+15\text{‰}$ , the  $\delta^{15}\text{N}$  values were between  $+15\text{‰}$  to  $+50\text{‰}$ , and the  $\delta\text{D}$  values were between  $+10\text{‰}$  to  $+100\text{‰}$ , and these values are within the range of CM chondrites (Alexander et al., 2012). The isotopic ratios of the C1 lithology were similar to the values of Met-2, but  $\delta^{15}\text{N}$  was lower (approximately  $-10\text{‰}$ ). The  $\delta^{13}\text{C}$  in the areas #1 and #2 of Met-2 were slightly higher than in CMs and close to the values of Tagish Lake. Hot spots smaller than  $1\text{ }\mu\text{m}$  with high  $\delta^{15}\text{N}$  values of  $+400\text{‰}$  to  $+800\text{‰}$  were found in area #3 (indicated by arrows, Fig. 20a) (Table 5). A  $\delta^{13}\text{C}$  anomalous area ( $\delta^{13}\text{C} \approx +2000\text{‰}$ ) was found in area #1 (indicated by an arrow in Fig. 20a) and is likely a presolar grain. The  $\delta^{13}\text{C}$  value is consistent with  $^{13}\text{C}$ -enriched presolar SiC grains in CR3 chondrites, which are thought to have originated in AGB stars (Floss and Stadermann, 2009).

## 4. DISCUSSION

### 4.1. Aguas Zarcas lithologies

Comparing the texture and mineralogy of the *Met-1 lithology* with those of known carbonaceous chondrites, it is clear that the lithology has to be classified as ungrouped carbonaceous chondrite matter (Kerraouch et al., 2021). However, it shows some similarities with CM and CR chondrites (Fig.22). According to Kerraouch et al., (2021), silicates and phyllosilicates within this lithology have similar compositions as those of CM chondrites (Zolensky et al., 1993, 1997), and chondrules are frequently surrounded by metal, which is a common feature of CR chondrites (Bischoff, 1992; Weisberg et al., 1993; Bischoff et al., 1993). The water-content of the Met-1 lithology (mean: 7.90 wt%) is consistent with CM measurements from Vacher et al., (2020; 7.8 wt%). These data are also consistent with TGA measurements of some CM chondrites by Garenne et al., (2014), but lower than those from Braukmüller et al., (2018) for CM chondrites. However, the mean chondrule diameter of ~160 µm in Met-1 is different from both CM (270±240 µm; Rubin and Wasson, 1986) and CR (~700 µm; Weisberg et al., 1993) chondrites. Further, the Met-1 lithology shows a rather variable degree of aqueous alteration. Some components, such as calcite and TCIs in the matrix and the complex CAIs with a high abundance of calcite, indicate that it has undergone a moderate to high degree of aqueous alteration (subtype 2.5), but the high abundance of metal indicates on the contrary a relatively low degree of aqueous alteration (subtype 2.9). Moreover, the XRD data also suggest a value of 1.9 (scale of Howard et al., (2015), which corresponds to subtype 2.8 on the Rubin et al.,et al., (2007) scale). The Met-1 lithology is, therefore, distinct from any other known carbonaceous chondrite, making it an important material that could provide new information about the early Solar System.

The *Met-2 lithology* contains the highest metal and sulfide abundances (5 vol%) among the investigated Aguas Zarcas lithologies. It shows close similarities to the Met-1 lithology, except that it contains more metal (~2 times more) and lacks FGRs around coarse-grained objects (e.g., chondrules, CAIs, mineral fragments, etc.). The composition of silicates and the size and abundance of chondrules suggest a close relationship to CM chondrites (Kerraouch et al., 2021). The carbon, nitrogen, and hydrogen isotopic values are also within the range of CM chondrites. The matrix is dominated by poorly crystalline phyllosilicate material, which could mean that Met-2 did not really experience intense aqueous alteration (Kerraouch et al., 2021).

In addition, the presolar grain (Fig. 20) identified during *in situ* C and N isotopic measurements indicates that the unusual Met-2 lithology is very primitive material. This presolar grain originally condensed in a stellar atmosphere before entering the interstellar medium from which our Solar System formed.

The **CM1/2 lithology** presents a high abundance of matrix with a high degree of aqueous alteration. The mean size of relic chondrules (~250  $\mu\text{m}$ ) and their abundance, as well as the observed types of CAIs (e.g., dominance of spinel-diopside inclusions; MacPherson and Davis 1994) indicate a CM-related heritage. These observations are well supported by the oxygen isotope analysis, which is consistent with CM (Kerraouch et al., 2021). Additionally, only about 3 vol% of the lithology is olivine and pyroxene that occur in some relic chondrules or as clasts in the matrix surrounded by phyllosilicates, which indicates a low petrologic type). Evidence of extensive aqueous alteration in the CM1/2 lithology includes the formation of Mg-rich serpentine from Fe-rich cronstedtite (Kerraouch et al., 2021). The lack of tochilinite is probably a result of higher  $f\text{O}_2$  conditions (Zolensky et al., 1997).

The **C1 lithology** is mineralogically similar to xenolithic C1 clasts in many meteorites, including ordinary chondrites, ureilites, and HEDs (Howardite-Eucrite-Diogenite) (e.g., Brearley and Prinz, 1992; Zolensky et al., 1996; Patzek et al., 2018; Chan et al., 2018; Goodrich et al., 2019; Kebukawa et al., 2019c), but different from the unique C1 chondrite Flensburg (Bischoff et al., 2021). The phyllosilicate composition is not consistent with the CM lithologies in Aguas Zarcas, but is similar to that of the phyllosilicates in Almahata Sitta 91A, a C1 chondrite lithology of very unusual isotopic composition (Goodrich et al., 2019; Kerraouch et al., 2021). Thus, it is not clear whether the C1 lithology is directly related to CM chondrites. Only more detailed analyses of larger volumes of the Aguas Zarcas C1 lithology (and O isotopic compositions) will reveal potential relationships to other astromaterials.

## **4.2. CHEMICAL AND ISOTOPIC CHARACTERIZATION**

Considering the chemical and isotopic aspects of the Aguas Zarcas lithologies, it is important to demonstrate differences by examining their oxygen isotopic compositions, which were first published by Kerraouch et al., (2021). These compositions (Fig. 21) clearly indicate that the lithologies formed in different environments and/or under very different conditions (e.g., water/rock ratios), or from initially different parent materials.

#### 4.2.1. Bulk chemistry

Minor and trace elements are good parameters for discriminating between the major chondrite classes (Van Schmus and Hayes 1974; Kallemeyn and Wasson 1979, 1981). The concentration of most of these elements in both samples of Aguas Zarcas Met-1 and CM1/2 lithologies show a good match with those of the median composition of CM chondrites reported by Braukmüller et al., (2018). However, the Met-1 lithology does show some differences.

For major elements, FeO and CaO concentrations are higher in the Met-1 lithology compared to the median composition of CM chondrites. The high value of FeO is related to the high abundance of metals and sulfides shown in the studied sections (PL19111 and PL19125), which represent about 3 vol% modal abundance, and also in the bulk XRD.

For the trace elements, both the Met-1 and CM1/2 lithologies have about 30% and 40%, respectively, lower concentrations of Zn, Cu, and Pb compared to the concentrations of these elements in other CM chondrites (Braukmüller et al., 2018); but, they are still in agreement with values obtained for CM chondrites. The Met-1 lithology does show a significant depletion in Sc relative to the CMs (<6 ppm) and all other chondritic classes (Fig. 6, e.g., CI~5 ppm; Kallemeyn and Wasson 1981). Scandium is a highly refractory element concentrated in the CAIs; therefore, the CI chondrites contain lower amounts of Sc than the CM chondrites due to having few, if any, CAIs (Kallemeyn and Wasson 1981; Hezel et al., 2008). By applying these observations to our sample, the low value of Sc could be attributed to the Met-1 lithology's low abundance of CAIs (<1vol%); even so, the Sc value is still very low in this unusual carbonaceous chondrite.

Additionally, the Zn/Mn vs. Sc/Mn array has proven useful to distinguish samples belonging to different carbonaceous chondrite groups (Boynton, 1984). This array shows that both the Met-1 and CM1/2 lithologies have a Zn/Mn ratio in agreement with CM chondrites. However, the Sc/Mn ratio of the Met-1 lithology is not consistent with any chondrite group (e.g. Fig. 5 in Kallemeyn and Wasson (1981)) due to its low concentration of Sc.

Finally, the REE patterns of the Met-1 and CM1/2 lithologies match well with the mean of CM chondrites (except Gd in Met-1). In particular, Met-1 is in good agreement with the mildly altered CM chondrite Paris, which also contains a significant amount of metal (Hewins et al., 2014).

In summary, the bulk chemical composition of the Met-1 and CM1/2 lithologies of Aguas Zarcas display a strong similarity with the CM chondrites. This confirms the CM1/2 lithology classification as a CM chondrite (Kerraouch et al., 2021). Yet, while the data for

Met-1 may also suggest a close relationship with the CM group, a more precise classification will only be possible upon considering further characteristics (such as isotopic compositions; see next section).

#### **4.2.2. Clues to the origin and relationship of chondritic components inferred from Ti, Cr, and Te isotope systematics**

Carbonaceous chondrites show excesses in neutron-rich Ti and Cr nuclides compared to non-carbonaceous meteorites (e.g., Warren, 2011). While most groups display restricted within-group isotope variability, different CC groups might be distinguished based on their Cr-Ti isotope signatures, which are controlled by variable abundances of isotopically diverse chondritic components (i.e., chondrules, matrix, refractory inclusions). The Ti and Cr isotope data obtained for both the CM1/2 and Met-1 lithology are consistent with those of CM chondrites and support their classification as CM chondritic lithologies. Nevertheless, the Met-1 lithology exhibits a systematically lower  $\epsilon^{50}\text{Ti}$  isotopic composition compared to the CM1/2 lithology that plots on the very low end of the compositional field of CM chondrites and overlaps with the Ti isotopic composition of CR chondrites as well (Fig. 7b). Given that Ti is a refractory element, the Ti isotopic composition of a bulk sample is strongly dependent on the amount of  $^{50}\text{Ti}$ -rich CAI-like material incorporated into a meteorite (Trinquier et al., 2009). This suggests that the Met-1 lithology accreted less CAI-like material compared to what is typically observed for CM chondrites, consistent with the observed low abundance of CAIs (i.e., ~0.7 vol%) and concentrations of refractory elements (such as Sc).

In contrast, the Cr isotopic composition of bulk meteorite samples is only marginally affected by the amount of refractory material, but it varies as a function of volatile element depletion. Recently, Hellmann et al., (2020) showed that the Cr isotopic composition of carbonaceous chondrites is correlated with the amount of matrix, the volatile element content, and the mass-dependent isotopic composition of some volatile elements (e.g., Te, Zn). They concluded that all carbonaceous chondrites, except CRs, are mixtures of the same two components: volatile-rich, isotopically heavy, and  $^{54}\text{Cr}$ -rich CI-like dust (i.e., the matrix) and volatile-poor, isotopically light, and  $^{54}\text{Cr}$ -poor chondrules or chondrule precursors. The CM-like Cr isotope signature of the Met-1 lithology is accompanied by Te isotopic and elemental systematics indistinguishable from CM chondrites (Fig. 7c-d). As such, in a  $\delta^{128/126}\text{Te}-\epsilon^{54}\text{Cr}$  diagram, Met-1 plots along the chondrule-matrix mixing line defined by CI, CM, CV, and CO chondrites as well as average CV, CO, CM chondrules. Our combined Cr and Te isotope data, therefore, suggest a close relationship between the Met-1 lithology and CM chondrites and imply that they contain comparable amounts of CI-like dust and that their chondrules formed

from isotopically similar precursor material. Of note, chondrules in CR chondrites are enriched in  $^{54}\text{Cr}$  relative to chondrules in CV, CO, and CM chondrites; thus, CR chondrites plot off the chondrule-matrix mixing line defined by the other CC groups in  $\delta^{128/126}\text{Te}$  versus  $\epsilon^{54}\text{Cr}$  space. Given that the Met-1 lithology exhibits a significantly lower  $\epsilon^{54}\text{Cr}$  value than CR chondrite chondrules, it probably contains few, if any, chondrules that formed from the same precursor material as CR chondrules. Overall, the Met-1 lithology appears to be closely related to CM chondrites, but it probably accreted low amounts of CAI-like material, as is evident from its relatively low  $\epsilon^{50}\text{Ti}$  isotopic composition.

#### **4.2.3. Evidence and conditions of aqueous alteration**

Ca,Al-rich inclusions from chondritic meteorites are widely considered to represent the first solid objects that condensed in the solar nebula (e.g., Grossman 1980; MacPherson et al., 1988). They formed in a hot and reducing environment, in which their elemental compositions are the result of volatility-controlled processes (evaporation-condensation; e.g., Marrocchi et al., 2019). Further, the isotopic compositions of CAIs retain a component of presolar nucleosynthetic origin. Their oxygen isotopic compositions have been studied extensively to decipher conditions of CAI formation (e.g. Yurimoto et al., 1998; Ito et al., 2004) and, thus, to provide insights regarding the high-temperature evolution of the earliest phases of the Solar System (e.g., Clayton et al., 1977; Clayton 1993; Thiemens 1999; Ireland and Fegley 2000). However, if CAIs include carbonate minerals, they could be possible candidates of primitive carbonate condensed directly from the nebula, as shown by claims of carbonate detection in protoplanetary disks (Kemper 2002, Toppani et al., 2005). But, on the other hand, most CAIs have also had long and complex histories, including multiple episodes of impact brecciation, partial melting interspersed, in some cases, with parent body alteration (e.g., MacPherson and Davis 1993), which would have caused some primary phases to be transformed into secondary phases.

Thus, carbonate minerals in carbonaceous chondrites have usually been regarded as secondary products (e.g., Benedix et al., 2003; Vacher et al., 2017). Calcite has been previously described by Armstrong et al., (1982) and MacPherson et al., (1983) in Murchison CAIs, Greenwood et al., (1994) in Cold Bokkeveld CAIs and by Lee and Greenwood (1994) in Murray CAIs. MacPherson et al., (1983) concluded that the calcite formed by interacting with the solar nebula gases, whereas Armstrong et al., (1982), Greenwood et al., (1994) and Lee and Greenwood (1994) all favored the idea that the calcite formed in a parent body environment that had undergone aqueous alteration processes.

Given this uncertainty regarding how calcite forms in CAIs, we examined the oxygen isotopic composition of calcite grains within the different lithologies of Aguas Zarcas because the CAIs in the Met-1 lithology have an unusually high calcite abundance of about 50 vol% (Fig. 5a). The presence of a high abundance of calcite in CAIs and in an almost unaltered (or moderately altered) chondrite with a high abundance of metals is puzzling. The calcite in this lithology may have formed through nebula alteration as suggested in the study by MacPherson et al., 1983), or via parent body alteration as suggested in other studies (e.g., Armstrong et al., 1982; Greenwood et al., 1994; Lee and Greenwood, 1994). To answer this question and to understand the origin of the calcite within the CAI, it is also important to investigate the calcite grains present within its matrix as well as in other CM and CM-like lithologies of Aguas Zarcas to test whether they have the same origins.

The CAIs consisting of abundant calcite grains contain spinel and are mostly surrounded by Al-diopside. A thick phyllosilicate rim, as described in the results section, surrounds each entire CAI. The textural characteristics of the other phases such as spinel and Al-diopside in these CAIs also imply that replacement is unlikely to produce calcite on the parent body.

The oxygen isotopic compositions of the spinel (Fig. 5b) are similar to those of non-altered CAIs in other carbonaceous chondrites (e.g., Grossman 1980; MacPherson et al., 1988). They have a lower  $\delta^{18}\text{O}$  and  $\delta^{17}\text{O}$  and they are distributed on the CCAM line, indicating that they were formed at a higher temperature. Conversely the calcites within CAIs show  $^{17,18}\text{O}$ -rich isotopic compositions, scattering under the TFL. Such values are close to the oxygen isotopic compositions of carbonates reported within CM matrices (Benedix et al., 2003; Verdier-Paoletti et al., 2017, 2019; Vacher et al, 2016; 2018). This indicates that calcite grains precipitated from  $^{17,18}\text{O}$ -rich fluids resulting from isotopic exchange between  $^{16}\text{O}$ -rich anhydrous silicates and  $^{17,18}\text{O}$ -rich fluids (Horstmann et al., 2014; Lindgren et al., 2017; Marrocchi et al., 2018). Similarly, the oxygen isotopic compositions of calcite grains within the matrix of Met-1 scatter under or on the TFL. As do the values of oxygen isotopic ratios of calcite grains within the matrix of Met-1, but with a lower slope (0.48). All the oxygen isotopic compositions of calcite within the matrix in the three CM-clasts and the CM1/2 lithology also show values closer to those of Met-1 in both the complex CAIs and in the matrix (Fig.4), which indicates that they result from secondary alteration processes that took place during the evolution of the parent body.

Considering the whole isotopic dataset of carbonates (Table S1), our data define a mass-dependent trend with  $\delta^{17}\text{O} = (0.52 \pm 0.01) \times \delta^{18}\text{O} - (1.2 \pm 0.5)$ . Such a trend is



consistent with that defined by T1 calcites in other CM chondrites with  $\delta^{17}\text{O} = (0.53 \pm 0.06) \times \delta^{18}\text{O} - (1.2 \pm 2.2)$  (Vacher et al., 2019). T1 calcites correspond to carbonate grains surrounded by Fe–S-rich serpentine/tochilinite (Pignatelli et al., 2016, 2017; Vacher et al., 2019). It has been shown that T1 calcite grains precipitate at relatively low temperatures ranging from 0°C to 50°C (Vacher et al., 2019), whereas serpentine-free T2 calcites form at higher temperatures (i.e., 100°C–150°C). Considering our data and the estimated oxygen isotopic compositions of the CM alteration fluids (Guo and Eiler, 2007), the precipitation temperature of each T1 calcite grain can be calculated according to the isotopic fractionation factor  $\alpha$  (Watkins et al., 2013), which corresponds to the distance between the oxygen isotopic compositions of the fluid and carbonates in the three-oxygen isotope diagram (see Vacher et al., (2019) for further details). This estimation leads to precipitation temperatures of 0°C–50°C, consistent with previous studies (Vacher et al., 2019). Noticeably, only calcite grains measured within the matrix of the Met-1 lithology show O-isotopic values consistent with T2 calcites, which suggests a formation at a higher temperature ranging between 100°C and 150°C.

If the calcite grains were formed during aqueous alteration processes inside a parent body, they would have had to be widely separated in space at that time, and then they all would have to be re-accreted with other chondritic components to form a new parent body. This strongly supports the model of formation of Aguas Zarcas by impact-induced brecciation and re-accretion proposed by Kerraouch et al., (2021).

Finally, the variation in oxygen isotopic compositions obtained from carbonate grains within the different Aguas Zarcas lithologies is interpreted as reflecting changes over time in the oxygen isotopic compositions and/or temperatures of aqueous solutions; as such, they perfectly answer our previous question of how calcite formed in this lithology.

#### **4.2.4. Organic matter and heating process**

Organomagnesium compounds (CHOMg) have been shown to be markers of shock/heating history in the parent body (Ruf et al., 2017, Bischoff et al., 2019b (Fig. S6); Kerraouch et al., 2019, Matzka et al., 2021). High pressure and temperature events generally lead to a higher number of CHOMg and CHOSMg compounds together with a loss in chemical diversity, especially of nitrogen and sulfur compounds (Langbroek et al., 2019). The presence of almost double the amount of organomagnesium in the Met-1 lithology fraction but still with a high chemical diversity comparable to the Aguas Zarcas pre-rain matrix suggests that this lithology has undergone slight temperature stress or short-term temperature exposures. Interestingly, the presence of oxidized CHO compounds and the increase of

polysulfidic CHOS compounds (Fig. 9d) indicate reductive conditions probably due to the higher metal content leading to a different redox steady state in the Met-1 lithology reflecting organo-mineral interactions possibly in aqueous environments. However, the overall molecular structures of organic matter in other Aguas Zarcas lithologies – namely the CM lithology (CR19-001), the Met-2 lithology, and the C1 lithology – generally agree with primitive CM/CI/CR chondrites revealed by IR, Raman, and C-XANES spectroscopic methods. The isotopic analysis also agrees with CM/CI chondrites, but it is not similar to CR chondrites, which have higher  $\delta^{15}\text{N}$  and  $\delta\text{D}$  (Alexander et al., 2007; Alexander et al., 2012). Although the CM, C1, and Met-2 lithologies can be well distinguished based on mineralogy and petrology, there are no large differences in the OM characteristics among these lithologies; this is not very surprising since bulk OM (or inorganic OM) in CI, CM, and CR chondrites are very similar, as seen by many spectroscopic methods including IR (Kebukawa et al., 2011; Orthous-Daunay et al., 2013), Raman (Busemann et al., 2007), XANES (Le Guillou et al., 2014), and nuclear magnetic resonance (NMR) (Cody and Alexander, 2005). However, the OM is heterogeneously distributed at the micron scale, as shown by conventional FTIR and Raman mapping. The results obtained in AFM-IR show that this heterogeneous distribution appears to exist on the sub-micron scale with two possible distributions observed: one in which the OM is concentrated in small hot spots ( $< 500$  nm) and the other in which the OM is more diffused and spread among the silicates. Isotopic heterogeneities are also observed in NanoSIMS  $\delta^{13}\text{C}$  images, suggesting a mixture of OM with different origins. At the sub-micron scale, OM mostly exists in the form of small particles of hundreds of nanometers, as observed by AFM-IR, STXM, and NanoSIMS. The C1 lithology, however, shows a somewhat homogeneous distribution of OM compared to the Met-2 and CM lithologies, suggesting a higher degree of aqueous alteration. Interestingly, the sulfur-bearing phase (likely tochilinite) and organic-rich phase do not overlap, as shown by NanoSIMS and Raman mapping. OM in CM chondrites (and similar groups) often coexists with phyllosilicates (e.g., Pearson et al., 2002; Kebukawa et al., 2010a; Le Guillou et al., 2014; Yesiltas et al., 2015; Yesiltas and Kebukawa, 2016; Kebukawa et al., 2019c). Although tochilinite is usually intergrown with cronstedtite in Aguas Zarcas, the organic-phyllosilicates association – at least phyllosilicates with tochilinite – is not always the case for this meteorite.

The heterogeneous distribution and particle-like structures of OM may imply a pre-accretional origin. In this case, refractory OM should have grown up to several hundreds of nanometers at some point before accretion into the Aguas Zarcas parent body, either in the proto-solar nebulae or in the molecular cloud. Some  $^{15}\text{N}$ -rich particles (hotspots) were

observed by NanoSIMS which may be attributed to such pre-accretional origin (e.g., Terzieva and Herbst, 2000; Charnley and Rodgers, 2002). Although we could not obtain the  $\delta D$  values in these  $^{15}N$ -rich particles (Met-2 (area#3 in Fig. 20a, Table 5)), the  $\delta D$  ratios in other areas were slightly higher than terrestrial values. Considering that the most primitive OM has higher  $\delta D$  up to  $\sim 30,000\text{‰}$  (Busemann et al., 2006; Duprat et al., 2010), hydrogen in the Aguas Zarcas OM could have exchanged with the D-poor water during aqueous alteration (Alexander et al., 2007; Yabuta et al., 2007; Alexander et al., 2010). On the other hand, particle-like OM could be synthesized in the parent body from simple molecules such as formaldehyde and ammonia in the presence of liquid water with moderate concentrations (Cody et al., 2011; Kebukawa et al., 2013). In this scenario, the  $\delta D$  and  $\delta^{15}N$  values of OM would depend on the isotopic compositions of the original molecules as well as of the liquid water (Kebukawa et al., 2021). Currently, one cannot discriminate between a pre-accretional or post-accretional origin of the OM. Since the molecular structures of OM particles show some differences – aromatic rich or less aromatic – the OM particles could be mixtures of OM with different origins.

These Raman parameters of the three lithologies (CM, Met-2, and C1) of Aguas Zarcas plot well away from thermally metamorphosed carbonaceous chondrites such as Allende (CV) and Moss (CO). Thus, these three lithologies did not experience long-term thermal metamorphism. The high fluorescence background also excludes the possibility of having experienced a significant thermal event (Bertrand et al., 1986; Quirico et al., 2014). It is not easy to distinguish short-term heating compared to long-term thermal metamorphism by Raman, i.e., the CM chondrite Y-793321, which experienced short-term heating to  $\sim 300^\circ\text{C}$  –  $500^\circ\text{C}$  (Nakamura, 2005; Tonui et al., 2014), has similar D- and G-band parameters. However, the weakly heated chondrites were known to have slightly higher D-band positions compared to unheated ones (Quirico et al., 2018). In this regard, the D-band positions of these three lithologies of Aguas Zarcas overlap with Murchison, while Y-793321 has a slightly higher D-band position (Fig. 13). Thus, these three lithologies likely escaped a short-term/weak heating event. The IR spectra indicate a possibility that partial heating may have occurred, since CM and Met-2 have little or no aliphatic C-H, which is sensitive to heating – aliphatics are degraded easily at around  $250^\circ\text{C}$  on timescales of minutes to hours (Kebukawa et al., 2010b). The C1 lithology and some regions of Met-2 show aliphatic C-H peaks with high  $\text{CH}_2/\text{CH}_3$  ratios. This also implies the possibility of short heating, since OM from heated chondrites tends to have higher  $\text{CH}_2/\text{CH}_3$  ratios (Kebukawa et al., 2011; Quirico et al., 2018).

If these lithologies were subjected to short heating, the Raman parameters indicated that the heating must be lower than Y-793321, i.e., ~400°C (Nakamura, 2005; Tonui et al., 2014).

#### **4.2.5. The metal-rich lithologies and their origin by mixing and re-accretion**

As discussed in the previous section from the petrographic and chemical characteristics, the metal-rich lithology (Met-1) is a new and unique carbonaceous chondrite lithology that shares similarities with the CR and CM chondrite groups, but is distinct from both based on oxygen isotope data. Its degree of alteration is ambiguous on the whole. Addressing these issues, we propose a possible way to form the Met-1 lithology related to impact-induced brecciation and re-accretion.

#### **1. Metal-1 lithology and its relationship with CM and CR chondrites**

The metal-rich carbonaceous chondrites (MRCCs), including CR chondrites, are thought to have accreted late in the evolution of the protoplanetary disk (Krot et al., 2005; Bollard et al., 2015; Schrader et al., 2017; Budde et al., 2018). These chondrites are characterized by a high abundance of metal and extreme enrichments in <sup>15</sup>N (e.g., Bischoff et al., 1993; Krot et al., 2002), the latter of which is commonly observed in N-bearing gas phase species from dark clouds and collapsing cores in the interstellar medium (Hily-Blant et al., 2013, 2020). This suggests MRCCs accreted in a reservoir isolated from that of other thermally processed Solar System materials, which are thought to have formed in a reservoir located sunward of the MRCCs. Following the Van Kooten et al., (2020) study, CM chondrules may have formed in a reservoir spatially separated from CR chondrules. Further, Mg and Cr isotope data from Van Kooten et al., (2020) suggest that CR chondrites accreted later than CM chondrites. These authors hypothesized on the nature of the barrier separating the two reservoirs and speculated that the barrier isolating the MRCC from the CC reservoir involved the accretion of Saturn. This means that the components making up the Met-1 lithology were probably formed in two different reservoirs, separated by distance and/or time. This assumption makes the scenario of brecciation and re-accretion the best model to interpret the mixture of the two materials (CM- and CR-like or metal-rich parent body) to form the metal-rich lithology.

An impact-triggered scenario for the formation of the metal-rich lithologies of Aguas Zarcas was recently proposed by Kerraouch et al., (2021). Considering this assumption, the

Met-1 lithology was probably formed by re-accretion of debris of two colliding bodies, a CM- and a CR-like (or metal-rich) parent body. Such a scenario would include three major formation stages:

(1) An old, altered CM parent body formed and continued to evolve in the CC reservoir.

(2) Subsequently, this parent body collided with a CR-like (or metal-rich) parent body, after crossing the Saturn barrier from the MRCC reservoir.

(3) The debris of both parent bodies resulting from this impact re-accreted together and formed the new Met-1 daughter body.

Since this body accreted from impact debris, this lithology must have been brecciated, as is observed (Fig. 1). This would also explain the co-existence of highly altered and unaltered material that evolved previously and are now found in close contact (e.g., metals and TCIs). The altered materials were already formed in the precursor CM parent body before being impacted, which is supported by the isotopic signatures considering the Cr and Te isotopic compositions. Based on the isotope data, the major portion of the re-accreted debris likely originated from the collided CM body. The other petrographic characteristics, such as the occurrence of large metal blobs (Fig. 3f) and chondrules with abundant metal and sulfides at their boundaries to the matrix (Fig. 22), may indicate an origin within a CR-related parent body.

During the re-accretion of the new metal-bearing daughter body the incorporated abundance of CAIs was small. This would explain the depletion in  $^{50}\text{Ti}$  in this lithology. This is well supported by the bulk oxygen isotopic composition. Figure 21 shows that this lithology is neither related to CM nor to CR chondrites, and plots significantly away from both fields.

## **2. Met-2 lithology linked to Met-1 lithology?**

The mineralogical and petrological data presented above show that the Met-2 lithology share similar characteristics with the Met-1 lithology. An exception is the high degree of brecciation in the Met-2 lithology, which contains only very few intact chondrules and more altered objects. Some of these differences can be largely accounted for by the observation that Met-2 has experienced extensive brecciation coupled with aqueous alteration. During the re-accretion of the destroyed material resulting from the impact between a CM- and CR-like parent bodies, ice could also have been incorporated. Brecciation then could help to enhance the rate of alteration by breaking chondrules into smaller fragments with larger

surface areas, accelerating the rate of dissolution by aqueous fluids. This explains the highly altered objects in Met-2 that are not present in Met-1 (e.g., Fig. 3a).

We, thus, suggest that Met-2 could be a result of re-accretion of fragments of objects (i.e., fragments of chondrules, metal, silicates, CAIs, etc.) and dust (perhaps phyllosilicates) during the re-accretion of the new metal-rich daughter body. This is supported by petrographic observations. Considering the metal grains, both lithologies share some characteristics of CR chondrites (as shown in Fig. 3b, c, d). However, the abundance of metal within the Met-2 lithology is twice that of the Met-1 lithology, and the metal grain size in Met-1 is twice that of Met-2. This means that during the re-accretion of the metal-rich parent body, the metal incorporated within Met-2 was mostly in form of fragments of metal grains but having twice the abundance as in the case of Met-1.

Moreover, further observations concerning the size of the chondrule lead to the same conclusion. Compared to Met-1, chondrules within Met-2 are smaller (136  $\mu\text{m}$  vs. 186  $\mu\text{m}$ , respectively), and they are largely fragmented. In addition, there are no chondrules dust rims in Met-2. This may indicate that the chondrules could have lost their rims during the impact (similar observations are shown in Fig. 7 of Metzler et al., 1992). On the other hand, the Met-1 lithology contains unfractured chondrules with well-defined accretionary dust rims (Fig. 3e, f).

### **3. Aqueous alteration: before and after brecciation?**

Thus, as stated above, the Met-2 lithology is related to the Met-1 lithology, although Met-2 exhibits more brecciated and strongly altered material. Since Met-2 experienced a generally homogeneous and more intense degree of aqueous alteration than Met-1, it cannot be ruled out that this is related to a very local post-brecciation alteration, perhaps due to the impact-induced melting of local ice grains.

The location of the aqueous alteration in altered chondrites is a controversial topic in the literature, particularly for CM chondrites (Brearley, 2006). Many different scenarios have been proposed, including pre-accretion aqueous alteration (nebular or on a pre-existing parent body that was destroyed; Metzler et al., al. 1992; Cyr et al., 1998; Bischoff 1998; Ciesla et al., 2003; Drake 2005), post-accretion aqueous activity (on the final parent body; Zolensky and McSween, 1988; Hanowski and Brearley, 2001), or combinations of both scenarios (Zolensky and McSween, 1988; Hanowski and Brearley, 2001). According to our observations it is likely that pre-brecciation aqueous alteration occurred within planetesimals that were subsequently destroyed, and these altered components were dispersed and re-accreted with

936 relatively unaltered, anhydrous material to form present-day asteroids (Metzler et al., 1992;  
937 Bischoff, 1998). Therefore, all the altered material that is related to the CM part (e.g.,  
938 carbonate, TCIs) predates the large-scale impact and re-accretion into the later metal-rich  
939 body. A further stage of post-re-accretion alteration then occurred, which slightly altered the  
940 metal in the Met-1 lithology and extended the alteration within the Met-2 lithology (as the  
941 Met-2 is more brecciated, it was more susceptible to this alteration than Met-1).

#### **4.2.6. Impact, re-accretion, and formation of a third-generation parent body for Aguas Zarcas**

Highly brecciated meteorites represent fragmented samples from a variety of parentbodies (e.g., Burbine et al., 2002; Zolensky and Ivanov, 2003; Bischoff et al., 2006, 2010, 2022; Horstmann and Bischoff, 2014; Goodrich et al., 2014; Kerraouch et al., 2019). They provide important information about the history and evolution of asteroids, including impact processes (Keil, 1982). The processes that lead to the mineralogical characteristics of a breccia may include i.a. processes of excavation of subsurface lithologies and mixing of diverse parent body lithologies, incorporation of material from the projectile, impact-related heating and metamorphism, melting, as well as subsequent re-accretion and lithification (e.g., Bischoff et al., 2006). In addition, the study of diverse breccias provides an important opportunity to investigate different types of clasts that do not occur as individual meteorites in our collections, such as new rock types, which certainly applies to the Aguas Zarcas meteorite.

The petrographic characteristics of the different lithologies within this meteorite show that each lithology represents distinct stages of formation and evolution, or rather belong to different parent bodies (Kerraouch et al., 2021). The chondrule sizes and abundances are only two examples. Chondrules are absent in the C1 lithology, while the CM1/2 lithology contains few (~2 vol%), and the CM clasts contain ~20 vol% chondrules (Fig. 1), which is typical for CM chondrites. The Met-1 lithology has a chondrule abundance of about 30 vol%. The chondrule sizes also differ among certain lithologies.

Considering aqueous alteration, the observed CM petrologic types vary from 1.0 to 2.8 in Aguas Zarcas (Rubin et al., 2007; Lentfort et al., 2021; Kerraouch et al., 2021). This means that each lithology experienced a different hydration period during its evolution.

In addition to petrographic differences, the lithologies also display different chemical and isotopic compositions. The large variations of their bulk oxygen isotopic compositions are shown by Kerraouch et al., (2021), and those findings clearly indicate that the different lithologies formed in different environments and/or under different conditions (e.g., water/rock ratios).

Finally, the OM signatures found here show that all the different Aguas Zarcas lithologies we studied experienced a short-term heating event or events in their evolution at a temperature up to ~400°C. This heating event could be linked to the impact-induced brecciation of the different fragments and their separation from their original bodies, followed



by their final accretion in the new generation body Aguas Zarcas. Noble gas analyses of some Aguas Zarcas CM lithologies by Davidson et al., (2020) show no evidence for solar wind implantation, indicating that these fragments did not originate from the surface of their original parent body(ies), which is a further clue for brecciation and mixing materials from deeper areas of an earlier parent body generation.

Meteorite breccias form during impacts between asteroids even at very low impact velocities without producing distinct visible shock features; impact velocities of above 0.5 to 1 km/s result in the formation of visible shock features like shocked and melted minerals (Stöffler et al., 1988; Bischoff and Stöffler, 1992). While impact velocities in the main asteroid belt due to mutual collisions currently range from 1 to 12 km/s with a mean of 5.3 km/s (Bottke et al., 1994), this was not the case for the Aguas Zarcas samples, as no strongly shocked minerals and melted components were observed. Since no olivines with planar fractures have been observed the shock pressure cannot have been in excess of 5-10 GPa (max. C-S2; Stöffler et al., 2018). Therefore, we suggest that only low-velocity impacts were involved in the formation and evolution of Aguas Zarcas and its lithologies.

In summary, the petrographic, isotopic, and compositional differences among the various Aguas Zarcas fragments provide good arguments for a model concerning the formation of the last Aguas Zarcas parent body by impact-induced brecciation and re-accretion. Several precursor parent bodies may have been involved in these processes of impact brecciation, mixing, and re-assembly.

Finally, among many types of chondritic and achondritic breccias (e.g., Keil, 1982, Bischoff et al., 2006, 2018) extreme examples exist with the samples of Kaidun (e.g., Zolensky and Ivanov, 2003) and Almahata Sitta (e.g., Bischoff et al., 2010, 2022; Horstmann et al., 2010; Horstmann and Bischoff, 2014; Goodrich et al., 2014). These samples are considered to be the most impressive and fascinating meteoritic breccias, consisting of abundant millimeter and sub-millimeter-sized fragments. A combination of different processes such as accretion, metamorphism, differentiation, brecciation, destruction, and re-accretion are certainly responsible for producing this kind of multifaceted polymict breccias. Zolensky and Ivanov (2003) suggest that Kaidun may derive from an especially large asteroid like Ceres or an unusually located one like Phobos, the largest moon of Mars. In this respect, Aguas Zarcas is also very different from other polymict CCs, in which different carbonaceous lithologies (e.g., CM, C1, metal-rich lithologies) are well consolidated in one thin section.

## 5. Conclusion

The Aguas Zarcas meteorite is a brecciated carbonaceous chondrite containing several different lithologies. The sharp boundary between the different adjacent lithologies makes the Aguas Zarcas meteorite a perfect breccia. Our new detailed studies, based on mineralogical, chemical, isotopic, and organic matter characteristics, show that each lithology is different from the others in its properties. The variations in their bulk oxygen isotopic compositions indicate that the different lithologies were formed in different environments and/or under different conditions (e.g., water/rock ratios). Each lithology has undergone a different degree of aqueous alteration, in which they experienced different hydration periods during their evolution. This suggests that several precursor parent bodies may have been involved in these processes of impact brecciation, mixing, and re-assembly that led to form the second generation Aguas Zarcas body.

The Cr and Ti isotopic data for both the CM1/2 and Met-1 lithology are consistent with those of other CM chondrites, although Met-1 has a much lower  $\epsilon^{50}\text{Ti}$  isotopic composition, which may be due to heterogeneities in the bulk meteorite samples on a larger scale and may reflect different abundances of refractory phases in the different Aguas Zarcas lithologies.

Furthermore, the OM signatures found here indicate that all of the different Aguas Zarcas lithologies have escaped significant heating events, but a short-term heating episode during their evolution cannot be excluded. If this was the case, the temperature was likely lower than  $\sim 400^\circ\text{C}$ . This heating event could be related to the impact-induced brecciation of the various fragments and their separation from their original bodies, followed by their final accretion in the body of the new and third generation of Aguas Zarcas.

## 1031 **Acknowledgements**

1032       We acknowledge the reviewers for their thoughtful comments and efforts towards  
1033 improving our manuscript and thank the Associate Editor Pierre Beck. We thank Ulla  
1034 Heitmann (Münster), Tommaso Di Rocco (Göttingen) for technical and analytical assistance  
1035 and Celeste Brennecke of editorial support.

1036 This work was partly funded by the Deutsche Forschungsgemeinschaft (DFG, German  
1037 Research Foundation) – Project-ID 263649064 – TRR 170 (subproject B05; AB); this is  
1038 TRR170 Publication No. 153. MZ was supported by NASA’s Emerging Worlds and  
1039 Hayabusa2 Participating Scientist Programs. We thank Robert Ward for loaning us some  
1040 meteorite samples. This work was also partly supported by Japan Society for the Promotion of  
1041 Science KAKENHI (grant number JP17H06458, YK, Y. Takeichi & Y. Takahashi;  
1042 JP19H05073, YK; JP18H04468 and JP18K18795, MI). This work was financially supported  
1043 by ANR (Project COMETOR 18-CE31-0011), (DIM-ACAV), CNRS, PNP, CNES and Labex  
1044 P2IO. We thank F. Borondics from the Soleil SMIS beam line for his help for the DRX  
1045 Raman spectrometer measurements. AK is supported by UK Research and Innovation (UKRI)  
1046 grant number MR/T020261/1. MP. is partly funded by a Sofja Kovalevskaja Award of the  
1047 Alexander von Humboldt Foundation.

1048 **References**

- 1049 Alexander C. M. O. D., Fogel M., Yabuta H. and Cody G. D. (2007) The origin and evolution  
1050 of chondrites recorded in the elemental and isotopic compositions of their  
1051 macromolecular organic matter. *Geochim. Cosmochim. Acta* **71**, 4380-4403.
- 1052 Alexander C. M. O. D., Newsome S. D., Fogel M. L., Nittler L. R., Busemann H. and Cody G.  
1053 D. (2010) Deuterium enrichments in chondritic macromolecular material—Implications  
1054 for the origin and evolution of organics, water and asteroids. *Geochim. Cosmochim.*  
1055 *Acta* **74**, 4417-4437.
- 1056 Alexander C. M. O. D., Bowden R., Fogel M. L., Howard K. T., Herd C. D. and Nittler L. R.  
1057 (2012) The provenances of asteroids, and their contributions to the volatile inventories  
1058 of the terrestrial planets. *Science* **337**, 721-723.
- 1059 Alexander C. M. O'D., Bowden R., Fogel M. L. and Howard K. T. (2015) Carbonate  
1060 abundances and isotopic compositions in chondrites. *Meteor. Planet. Sci.* **50**, 810-833.
- 1061 Anders, E., and Grevesse, N. (1989) Abundances of the elements. Meteoritic and solar.  
1062 *Geochimica et Cosmochimica Acta*, 53, 197–214.
- 1063 Armstrong J. T., Meeker G. P., Huneke J. C., and Wasserburg G. J. ( 1982) The Blue Angel:  
1064 I. The mineralogy and petrogenesis of a hibonite inclusion from the Murchison  
1065 meteorite. *Geochim. Cosmochim. Acta* **46**, 575-596.
- 1066 Barrat J.-A., Zanda B., Moynier F., Bollinger C., Liorzou C., and Bayron G. (2012)  
1067 Geochemistry of CI chondrites: Major and trace elements, and Cu and Zn isotopes.  
1068 *Geochim. Cosmochim. Acta* **83**, 79-92.
- 1069 Beck P., Quirico E., Montes-Hernandez G., Bonal L., Bollard J., Orthous-Daunay F.-R.,  
1070 Howard K.T., Schmitt B., Brissaud O., Deschamps F., Wunder B., and Guillot S.  
1071 (2010) Hydrous mineralogy of CM and CI chondrites from infrared spectroscopy and  
1072 their relationship with low albedo asteroids. *Geochim. Cosmochim. Acta* **74**, 4881-  
1073 4892.
- 1074 Benedix G., Leshin L., Farquhar J., Jackson T., and Thiemens M. 2003. Carbonates in CM2  
1075 chondrites: Constraints on alteration conditions from oxygen isotopic compositions  
1076 and petrographic observations. *Geochim. Cosmochim. Acta* **67**, 1577–1588.

1077 Bertrand, P., Pittion, J.-L. and Bernaud, C. (1986) Fluorescence of sedimentary organic matter  
1078 in relation to its chemical composition. *Org. Geochem.* **10**, 641-647.

1079 Bischoff A. (1992) ALH 85085, Acfer 182, and Renazzo-type chondrites - Similarities and  
1080 differences. *Meteoritics* **27**, 203-204.

1081 Bischoff A.: Aqueous alteration of carbonaceous chondrites: Evidence for preaccretionary  
1082 alteration - a review. *Meteoritics & Planet. Sci.* **33**, 1113- 1122 (1998).

1083 Bischoff A., Palme H., Ash R.D., Clayton R.N., Schultz L., Herpers U., Stöffler D., Grady  
1084 M.M., Pillinger C.T., Spettel B., Weber H., Grund T., Endreß M., and Weber D. (1993)  
1085 Paired Renazzo-type (CR) carbonaceous chondrites from the Sahara. *Geochim.*  
1086 *Cosmochim. Acta* **57**, 1587–1604.

1087 Bischoff A., Scott E. R. D., Metzler K., and Goodrich C. A. (2006) Nature and Origins of  
1088 meteoritic breccias. Book chapter in “Meteorites and the Early Solar System II” (eds.  
1089 D.S. Lauretta and H.Y. McSween Jr.), *Univ. of Arizona, Tucson* 679-712.

1090 Bischoff A., Horstmann M., Pack A., Laubenstein M., and Haberer S. (2010) Asteroid 2008  
1091 TC<sub>3</sub> – Almahata Sitta: A spectacular breccia containing many different ureilitic and  
1092 chondritic lithologies. *Meteoritics & Planetary Science* **45**, 1638-1656.

1093 Bischoff A., Ebert S., Metzler K., and Lentfort S. (2017) Breccia classification of CM  
1094 chondrites. *Meteoritics & Planetary Science* **52**, Special Issue, A26, #6089.

1095 Bischoff A., Schleiting M., Wieler R., and Patzek M. (2018) Brecciation among 2280 ordinary  
1096 chondrites – constraints on the evolution of their parent bodies. *Geochim. Cosmochim.*  
1097 *Acta* **238**, 516-541.

1098 Bischoff A., Alexander C. M. O'D., Barrat J.-A., Burkhardt C., Busemann H., Degering D.,  
1099 Di Rocco T., Fischer M., Fockenberg T., Foustoukos D. I., Gattacceca J., Godinho J. R.  
1100 A., Harries D., Heinlein D., Hellmann J. L., Hertkorn N., Holm A., Jull A. J. T.,  
1101 Kerraouch I., King A. J., Kleine T., Koll D., Lachner J., Ludwig T., Merchel S.,  
1102 Mertens C. A. K., Morino P., Neumann W., Pack A., Patzek M., Pavetich S., Reitze M.  
1103 P., Rüfenacht M., Rugel G., Schmidt C., Schmitt-Kopplin P., Schönbächler M., Tieloff  
1104 M., Wallner A., Wimmer K., and Wölfer E. (2021) The old, unique C1 chondrite  
1105 Flensburg – insight into the first processes of aqueous alteration, brecciation, and the

1106 diversity of water-bearing parent bodies and lithologies. *Geochim. Cosmochim. Acta*.  
1107 **293**, 142–186.

1108 Bischoff A., Bannemann L., Decker S., Ebert S., Haberer S., Heitmann U., Horstmann M.,  
1109 Klemm K. I., Kraemer A.-K., Lentfort S., Patzek M., Storz J., and Weyrauch M. (2022)  
1110 Asteroid 2008 TC3, not a polymict ureilitic but a polymict C1 chondrite parent body? -  
1111 Survey of 249 Almahata Sitta fragments. *Meteoritics & Planetary Science*; DOI:  
1112 10.1111/maps.13821.

1113 Bollard J., Connelly J., and Bizzarro M. (2015) Pb-Pb dating of individual chondrules from  
1114 the CBa chondrite Gujba: Assessment of the impact plume formation model.  
1115 *Meteoritics & Planetary Science* **50**, 1197–1216.

1116 Bottke W. F., Nolan M. C., Greenberg R., and Kolvoord R. A. (1994) Velocity distributions  
1117 among colliding asteroids. *Icarus* **107**, 255-268.

1118 Braukmüller N., Wombacher F., Hezel D. C., Escoube R., and Münker C. (2018) The  
1119 chemical composition of carbonaceous chondrites: Implications for volatile element  
1120 depletion, complementarity and alteration. *Geochim. Cosmochim. Acta* **239**, 17-48.

1121 Brearley A. and Prinz M. (1992) CI chondrite-like clasts in the Nilpena polymict ureilite:  
1122 Implications for aqueous alteration processes in CI chondrites. *Geochimica et*  
1123 *Cosmochimica Acta* **56**, 1373-1386.

1124 Brearley, A.J., and Jones, R.H. (1998) Chondritic meteorites. In J.J. Papike, Ed., *Planetary*  
1125 *Materials*, 36, p. 3-1–3-398. Reviews in Mineralogy and Geochemistry,  
1126 Mineralogical Society of America, Chantilly, Virginia.

1127 Brearley A. J. (2006) The action of water. In *Meteorites and the Early Solar System II* (ed. D.  
1128 S. Lauretta and Jr. H. Y. McSween). *Tucson Arizona: The University of Arizona Press*  
1129 pp. 587-624.

1130 Browning L. B., McSween H. Y. Jr., and Zolenski M. E. (1996) Correlated alteration effects in  
1131 CM carbonaceous chondrites. *Geochimica et Cosmochimica Acta* 60: 2621-  
1132 2633.

1133 Budde G., Kruijer T., and Kleine T. (2018) Hf-W chronology of CR chondrites: Implications  
1134 for the timescales of chondrule formation and the distribution of <sup>26</sup>Al in the solar  
1135 nebula. *Geochim. Cosmochim. Acta* **222**, 284–304.

- 1136 Burbine T. H., McCoy T. J., Meibom A., Gladman B., and Keil K. (2002) Meteoritic parent  
1137 bodies: their number and identification. In Asteroids III (W. F. Bottke et al., eds.), *Univ.*  
1138 *Arizona Press*. pp. 653-667.
- 1139 Busemann H., Young A. F., Alexander C. M. O., Hoppe P., Mukhopadhyay S. and Nittler L.  
1140 R. (2006) Interstellar chemistry recorded in organic matter from primitive meteorites.  
1141 *Science* **312**, 727-730.
- 1142 Busemann H., Alexander C. M. O. D. and Nittler L. R. (2007) Characterization of insoluble  
1143 organic matter in primitive meteorites by microRaman spectroscopy. *Meteoritics &*  
1144 *Planetary Science* **42**, 1387-1416.
- 1145 Charnley, S. and Rodgers, S. (2002) The end of interstellar chemistry as the origin of nitrogen  
1146 in comets and meteorites. *The Astrophysical Journal Letters* **569**, L133-L137.
- 1147 Chan Q., Zolensky M., Kebukawa Y., Franchi I., Wright I., Zhao I., Rahman Z., and Utas J.  
1148 (2018) Primitive oxygen-, nitrogen-, and organic-rich vein preserved in a xenolith  
1149 hosted in the metamorphosed Carancas meteorite *49th Lunar and Planetary Science*  
1150 *Conference*. (abstract #1191).
- 1151 Cody, G. D. and Alexander, C. M. O. D. (2005) NMR studies of chemical structural variation  
1152 of insoluble organic matter from different carbonaceous chondrite groups. *Geochim.*  
1153 *Cosmochim. Acta* **69**, 1085-1097.
- 1154 Cody, G. D., Alexander, C. M. O. D., Yabuta, H., Kilcoyne, A. L. D., Araki, T., Ade, H.,  
1155 Dera, R., Fogel, M., Militzer, B. and Mysen, B. O. (2008) Organic thermometry for  
1156 chondritic parent bodies. *Earth. Planet. Sci. Lett.* **272**, 446-455.
- 1157 Cody, G. D., Heying, E., Alexander, C. M. O. D., Nittler, L. R., Kilcoyne, A. L. D., Sandford,  
1158 S. A. and Stroud, R. M. (2011) Establishing a molecular relationship between chondritic  
1159 and cometary organic solids. *Proceedings of the National Academy of Sciences of the*  
1160 *United States of America* **108**, 19171-19176.
- 1161 Clayton R. N. (1993) Oxygen isotopes in meteorites. *Ann. Rev. Earth Planet. Sci.* **21**, 115-149.

1162 Clayton. N., Onuman.,Grossmanl. and Mayeda T. K. (1977) Distribution of the pre solar  
1163 component in Allende and other carbonaceous chondrites. *Earth Planet. Sci. Lett.* **34**,  
1164 209-224.

1165 Cyr K.E., Sears W.D., and Lunine J.I. (1998) Distribution and evolution of water ice in the  
1166 solar nebula: Implications for Solar System body formation. *Icarus* **135**, 537–548.

1167 Davidson, J., Alexander, C. M. O'D., Bates, H. C., King, A. J., Foustoukos, D. I., Schrader, D.  
1168 L., Bullock, E. S. et al. 2020. Coordinated Studies of Samples Relevant for  
1169 Carbonaceous Asteroid Sample Return: CM Chondrites AZ and Meteorite Hills 00639  
1170 (Abstract #1623). 51st Lunar and Planetary Science Conference. CD-ROM

1171 Duprat J., Dobrica E., Engrand C., Aleon J., Marrocchi Y., Mostefaoui S., Meibom,A.,  
1172 Leroux H., Rouzaud J. N., Gounelle M. and Robert F. (2010) Extreme deuterium  
1173 excesses in ultracarbonaceous micrometeorites from central Antarctic snow. *Science*  
1174 **328**, 742-745.

1175 Drake M. J. (2005) rigin of water in the terrestrial planets. *Meteoritics & Planetary Science*  
1176 **40**, 519-527

1177 Ferrari, A. C. and Robertson, J. (2000) Interpretation of Raman spectra of disordered and  
1178 amorphous carbon. *Physical Review B* **61**, 14095-14107.

1179 Floss C. and Stadermann F. J. (2009) High abundances of circumstellar and interstellar C-  
1180 anomalous phases in the primitive CR3 chondrites QUE 99177 and MET 00426.  
1181 *Astrophysical Journal* **697**, 1242-1255.

1182 Garenne A., P. Beck, G. Montes Hernandez, R. Chiriac, F. Toche, E. Quirico, L. Bonal, B.  
1183 Schmitt (2014). The abundance and stability of “water” in type 1 and 2  
1184 carbonaceous chondrites (CI, CM and CR) *Geochim. Cosmochim. Acta*, 137,  
1185 pp. 93-112,  
1186

1187 Garvie, (2021) Mineralogy of the 2019 Aguas Zarcas (CM2) carbonaceous chondrite  
1188 meteorite fall. *American Mineralogist*.106 (12): 1900–1916.  
1189

1190 Goodrich C. A., Bischoff A., and O'Brien D. P. (2014). Asteroid 2008 TC<sub>3</sub> and the fall of  
1191 Almahata Sitta, a unique meteorite breccia. *Elements* 10, 31-37.



1192 Goodrich C., Zolensky M., Fioretti A., Shaddad M., Downes H., Hiroi T., Kohl I., Young E.,  
1193 Kita N., Śliwiński M., Hamilton V., Riebe M., Busemann H., Macke R., Ross D., and  
1194 Jenniskens P. (2019) The first samples from Almahata Sitta showing contacts between  
1195 ureilitic and chondritic lithologies: Implications for the structure and composition of  
1196 Asteroid 2008 TC3. *Meteoritics & Planetary Science* **54**, 2769-2813.

1197 Grossman L. (1980) Refractory inclusions in the Allende meteorite. *Ann. Rev. Earth Planet.*  
1198 *Sci.* **8**, 559-608.

1199 Greenwood R.C., Lee M.R., Hutchison R., and Barber D.J. (1994) Formation and alteration of  
1200 CAIs in Cold Bokkeveld (CM2) *Geochim. Cosmochim. Acta* **58**, 1913-1935.

1201 Greenwood, R.C., Burbine, T.H., and Franchi, I.A. (2020) Linking asteroids and meteorites to  
1202 the primordial planetesimal population. *Geochimica et Cosmochimica Acta*,  
1203 277, 377–406.

1204 Grimm R. E., and McSween H. Y. J. (1989) Water and the thermal evolution of carbonaceous  
1205 chondrite parent bodies. *Icarus* **82**, 244–280.

1207 Guo W. and Eiler J. M. (2007) Temperatures of aqueous alteration and evidence for methane  
1208 generation on the parent bodies of the CM chondrites. *Geochimica et Cosmochimica*  
1209 *Acta* **71**, 5565–5575.

1210 Haack H., Grau Th., Bischoff A., Horstmann M., Wasson J., Norup Sørensen A., Laubenstein  
1211 M., U. Ott, Palme H., Gellissen M., Greenwood R.C., Pearson V.K., Franchi I.A.,  
1212 Gabelica Z., and Schmitt-Kopplin Ph. (2012) Maribo – a new CM fall from Denmark.  
1213 *Meteoritics & Planetary Science* **47**, 30–50.

1214 Hanna R.D., Hamilton V.E., Haberle C.W., King A.J., Abreu N.M., and Friedrich J.M. (2020)  
1215 Distinguishing relative aqueous alteration and heating among CM chondrites with IR  
1216 spectroscopy. *Icarus* **346**, 113760.

1217 Hanowski N. P. and Brearley A. (2001) Aqueous alteration of chondrules in the CM  
1218 carbonaceous chondrite, Allan Hills 81002: Implications for parent body alteration.  
1219 *Geochim. Cosmochim. Acta* **65**, 495-518.

1220 Hellmann J. L., Hopp T., Burkhardt C., and Kleine T. (2020) Origin of volatile element  
1221 depletion among carbonaceous chondrites. *Earth and Planetary Science Letters* **549**,  
1222 116508.

- 1223 Hewins R. H., Bourot-Denise M., Zanda B., Leroux H., Barrat J.-A., Humayun M., Göpel C.,  
1224 Greenwood R. C., Franchi I. A., Pont S., Lorand J.-P., Cournede C., Gattacceca J.,  
1225 Rochette P., Kuga M., Marrocchi Y., and Marty B. (2014) The Paris meteorite, the least  
1226 altered CM chondrite so far. *Geochim. Cosmochim. Acta* **124**, 190–222.
- 1227 Hezel D.C., S.S. Russell, A.J. Ross, A.T. Kearsley (2008) Modal abundances of CAIs:  
1228 implications for bulk chondrite element abundances and fractionations Meteorit. *Planet.*  
1229 *Sci.* **43**, 1879-1894.
- 1230 Hily-Blant P., Bonal L., Faure A., and Quirico E. (2013) The <sup>15</sup>N-enrichment in dark clouds  
1231 and solar system objects. *Icarus* **223**, 582–590.
- 1232 Hily-Blant P., Pineau des Forêts G., Faure A., and Flower D. R.(2020) Depletion and  
1233 fractionation of nitrogen in collapsing cores. *Astronomy & Astrophysics* **643**, A76
- 1234 Horstmann M., Bischoff A., Pack A., and Laubenstein M. (2010) Almahata Sitta – fragment  
1235 MS-CH: Characterization of a new chondrite type. *Meteoritics & Planetary Science* **45**,  
1236 1657-1667.
- 1237 Horstmann M. and Bischoff A. (2014) The Almahata Sitta polymict breccia and the late  
1238 accretion of Asteroid 2008 TC<sub>3</sub> - Invited Review. *Chemie der Erde - Geochemistry* **74**,  
1239 149-184.
- 1240 Howard K.T. , Benedix G.K., P.A. Bland, G. Cressey (2009). Modal mineralogy of CM2  
1241 chondrites by X-ray diffraction (PSD-XRD). Part 1: Total phyllosilicate  
1242 abundance and the degree of aqueous alteration. *Geochimica et Cosmochimica*  
1243 *Acta* **73**. 4576-4589
- 1244 Howard K.T., Alexander C.M.O'D., Schrader D.L., Dyl K.A. (2015) Classification of  
1245 hydrous meteorites (CR, CM and C2 ungrouped) by phyllosilicate fraction:  
1246 PSD-XRD modal mineralogy and planetesimal environments Author links  
1247 open overlay. *Geochimica et Cosmochimica Acta* 149:206.
- 1248 Ireland T. R., and Fegley B., JR. (2000) The Solar System's earliest chemistry: Systematics of  
1249 refractory inclusions. *Inti. Geol. Rev.* **42**, 865-894.
- 1250 Ito M., Yurimoto H., and Nagasawa H. (2004) Oxygen isotopic SIMS analysis in Allende  
1251 CAI: Details of the very early thermal history of the solar system. *Geochim. Cosmochim.*  
1252 *Acta* **68**, 2905–2923.

- 1253 Kallemeyn G. W., and Wasson J. T. (1979) Refractory element fractionations among  
1254 carbonaceous chondrite groups. *Nature* **282**, 827-829.
- 1255 Kallemeyn G. W. and Wasson J. T. (1981) The compositional classification of chondrites- I.  
1256 The carbonaceous chondrite groups. *Geochim. Cosmochim. Acta* **45**, 1217–1230.
- 1257 Kebukawa Y., Nakashima S., Ishikawa M., Aizawa K., Inoue T., Nakamura-Messenger K.  
1258 and Zolensky M. E. (2010a) Spatial distribution of organic matter in the Bells CM2  
1259 chondrite using near-field infrared microspectroscopy. *Meteoritics & Planetary Science*  
1260 **45**, 394-405.
- 1261 Kebukawa Y., Nakashima S. and Zolensky M. E. (2010b) Kinetics of organic matter  
1262 degradation in the Murchison meteorite for the evaluation of parent-body temperature  
1263 history. *Meteoritics & Planetary Science* **45**, 99-113.
- 1264 Kebukawa Y., Alexander C. M. O. D. and Cody G. D. (2011) Compositional diversity in  
1265 insoluble organic matter in type 1, 2 and 3 chondrites as detected by infrared  
1266 spectroscopy. *Geochim. Cosmochim. Acta* **75**, 3530–3541.
- 1267 Kebukawa Y., Kilcoyne A. L. D. and Cody G. D. (2013) Exploring the potential formation of  
1268 organic solids in chondrites and comets through polymerization of interstellar  
1269 formaldehyde. *The Astrophysical Journal* **771**, 19.
- 1270 Kebukawa Y., Alexander C. M. O. D. and Cody G. D. (2019a) Comparison of FT-IR spectra  
1271 of bulk and acid insoluble organic matter in chondritic meteorites: An implication for  
1272 missing carbon during demineralization. *Meteoritics & Planetary Science* **54**, 1632–  
1273 1641.
- 1274 Kebukawa Y., Ito, M., Zolensky M. E., Greenwood R. C., Rahman Z., Suga H., Nakato A.,  
1275 Chan Q. H., Fries M. and Takeichi Y. (2019b) A novel organic-rich meteoritic clast  
1276 from the outer Solar System. *Scientific Reports* **9**, 3169.
- 1277 Kebukawa Y., Kobayashi H., Urayama N., Baden N., Kondo M., Zolensky M. E. and  
1278 Kobayashi K. (2019c) Nanoscale infrared imaging analysis of carbonaceous chondrites  
1279 to understand organic-mineral interactions during aqueous alteration. *Proceedings of the*  
1280 *National Academy of Sciences* **116**, 753-758.

- 1281 Kebukawa Y., Zolensky M. E., Ito M., Ogawa N. O., Takano Y., Ohkouchi N., Nakato A.,  
1282 Suga H., Takeichi Y., Takahashi Y. and Kobayashi K. (2020) Primordial organic matter  
1283 in the xenolithic clast in the Zag H chondrite: Possible relation to D/P asteroids.  
1284 *Geochim. Cosmochim. Acta* **271**, 61-77.
- 1285 Kebukawa Y., Zolensky M. E., Goodrich C. A., Ito M., Ogawa N.O. , Takano Y.,  
1286 Ohkouchi N., Kiryu K., Igisu M., Takazo Shibuya, Matthew A. Marcus, Takuji Ohigashi,  
1287 Martinez J, Kodama Y., Shaddad M.H., Jenniskens P. (2021) Organic matter in  
1288 carbonaceous chondrite lithologies of Almahata Sitta: Incorporation of previously  
1289 unsampled carbonaceous chondrite lithologies into ureilitic regolith. *Meteoritics &*  
1290 *Planetary Science*. 57: 1311-1327 <https://doi.org/10.1111/maps.13713>
- 1291 Kemper F., Jäger C., Waters L. B. F. M., Henning Th., Molster F. J., Barlow M. Lim J., T.  
1292 and Koter A. de (2002) Detection of carbonates in dust shells around evolved stars  
1293 *Nature* **415**, 295–297.
- 1294 Keil K. (1982) Composition and origin of chondritic breccias. In *Workshop on Lunar*  
1295 *Breccias and Soils and Their meteoritic Analogs* (eds. G. J. Taylor and L. L.  
1296 Wilkening), pp. 65-83. LPI Technical Report 82-02. Lunar Planetary Institute.
- 1297 Kerraouch I., Ebert S., Patzek M., Bischoff A., Zolensky M.E., Pack A., Schmitt-Kopplin Ph.,  
1298 Belhai, D, Bendaoud A., Leg L. (2019) A light, chondritic xenolith in the Murchison  
1299 (CM) chondrite – Formation by fluid-assisted percolation during metasomatism?  
1300 *Geochemistry* **79** (4) 125518.
- 1301 Kerraouch I., Bischoff A., Zolensky M.E., Pack A., Patzek M., Wölfer E., Burkhardt C., and  
1302 Fries M. (2020) Characteristics of a new carbonaceous, metal-rich lithology found in  
1303 the carbonaceous chondrite breccia Aguas Zarcas. *Lunar and Planetary Science Conference* **51**, abstract #2011.
- 1304 Kerraouch I., A. Bischoff, M. E. Zolensky, A. Pack, M. Patzek, R. D. Hanna, M. D. Fries, D.  
1305 Harries, Y. Kebukawa, L. Le, M. Ito, and Z. Rahman. (2021) The polymict  
1306 carbonaceous breccia Aguas Zarcas: A potential analogue to samples being returned by  
1307 the OSIRIS-REx and Hayabusa2 missions. *Meteoritics & Planetary Science* **56**, 277-  
1308 310.

1309 King A. J., Schofield P. F. and Russell S. S. (2017) Type 1 aqueous alteration in CM  
1310 carbonaceous chondrites: Implications for the evolution of water-rich asteroids.  
1311 *Meteorit. Planet. Sci.* **52**, 1197–1215.

1312 King A.J., Batesa H.C., Krietsch D., Busemann H., Clay P.L., Schofield P.F., Russell S.S.  
1313 (2019) The Yamato-type (CY) carbonaceous chondrite group: Analogues for the  
1314 surface of asteroid Ryugu? *Geochemistry* **79**, 125531.

1315 Kiryu K., Kebukawa Y., Igisu M., Shibuya T., Zolensky M. E., and Kobayashi K. (2020)  
1316 Kinetics in thermal evolution of Raman spectra of chondritic organic matter to evaluate  
1317 thermal history of their parent bodies. *Meteoritics & Planetary Science* **55**, 1848–1864.

1318 Kodama Y, Tomioka N, Ito M, Imae N (2020) Developments in microfabrication of mineral  
1319 samples for simultaneous EBSD-EDS analysis utilizing a FIB-SEM instrument: study  
1320 on an S-type cosmic spherule from Antarctica. *Journal of Mineralogical and*  
1321 *Petrological Sciences* (accepted).

1322 Krot A., Meibom A., Weisberg M., and Keil K. (2002) The CR chondrite clan: Implications  
1323 for early solar system processes. *Meteoritics & Planetary Science* **37**, 1451–1490.

1324 Krot A. N., Amelin Y., Cassen P., and Meibom A. (2005) Young chondrules in CB chondrites  
1325 from a giant impact in the early solar system. *Nature* **436**, 989–992.

1326 Lafuente, B., Downs, R., Yang, H. and Stone, N. (2015) The power of databases: the RRUFF  
1327 project. In *Highlights in mineralogical crystallography* Berlin, Germany, W. De  
1328 Gruyter, pp. 1-30.

1329 Langbroek M., P. Jenniskens, L.M. Kriegsman, H. Nieuwenhuis, N. De Kort, J. Kuiper, W.  
1330 Van Westrenen, M. E Zolensky, K. Ziegler, Q.Z. Yin, M. E Sanborn, J. Wimpenny, A.  
1331 Yamakawa, S.J. De Vet, M. Meier, K.C Welten, K. Nishiizumi, M.W Caffee, AS  
1332 Burton, J.P. Dworkin, D.P Glavin, Q. Wu, R.N Zare, A. Ruf, M. Harir, Ph. Schmitt-  
1333 Kopplin (2019) Diepenveen Meteorite Consortium, The CM carbonaceous chondrite  
1334 regolith Diepenveen *Meteoritics & Planetary Science* **54** (7), 1431-1461.

1335 Lee R.L. and Greenwood R.C. (1994) Alteration of calcium-aluminium-rich inclusions  
1336 (CAIs) in the Murray (CM2) carbonaceous chondrite. *Meteoritics & Planetary Science*  
1337 **29**, 780-790

- 1338 Lentfort S., Bischoff A., Ebert S., and Patzek M. (2021) Classification of CM chondrite breccias –  
1339 implications for the evaluation of samples from the OSIRIS-REx and Hayabusa 2 missions.  
1340 *Meteoritics & Planetary Science* **56**, 127-147.
- 1341 Lindgren P., M.R.Lee, N.A.Starkey, and I.A. Franchib (2017) Fluid evolution in CM  
1342 carbonaceous chondrites tracked through the oxygen isotopic compositions of  
1343 carbonates. <https://doi.org/10.1016/j.gca.2017.01.048>.
- 1344 Le Guillou C., Bernard S., Brearley A. J. and Remusat L. (2014) Evolution of organic matter  
1345 in Orgueil, Murchison and Renazzo during parent body aqueous alteration: In situ  
1346 investigations. *Geochim. Cosmochim. Acta* **131**, 368-392.
- 1347 Macpherson G. J., Bar-Matthews M., Tanaka T., Olsen E., and Grossman L. ( 1983)  
1348 Refractory inclusions in the Murchison meteorite. *Geochim. Cosmochim. Acta* **41**, 823-  
1349 839.
- 1350 Macpherson G. J., Wark D. A., and Armstrong J. T. (1988) Primitive material surviving in  
1351 chondrites: Refractory inclusions. In *Meteorites and the Early Solar System* (eds. J.  
1352 F.Kerridge and M. S. Matthews), *Univ. Arizona Press*, Tucson, Arizona, USA pp. 746-  
1353 807.
- 1354 MacPherson G. J. and Davis A. M. (1993) A petrologic and ion microprobe study of a  
1355 Vigarano Type B2 refractory inclusion: evolution by multiple stages of melting and  
1356 alteration. *Geochim. Cosmochim. Acta* **57**, 231–243.
- 1357 Matzka M., LucioM., KanawatiB., Quirico E., Bonal L., Loehle S., and Schmitt-Kopplin P.  
1358 (2021). Thermal History of Asteroid Parent Bodies Is Reflected in Their  
1359 Metalorganic Chemistry. *The Astrophysical Journal Letters* 915 L7.
- 1360 Marrocchi Y., Bekaert D. V. and Piani L. (2018) Origin and abundance of water in  
1361 carbonaceous asteroids. *Earth Planet. Sci. Lett.* **482**, 23–32.
- 1362 Marrocchi Y., Villeneuve J., Jacquet E., Piralla M., and Chaussidon M. (2019) *PNAS* **116**,  
1363 (47) 23461-23466.
- 1364 Metzler K. and Bischoff A. (1996) Constraints on chondrite agglomeration from fine-grained  
1365 chondrule rims. Book chapter in: "*Chondrules and the Protoplanetary Disk*" (eds.  
1366 R.H. Hewins, R.H. Jones, and E.R.D. Scott), *Cambridge University Press*.153-162.

1367 Metzler K., Bischoff A. and Stöffler D. (1992) Accretionary dust mantles in CM-chondrites:  
 1368 Evidence for nebula processes. *Geochimica et Cosmochimica Acta* **56**, 2873-2897.

1369 Mathurin J., Pancani E., Deniset-Besseau A., Kjoller K., Prater C. B., Gref R. and Dazzi A.  
 1370 (2018) How to unravel the chemical structure and component localization of individual  
 1371 drug-loaded polymeric nanoparticles by using tapping AFM-IR. *Analyst* **143**, 5940-  
 1372 5949.

1373 Mathurin J., Dartois E., Pino T., Engrand C., Duprat J., Deniset-Besseau A., Borondics F.,  
 1374 Sandt C. and Dazzi A. (2019) Nanometre-scale infrared chemical imaging of organic  
 1375 matter in ultra-carbonaceous Antarctic micrometeorites (UCAMMs). *Astronomy &*  
 1376 *Astrophysics* **622**, A160.

1377 Nakamura T. (2005) Post-hydration thermal metamorphism of carbonaceous chondrites.  
 1378 *Journal of Mineralogical and Petrological Sciences* **100**, 260-272.

1379 Ohigashi T., Arai H., Araki T., Kondo N., Shigemasa E., Ito A., Kosugi N. and Katoh M.  
 1380 (2013) Construction of the scanning transmission X-ray microscope beamline at  
 1381 UVSOR. *Journal of Physics: Conference Series* **463**, #012006 (abstr.).

1382 Orthous-Daunay F. R., Quirico E., Beck P., Brissaud O., Dartois E., Pino T. and Schmitt B.  
 1383 (2013) Mid-infrared study of the molecular structure variability of insoluble organic  
 1384 matter from primitive chondrites. *Icarus* **223**, 534-543.

1385 Osawa T., KAGI H., Nakamura T., and Noguchi T. (2005) Infrared spectroscopic taxonomy  
 1386 for carbonaceous chondrites from speciation of hydrous components. *Meteoritics &*  
 1387 *Planetary Science* **40**, 71–86.

1388 Patzek M., Pack A., Bischoff A., Visser R., and John T. (2018) O-isotope composition of CI-  
 1389 and CM-like clasts in ureilites, HEDs, and CR chondrites (abstract #6254). *Meteoritics*  
 1390 *& Planetary Science* **53**, 6254.

1391 Pearson V. K., Sephton M. A., Kearsley A. T., Bland P. A., Franchi I. A. and Gilmour I.  
 1392 (2002) Clay mineral-organic matter relationships in the early Solar System. *Meteoritics*  
 1393 *& Planetary Science* **37**, 1829-1833.

- 1394 Pignatelli I., Marrocchi Y., Vacher L. G., Delon R. and Gounelle M. (2016) Multiple  
1395 precursors of secondary mineralogical assemblages in CM chondrites. *Meteorit. Planet.*  
1396 *Sci.* **51**, 785– 805.
- 1397 Pignatelli I., Marrocchi Y., Mugnaioli E., Bourdelle F. and Gounelle M. (2017) Mineralogical,  
1398 crystallographic and redox features of the earliest stages of fluid alteration in CM  
1399 chondrites. *Geochim. Cosmochim. Acta* **209**, 106–122.
- 1400 Pizzarello S., Yarnes C.T., Cooper G.(2020). The Aguas Zarcas (CM2) meteorite: New  
1401 insights into early solar system organic chemistry. *Meteoritics & Planetary Science*.  
1402 55:1525-1538 <https://doi.org/10.1111/maps.13532>
- 1403 Popova O., P. Jenniskens, V. Emel'yanenko, A. Kartashova, E. Biryukov, S.  
1404 Khaibrakhmanov, V. Shuvalov, Y. Rybnov, A. Dudorov, V.I. Grokhovsky, D.D.  
1405 Badyukov, Q.Z. Yin, P.S. Gural, J. Albers, M. Granvik, L.G. Evers, J. Kuiper, V.  
1406 Kharlamov, A. Solovyov, Y. S. Rusakov, S. Korotkiy, I.Serdyuk, A.V.Korochantsev,  
1407 M.Y. Larionov, D. Glazachev, A.E. Mayer, G. Gisler, S.V. Gladkovsky, J. Wimpenny,  
1408 M.E. Sanborn, A. Yamakawa, K.L. Verosub, D.J. Rowland, S. Roeske, N.W. Botto,  
1409 J.M. Friedrich, M. Zolensky, L. Le, D. Ross, K. Ziegler, T. Nakamura, I. Ahn, J. Ik Lee,  
1410 Q. Zhou, X.H. Li, Q.L. Li, Y. Liu, G.Q. Tang, T. Hiroi, D. Sears, I.A. Weinstein, A.S.  
1411 Vokhmintsev, A.V. Ishchenko, Ph. Schmitt-Kopplin, N. Hertkorn, K. Nagao, M.K.  
1412 Haba, M. Komatsu, T. Mikouchi (2013) (The Chelyabinsk Airburst Consortium).  
1413 Chelyabinsk Airburst, Damage Assessment, Meteorite Recovery and Characterization.  
1414 *Science* **342**, 1069-1073.
- 1415 Quirico, E., Orthous-Daunay, F.-R., Beck, P., Bonal, L., Brunetto, R., Dartois, E., Pino, T.,  
1416 Montagnac, G., Rouzaud, J.-N., Engrand, C. and Duprat, J. (2014) Origin of insoluble  
1417 organic matter in type 1 and 2 chondrites: New clues, new questions. *Geochim.*  
1418 *Cosmochim. Acta* **136**, 80-99.
- 1419 Quirico E., Bonal L. Beck P., Alexander C. M. O. D., Yabuta H., Nakamura T., Nakato A.,  
1420 Flandinet L., Montagnac G., Schmitt-Kopplin P. and Herd C. D. K. (2018) Prevalence  
1421 and nature of heating processes in CM and C2-ungrouped chondrites as revealed by  
1422 insoluble organic matter. *Geochim. Cosmochim. Acta* **241**, 17-37.



- 1423 Ruf A., B.Kanawati, N. Hertkorn, Q.-Z. Yin, F. Moritz, M. Harir, M. Lucio, B.Michalke,  
1424 J.Wimpenny, S. Shilobreeva, B.Bronsky, V.Saraykin, Z.Gabelica, R.D Gougeon,  
1425 E.Quirico, S.Ralew, T.Jakubowski, H.Haack, M.Gonsior, P.Jenniskens, N.W Hinman,  
1426 Ph. Schmitt-Kopplin (2017) Previously unknown class of metalorganic compounds  
1427 revealed in meteorites. *PNAS* **114** (11), 2819-2824.
- 1428 Rubin A. E. and Wasson J. T. (1986) Chondrules in the Murray CM2 meteorite and  
1429 compositional differences between CM-CO and ordinary chondrite chondrules.  
1430 *Geochim. Cosmochim. Acta* **50**, 307-315.
- 1431 Rubin A. E., Trigo-Rodríguez J. M., Huber H., and Wasson J. T. (2007) Progressive aqueous  
1432 alteration of CM carbonaceous chondrites. *Geochim. Cosmochim. Acta* **71**, 2361-2382.
- 1433 Schmitt-Kopplin Ph., Gabelica Z., Gougeon, R.D., Fekete, A., Kanawati, B., Harir, M.,  
1434 Gebefuegi, I., Eckel G., and Hertkorn N. (2010) High molecular diversity of  
1435 extraterrestrial organic matter in Murchison meteorite revealed 40 years after its fall.  
1436 *Proceedings of the National Academy of Sciences* **107**(7), 2763-2768.
- 1437 Schmitt-Kopplin Ph., Harir M., Kanawati B., Tziotis D., Hertkorn N., and Gabelica Z. (2012)  
1438 Chemical footprint of the solvent soluble extraterrestrial organic matter occluded in  
1439 Soltmany ordinary chondrite. *Meteorite Journal*, Special issue *Soltmany* **1-2**, 79-92.
- 1440 Schrader D., Nagashima K., Krot A., Ogliore R., Yin Q.-Z., Amelin Y., Stirling C., and  
1441 Kaltenbach A. 2017. Distribution of <sup>26</sup>Al in the CR chondrite chondrule-forming region  
1442 of the protoplanetary disk. *Geochim. Cosmochim. Acta* **201**, 275–302.
- 1443 Schneider J. M., Burkhardt C., Marrocchi Y., Brennecka A. and Kleine T. (2020) Early  
1444 evolution of the solar accretion disk inferred from Cr-Ti-O isotopes in individual  
1445 chondrules. *Earth Planet. Sci. Lett.* **551**, 116585.
- 1446 Stöffler D., Bischoff A., Buchwald V., and Rubin A. E. (1988) Shock effects in meteorites. In  
1447 Meteorites and the Early Solar System (eds. J.F. Kerridge and M. S. Matthews), *The*  
1448 *University of Arizona Press, Tucson* 165-202.
- 1449 Takeichi, Y., Inami, N., Suga, H., Miyamoto, C., Ueno, T., Mase, K., Takahashi, Y. and Ono,  
1450 K. (2016) Design and performance of a compact scanning transmission X-ray  
1451 microscope at the Photon Factory. *Rev. Sci. Instrum.* **87**, 013704.

1452 Terzieva, R. and Herbst, E. (2000) The possibility of nitrogen isotopic fractionation in  
1453 interstellar clouds. *Monthly Notices of the Royal Astronomical Society* **317**, 563-568.

1454 Thiemens M. H. (1999) Mass-independent isotope effects in planetary atmospheres and the  
1455 early Solar System. *Science* **283**, 341-345.

1456 Tonui E., Zolensky M., Hiroi T., Nakamura T., Lipschutz M. E., Wang M.-S. and Okudaira K.  
1457 (2014) Petrographic, chemical and spectroscopic evidence for thermal metamorphism in  
1458 carbonaceous chondrites I: CI and CM chondrites. *Geochim. Cosmochim. Acta* **126**,  
1459 284-306.

1460 Toppania a., Libourela g., Robertf., and Ghanbajad j. (2006) Laboratory condensation of  
1461 refractory dust in protosolar and circumstellar conditions. *Geochimica et Cosmochimica*  
1462 *Acta* **70**(19):5035-5060

1463 Trinquier A., Elliott T., Ulfbeck D., Coath C., Krot A.N., and Bizzarro M. (2009) Origin of  
1464 nucleosynthetic isotope heterogeneity in the solar protoplanetary disk. *Science* **324**,  
1465 374-376.

1466 Van Kooten E., Cavalcante L., Wielandt D., and Bizzarro M. (2020) The role of Bells in the  
1467 continuous accretion between the CM and CR chondrite reservoirs. *Meteoritics &*  
1468 *Planetary Science* **55**, 575-590.

1469 Van Schmus W. R. and Hayes J. M. (1974) Chemical and petrologic correlations among  
1470 carbonaceous chondrites. *Geochim. Cosmochim. Acta* **38**, 47-64.

1471 Warren P. H., (2011) Stable-isotopic anomalies and the accretionary assemblage of the Earth  
1472 and Mars: A subordinate role for carbonaceous chondrites. *Earth. Planet. Sci. Lett.* **311**,  
1473 93-100

1474 Watkins J.M., Lammers L., Ryerson F.J., and Depaolo D. J. (2013) The influence of kinetics  
1475 on the oxygen isotope composition of calcium carbonate. *Earth. Planet. Sci. Lett* **375**,  
1476 349-360.

1477 Wasson, J.T., and Kallemeyn, G.W. (1988) Composition of chondrites. *Philosophical*  
1478 *Transactions of the Royal Society of London*, A325, 535–544.

1479 Weisberg M. K., Prinz M., Clayton R. N., and Mayeda T. K. (1993). The CR (Renaazo-type)  
1480 carbonaceous chondrite group and its implications. *Geochimica et Cosmochimica Acta*  
1481 **57**, 1567-1586.

1482 Yabuta H., Williams L. B., Cody G. D., Alexander C. M. O. D. and Pizzarello S. (2007) The  
1483 insoluble carbonaceous material of CM chondrites: A possible source of discrete  
1484 organic compounds under hydrothermal conditions. *Meteoritics & Planetary Science* **42**,  
1485 37-48.

1486 Yamakawa A., Yamashita K., Makishima A. and Nakamura E. (2010) Chromium isotope  
1487 systematics of achondrites: Chronology and isotopic heterogeneity of the inner Solar  
1488 System bodies. *Astrophys. J.* **720**, 150–154.

1489 Yesiltas M., Peale R. E., Unger M., Sedlmair J. and Hirschmugl C. J. (2015) Organic and  
1490 inorganic correlations for Northwest Africa 852 by synchrotron-based Fourier transform  
1491 infrared microspectroscopy. *Meteoritics & Planetary Science* **50**, 1684-1696.

1492 Yesiltas M. and Kebukawa Y. (2016) Associations of organic matter with minerals in Tagish  
1493 Lake meteorite via high spatial resolution synchrotron-based FTIR microspectroscopy.  
1494 *Meteoritics & Planetary Science* **51**, 584-595.

1495 Yurimoto H., Ito M., and Nagasawa H. (1998) Oxygen isotope exchange between refractory  
1496 inclusion in Allende and solar nebula gas. *Science* **282**, 1874–1877.

1497 Vacher L. G., Marrocchi Y., Verdier-Paoletti M. J., Villeneuve J. and Gounelle M. (2016)  
1498 Inward radial mixing of interstellar water ices in the solar protoplanetary disk.  
1499 *Astrophys.J.* **827**, L1.

1500 Vacher L. G., Marrocchi Y., Villeneuve J., Verdier-Paoletti M. J. and Gounelle M. (2017)  
1501 Petrographic and C & O isotopic characteristics of the earliest stages of aqueous  
1502 alteration of CM chondrites. *Geochim. Cosmochim. Acta* **213**, 271–290.

1503 Vacher L.G., MarrocchiY., VilleneuveJ., Verdier-Paoletti M.J., and Gounelle M. (2018)  
1504 Collisional and alteration history of the CM parent body. *Geochim. Cosmochim. Acta*  
1505 **239**, 213-234.

1506 Vacher L.G., Truche L., Faure F., Tissandier L., Mosser-Ruck R., and Marrocchi Y. (2019)  
1507 Deciphering the conditions of tochilinite and cronstedtite formation in CM chondrites  
1508 from low temperature hydrothermal experiments. *Meteoritics & Planetary Science* **54**,  
1509 1870-1889.

1510 Vacher L.G., Piani L., Rigaudier T., Thomassin D., Florin G., Piralla M. & Marrocchi Y.  
1511 (2020) Hydrogen in chondrites: Influence of parent body alteration and atmospheric  
1512 contamination on primordial components. *Geochimica et Cosmochimica Acta* **281**, 53-  
1513 66, 10.1016/j.gca/2020.05.007

1514 Verdier-Paoletti M.J., Marrocchi Y., Avice G., Roskosz M., Gurenko A., and Gounelle M.  
1515 (2017) Oxygen isotope constraints on the alteration temperatures of CM chondrites.  
1516 *Earth Planet. Sci. Lett.* **458**, 273-281.

1517 Verdier-Paoletti M.J., Marrocchi Y., Vacher L.G., Gattacceca J., Gurenko A., Sonzogni C.,  
1518 and Gounelle M. (2019) Testing the genetic relationship between fluid alteration and  
1519 brecciation in CM chondrites. *Meteoritics & Planetary Science* **54**, 1692-1709.

1520 Vinogradoff V., Le Guillou C., Bernard S., Binet L., Cartigny P., Brearley A. J. and Remusat  
1521 L. (2017) Paris vs. Murchison: Impact of hydrothermal alteration on organic matter in  
1522 CM chondrites. *Geochimica et Cosmochimica Acta*. **212**, 234-252.

1523 Vollmer C., Leitner J., Kepaptsoglou D., Ramasse Q. M., King A. J., Schofield P. F., Bischoff  
1524 A., Araki T., and Hoppe P. (2020) A primordial <sup>15</sup>N-depleted organic component  
1525 detected within the carbonaceous chondrite Maribo. *Nature* 10, 2025.

1526 Zhang J., Dauphas N., Davis A. M., and Pourmand A. (2011) A new method for MC-ICPMS  
1527 measurement of Ti isotopic composition: identification of correlated isotope anomalies  
1528 in meteorites. *J. Anal., At. Spectrom.* **26**, 2197-2205.

1529 Zhang J., Dauphas N., Davis A. M., Leya I., and Fedkin A. (2012) The proto-Earth as a  
1530 significant source of lunar material., *Nature Geoscience* **5**, 251-255.

1531 Zolensky M.E., Barrett R.A., and Browning L. (1993) Mineralogy and composition of matrix  
1532 and chondrule rims in carbonaceous chondrites. *Geochim. Cosmochim. Acta* **57**, 3123-  
1533 3148.

1534 Zolensky M.E., Weisberg M.K., Buchanan P.C., and Mittlefehldt D.W. (1996) Mineralogy of  
1535 carbonaceous chondrite clasts in HED achondrites and the Moon. *Meteoritics &*  
1536 *Planetary Science* **31**, 518-537.

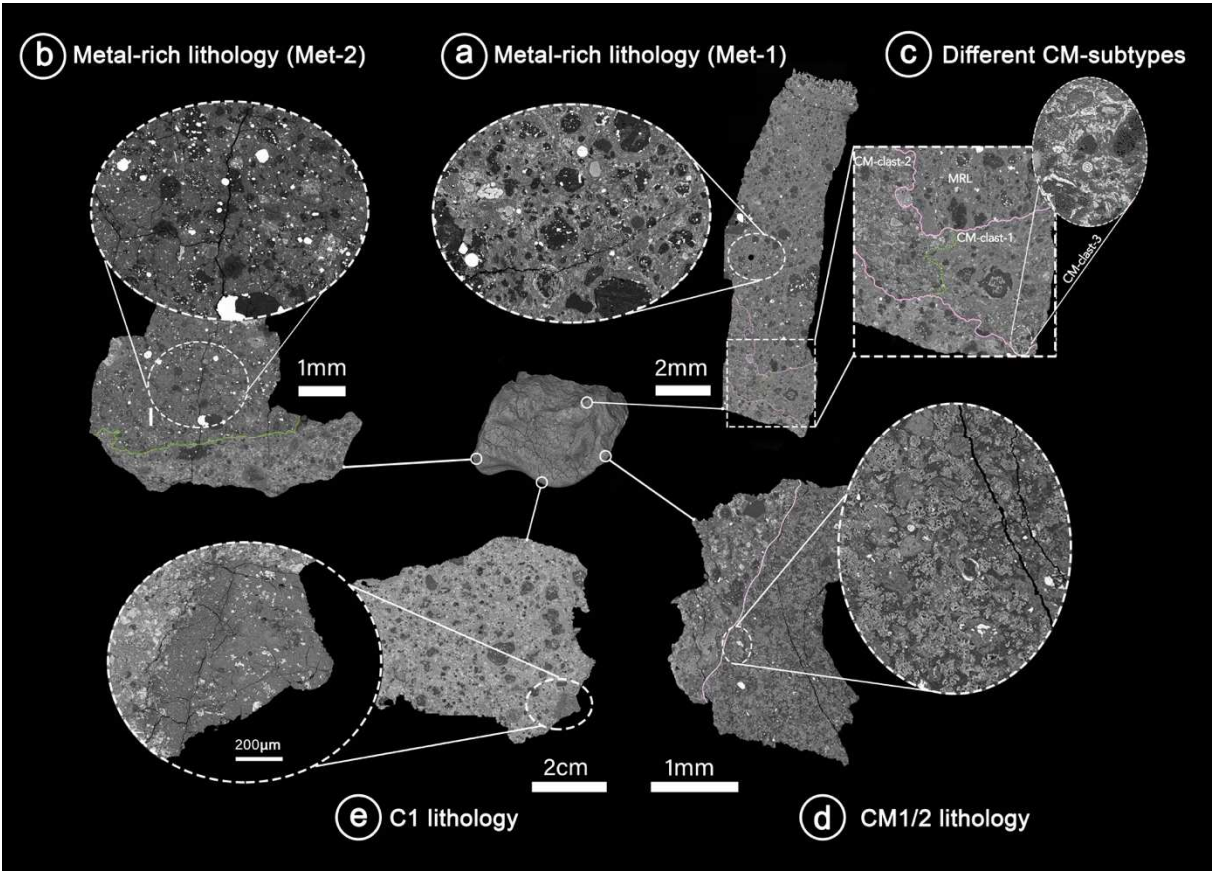
1537 Zolensky M.E., Mittlefehldt D.W., Lipschutz M.E., Wang M.-S., Clayton R.N., Mayeda T.,  
1538 Grady M.M., Pillinger C. and Barber D. (1997) CM chondrites exhibit the complete  
1539 petrologic range from type 2 to 1. *Geochimica et Cosmochimica Acta* **61**, 5099-5115.

1540 Zolensky M. and Ivanov. A. (2003) The Kaidun microbreccia meteorite: A harvest from the  
1541 inner and outer Asteroid belt. *Chem. Erde* **63**, 185-246.

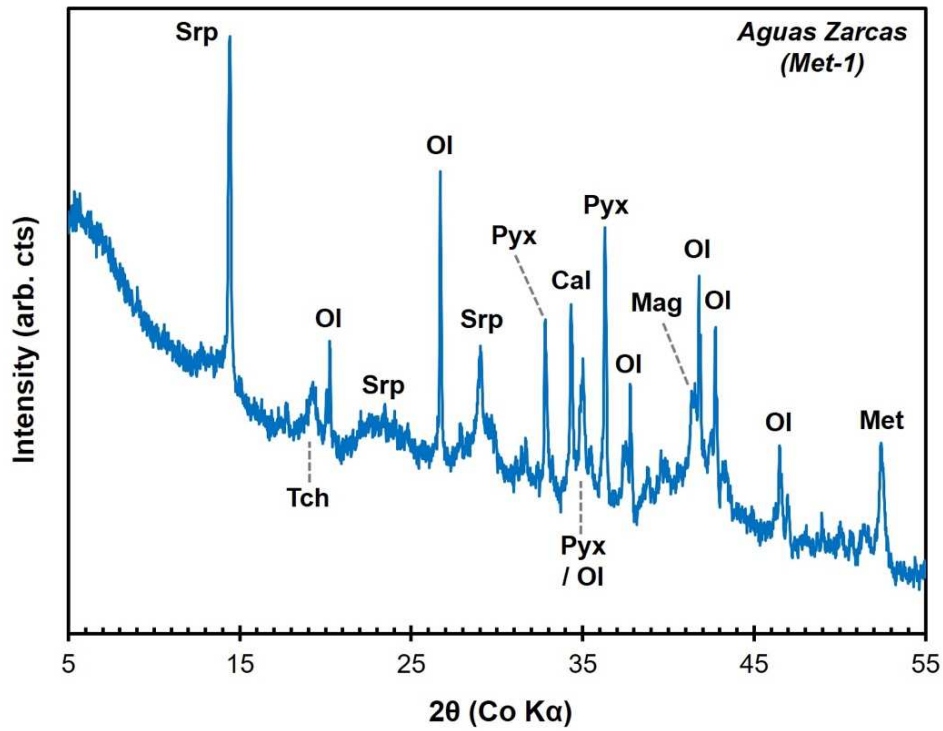
1542

1543

1544



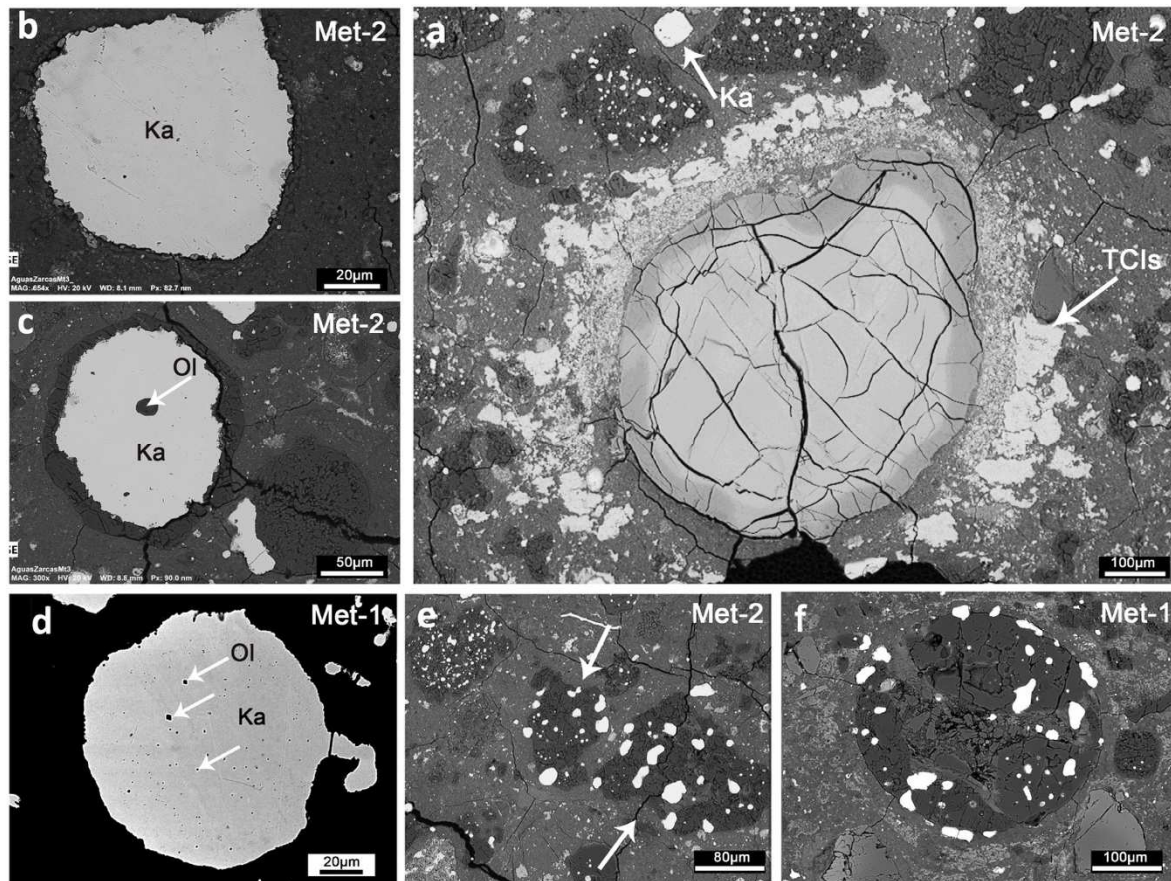
1546  
1547 Fig. 1: Backscattered electron (BSE) images of four thin sections show the brecciation of  
1548 Aguas Zarcas. (a) Met-1 is in the upper part, and the brecciated CM chondrite with clasts of  
1549 three CM subtypes are in the lower part (c). (b) Met-2 is on the left side. (d) The C1/2  
1550 lithology is in dark gray, and the CM lithology is in light grey. (e) The C1 lithology is on the  
1551 left side at the bottom. Lines indicate the boundaries between the different lithologies.



1552

1553 Fig. 2: XRD pattern for the Met-1 lithology of Aguas Zarcas, showing the main identified  
 1554 phases. (Ol: Olivine; Pyx: Pyroxene; Srp: Serpentine; Mag: Magnetite; Met: Metal; Tch:  
 1555 Tochilinite; Cal: Calcites).

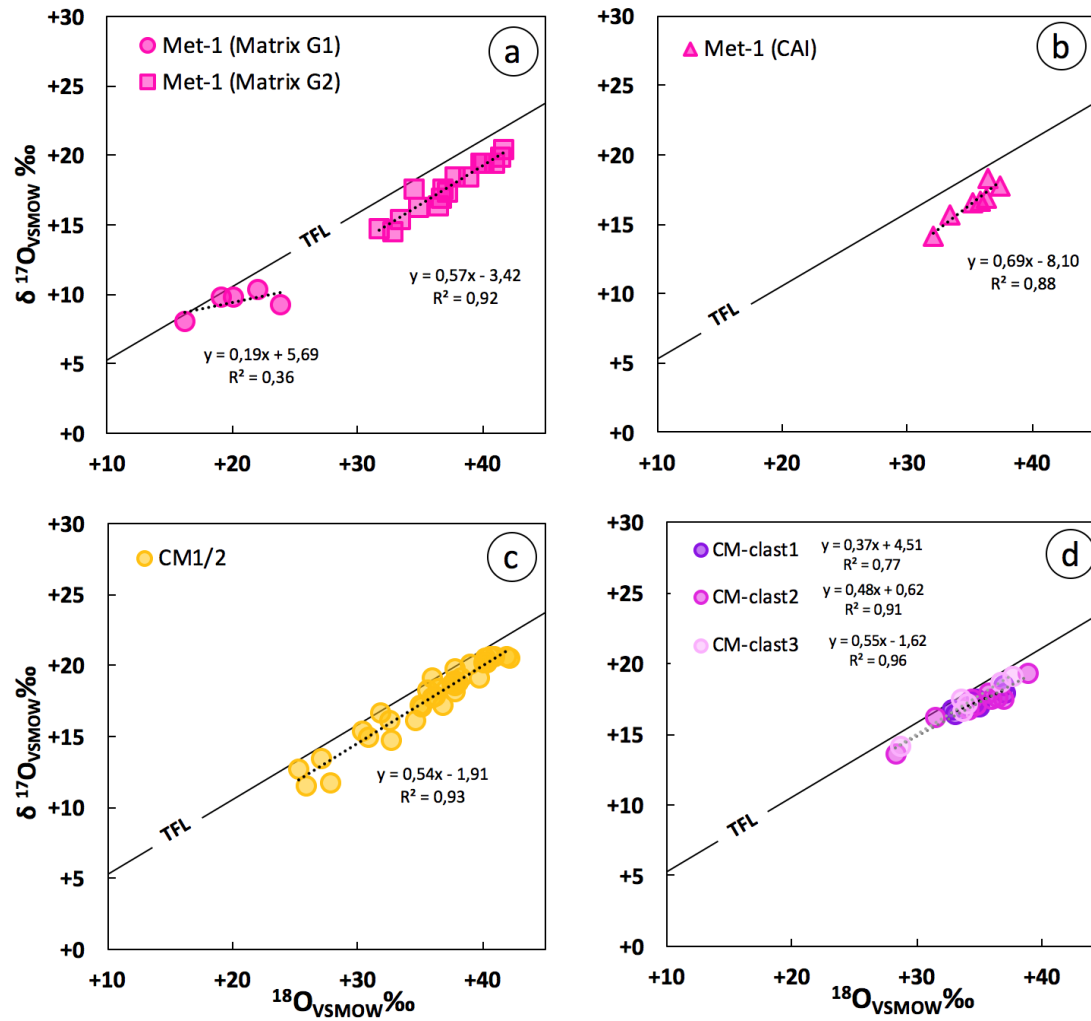
1556



1557

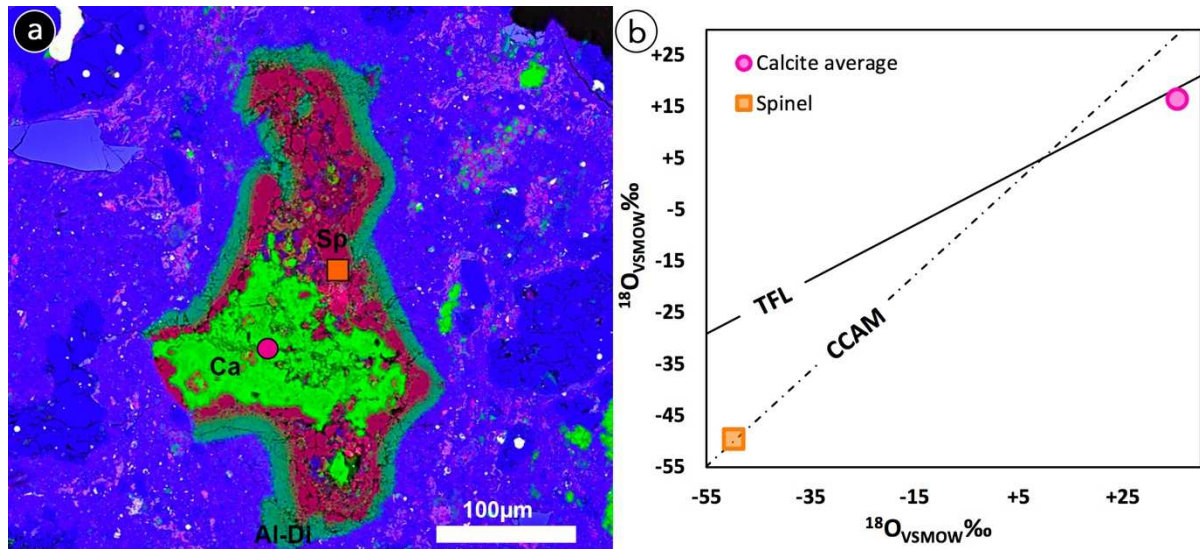
1558 Fig. 3: BSE images showing some characteristics and similarities between the Met-1 and Met-  
 1559 2 lithologies: (a) A highly altered object within the Met-2 lithology, composed of Fe, Ni, S,  
 1560 Cr and Mn, surrounded by compact TCIs. (b, c, d) Large metal blobs within both lithologies  
 1561 Met-1 and Met-2, similar to those occurring in CR chondrites (e.g., Weisberg et al., 1993;  
 1562 Bischoff et al., 1993). These grains of metal contain pores filled with either olivine or  
 1563 phyllosilicates in both lithologies (shown by arrows; compare Kerraouch et al., 2021). (e) The  
 1564 chondrules in the Met-2 lithology are often fragmented, containing abundant metal grains and  
 1565 completely lacking accretionary dust rims (Metzler et al., 1992). (f) Rimmed chondrules  
 1566 within the Met-1 lithology show rounded shapes, with metal grains outside and inside the  
 1567 chondrules. The matrix of the Met-2 lithology frequently shows cracks and fractures, which  
 1568 are very rare within Met-1. Ka: Kamacite; Ol: Olivine.





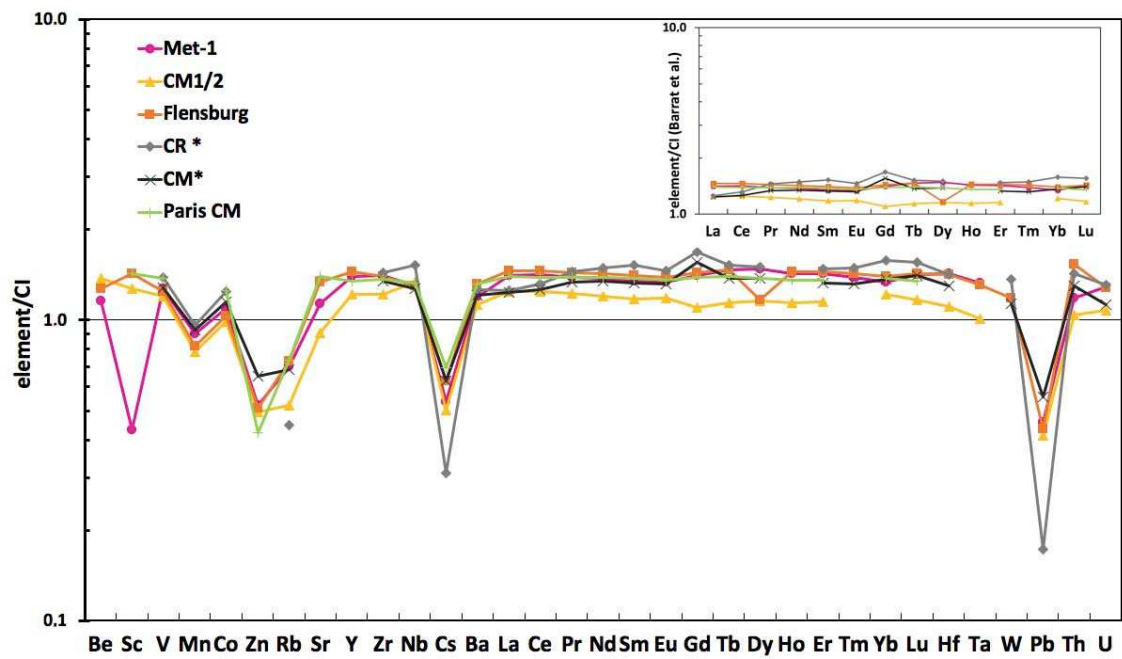
1569

1570 Fig. 4: Oxygen isotope diagrams of calcite in Aguas Zarcas: (a) Met-1, (b) CAI within the  
 1571 Met-1, (c) three CM clasts from Met-1 (d) CM1/2 lithology. TFL= terrestrial fractionation  
 1572 line.



1573

1574 Fig. 5: (a) Elemental map of the complex CAI within the Met-1 lithology (PL19125). Calcite-  
 1575 rich, spinel-bearing CAIs; (b) O isotope diagram of calcite and spinel. Color code: Al (red;  
 1576 mainly indicating spinel), Ca (green; related to calcite), and Mg (blue; typical element within  
 1577 the dust rim and matrix). TFL= terrestrial fractionation line; CCAM= carbonaceous chondrite  
 1578 anhydrous mineral.



1580

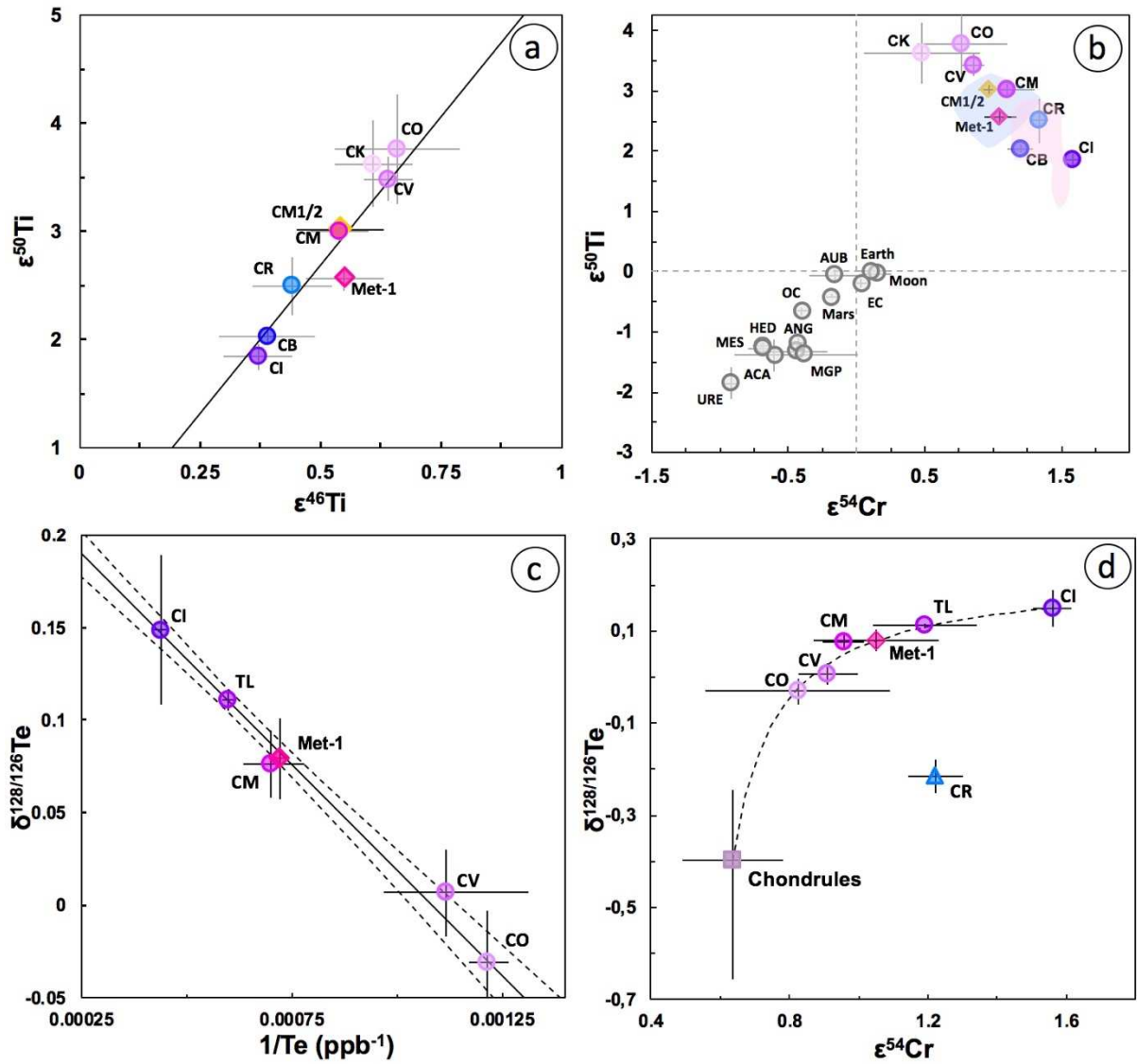
1581

1582

1583

1584

Fig. 6: Bulk composition of the metal-rich lithology of Aquas Zarcas compared to that of Flensburg (Bischoff et al., 2021) and the average (CM\* and CR\*) of other CM and CR chondrites (Braukmüller et al., 2018). For normalization, the CI values of Barrat et al., (2012) are used.



1585

1586 Fig. 7: Positions of the Met-1 and CM1/2 lithologies in (a)  $\epsilon^{50}\text{Ti}$  vs.  $\epsilon^{46}\text{Ti}$ , (b)  $\epsilon^{50}\text{Ti}$  vs.  $\epsilon^{54}\text{Cr}$ ,  
 1587 (c)  $\delta^{128/126}\text{Te}$  vs.  $1/\text{Te}$ , and (d)  $\delta^{128/126}\text{Te}$  vs.  $\epsilon^{54}\text{Cr}$  space. The Ti isotopic composition of Met-1  
 1588 overlaps with data reported for CM and CR chondrites, while its Cr and Te isotopic  
 1589 compositions are similar to CM chondrites only. Titanium, Cr, and Te isotope data for the  
 1590 CM1/2 lithology imply a close genetic link to CM chondrites. Literature data for Ti and Cr  
 1591 were taken from the compilation published by Burkhardt et al., (2019), and the slope and  
 1592 intercept of the bulk meteorite regression in  $\epsilon^{50}\text{Ti}$  vs.  $\epsilon^{46}\text{Ti}$  space was taken from Trinquier et  
 1593 al., (2009). The blue and pink regions represent CM chondrites and CR chondrites,  
 1594 respectively, literature data from Torrano et al., (2021). The  $\delta^{128/126}\text{Te}$ – $1/\text{Te}$  mixing line  
 1595 defined by carbonaceous chondrite groups and Te literature data were taken from Hellmann et  
 1596 al., (2020). TL: Tagish Lake.

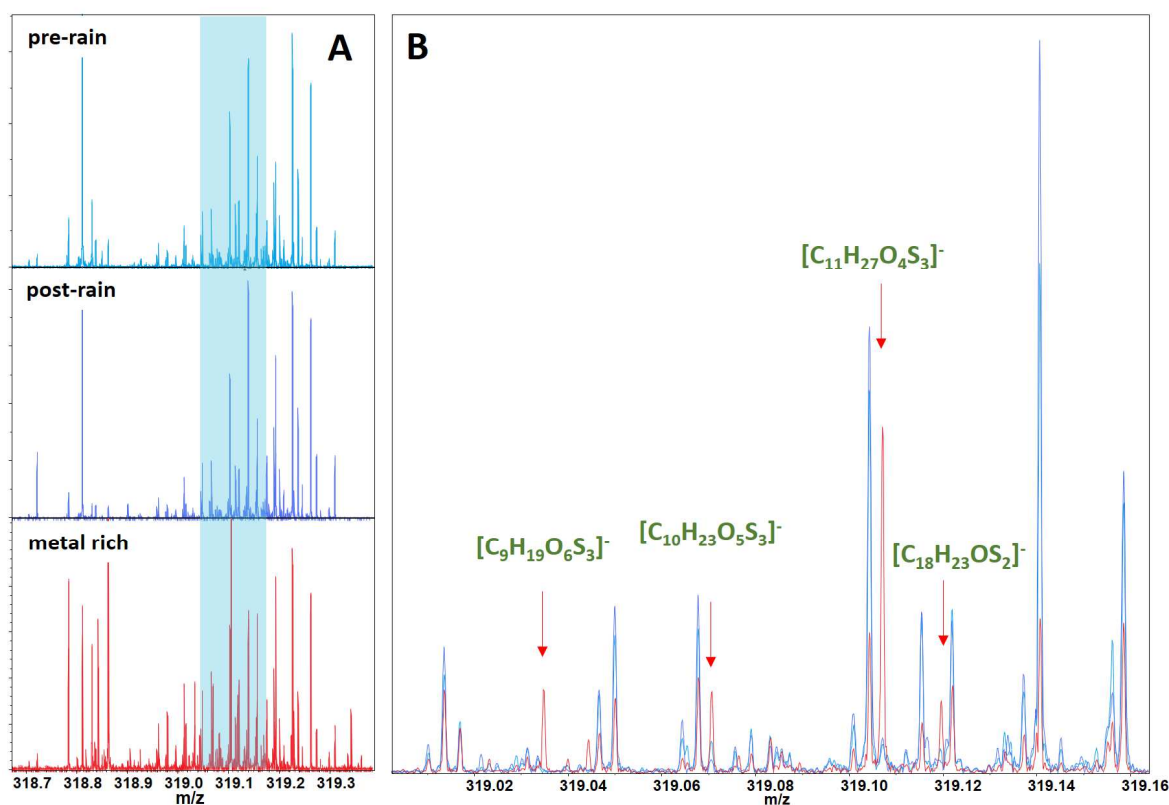


Fig. 8: FTICR-MS spectra detail in nominal mass 319 showing (a) the high abundance of signals in the Aguas Zarcas pre-rain sample, post-rain sample, and the metal-rich lithology Met-1. (b) The signature is similar between the pre- and post-rain samples, and a relative increase of polysulfidic compounds appears in the Met-1 fraction.

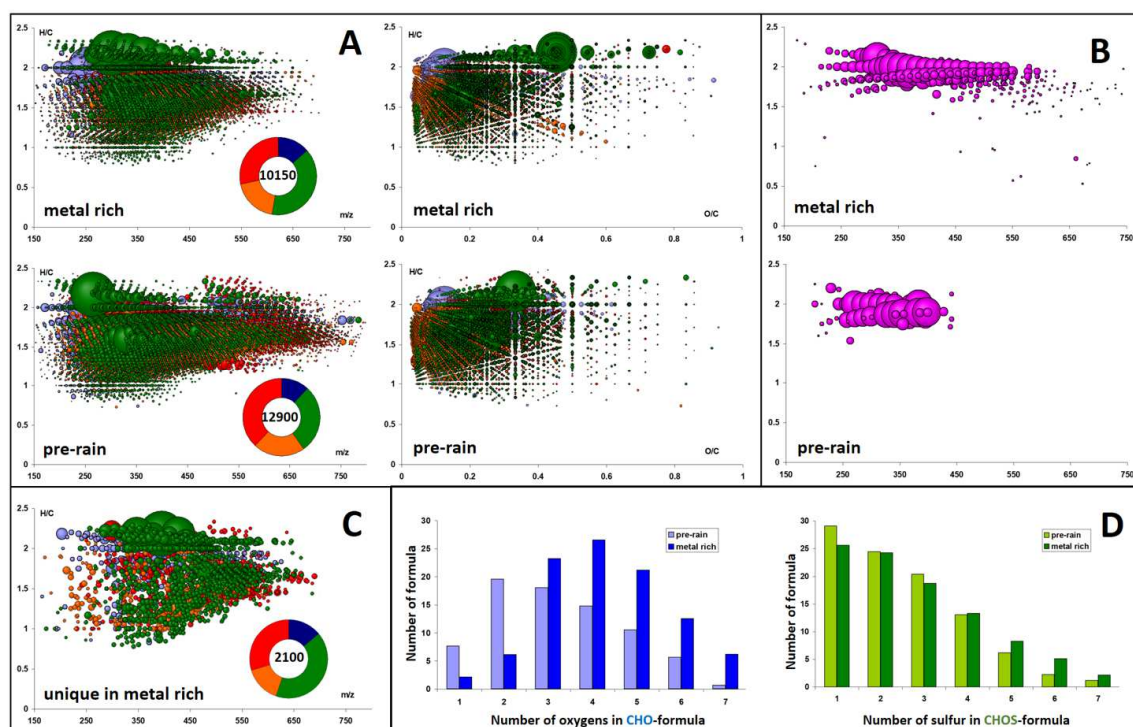
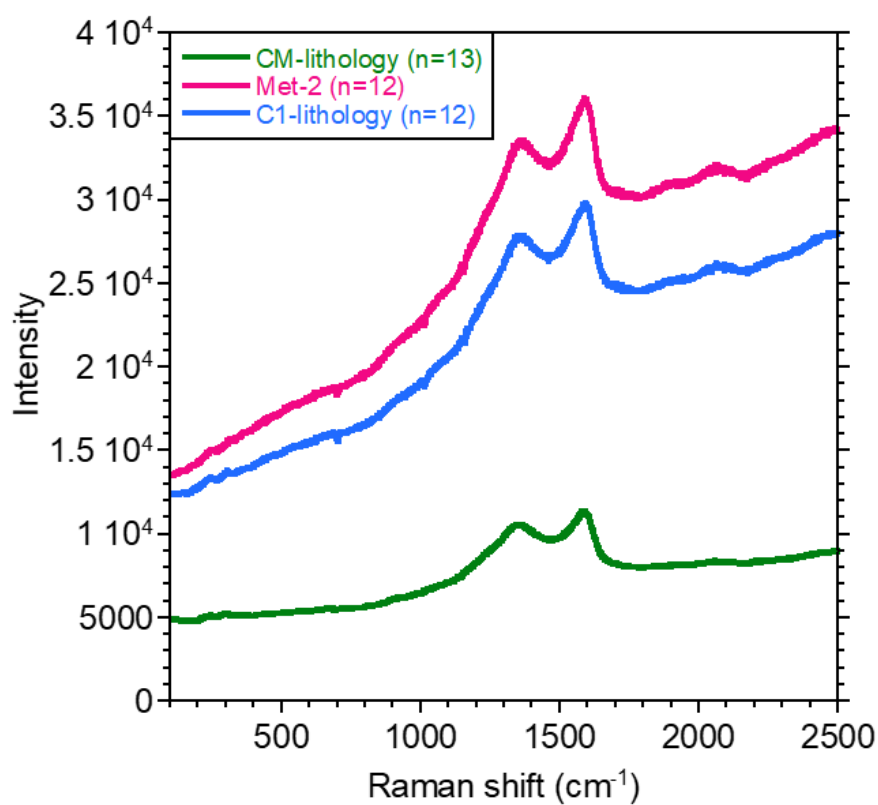
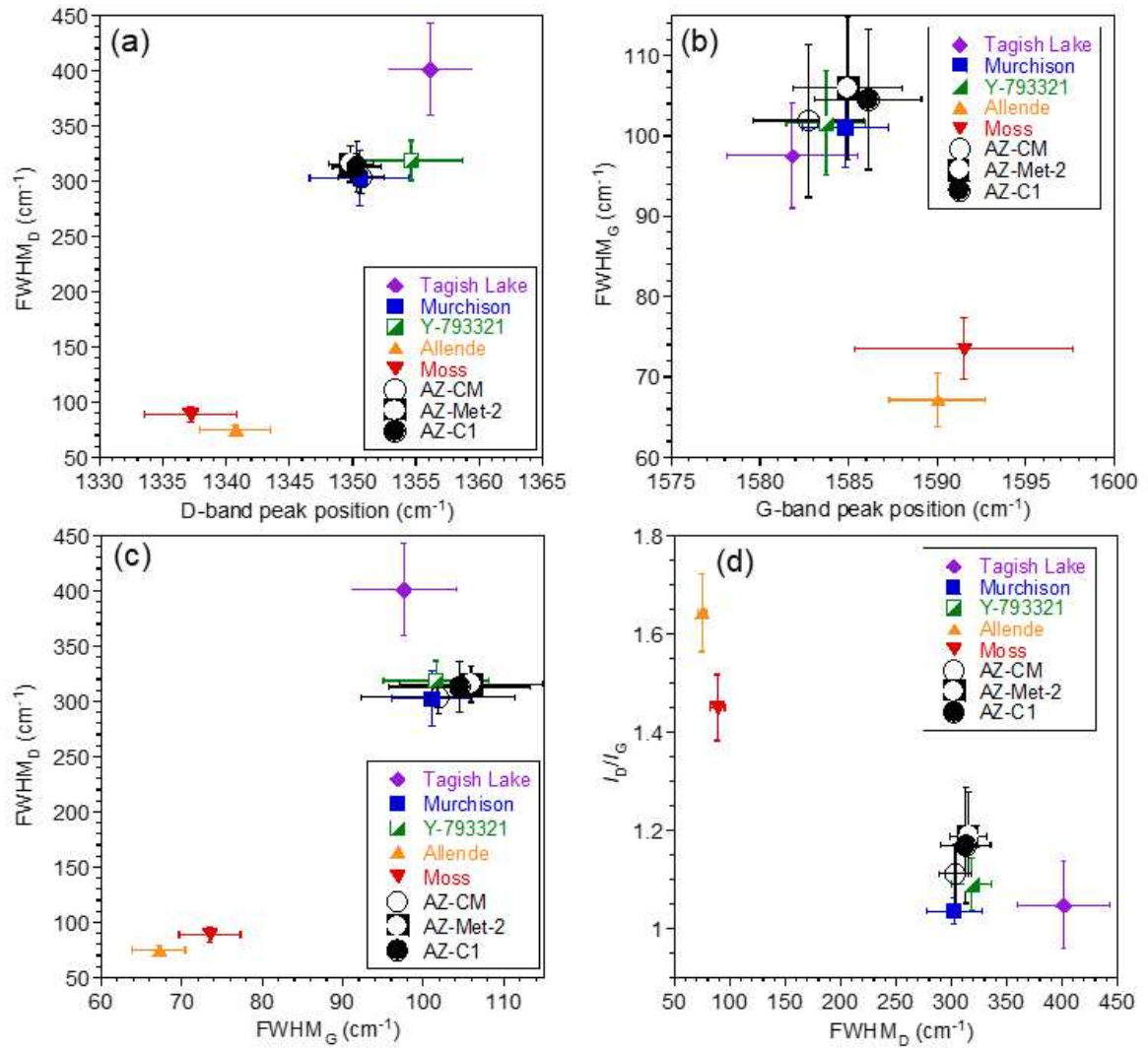


Fig. 9: FTICR-MS compositional profiling of the Aguas Zarcas pre-rain sample and the Met-1 lithology. (a) van Krevelen diagrams of the whole C, H, N, O, S compositional space (Color code as CHO=blue, CHNO=orange, CHOS=green, CHNOS=red; the bubble size indicates relative abundances of the molecular species). Also shown are the (b) organomagnesium compounds (CHOMg), (c) the van Krevelen diagram of the unique species in the metal-rich fraction Met-1, and (d) abundance of oxygen atoms in the CHO compounds and abundance of sulfur atoms in the CHOS compounds.



1611

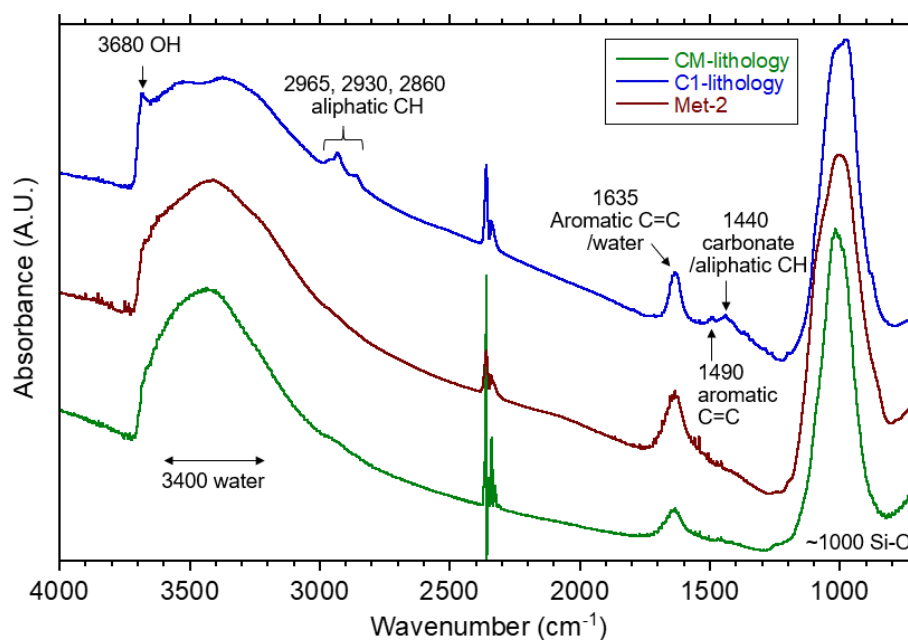
1612 Fig. 10: Raman spectra recorded at 532 nm of carbon-rich spots (average of  $n$  spots from each  
 1613 lithology) in the CM lithology, Met-2, and C1 lithology from the Aguas Zarcas meteorite.



1614

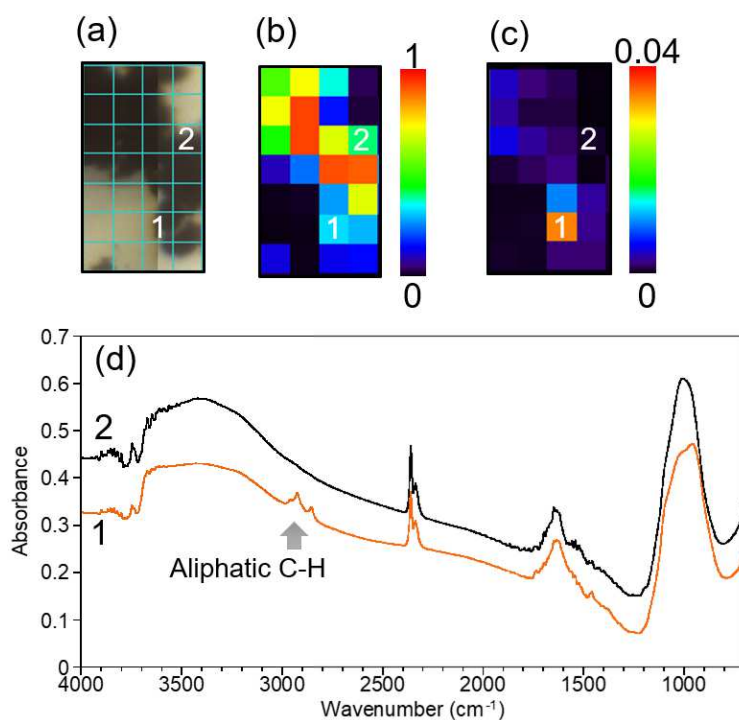
1615 Fig. 11: The Raman D and G band parameters. (a) the D band peak position vs. the full width  
 1616 half-maximum (FWHM) of D band, (b) the G band peak position vs. FWHM of G band, (c)  
 1617 FWHM of G band vs. FWHM of D band, and (d) FWHM of D band vs. the peak intensity  
 1618 ratio of D and G bands ( $I_D/I_G$ ). The data from Murchison (CM2), Tagish Lake (C2-ung),  
 1619 Allende (CV3.2), Moss (CO3.6), and Y-793321 (CM-heated) is from Kiryu et al., (2020).





1620

1621 Fig. 12: Infrared absorption spectra of the Aguas Zarcas meteorite. A sharp peak at 3680 cm<sup>-1</sup>  
 1622 is assigned to phyllosilicate O-H; a broad peak at ~3400 cm<sup>-1</sup> is assigned to  
 1623 adsorbed/interlayer water. The peaks at 2965, 2930, and 2860 cm<sup>-1</sup> are assigned to C-H  
 1624 asymmetric stretching of CH<sub>3</sub>, C-H asymmetric stretching of CH<sub>2</sub>, and blended C-H  
 1625 symmetric stretching of CH<sub>3</sub> and CH<sub>2</sub>, respectively. A peak at 1635 cm<sup>-1</sup> is due to aromatic  
 1626 C=C and adsorbed/interlayer water. Peaks at 1490 and 1440 cm<sup>-1</sup> are likely due to aromatic  
 1627 C=C and carbonate/aliphatic C-H bending, respectively. A large peak at ~1000 cm<sup>-1</sup> is  
 1628 assigned to Si-O stretching of silicates. Note that the feature at ~2360 cm<sup>-1</sup> is due to  
 1629 atmospheric CO<sub>2</sub>.



1630

1631 Fig. 13: Infrared spectroscopic mapping of the Met-2 lithology. (a) Optical microscope image  
 1632 of the mapping area. The pixel size is  $50 \times 50 \mu\text{m}^2$ . (b) Peak intensity map of Si-O at  $1000$   
 1633  $\text{cm}^{-1}$  with a linear baseline between  $1200$ - $800 \text{ cm}^{-1}$ . (c) peak intensity map of aliphatic C-H  
 1634 at  $2930 \text{ cm}^{-1}$  with a linear baseline between  $3000$ - $2800 \text{ cm}^{-1}$ . (d) IR spectra from areas #1 and  
 1635 #2.

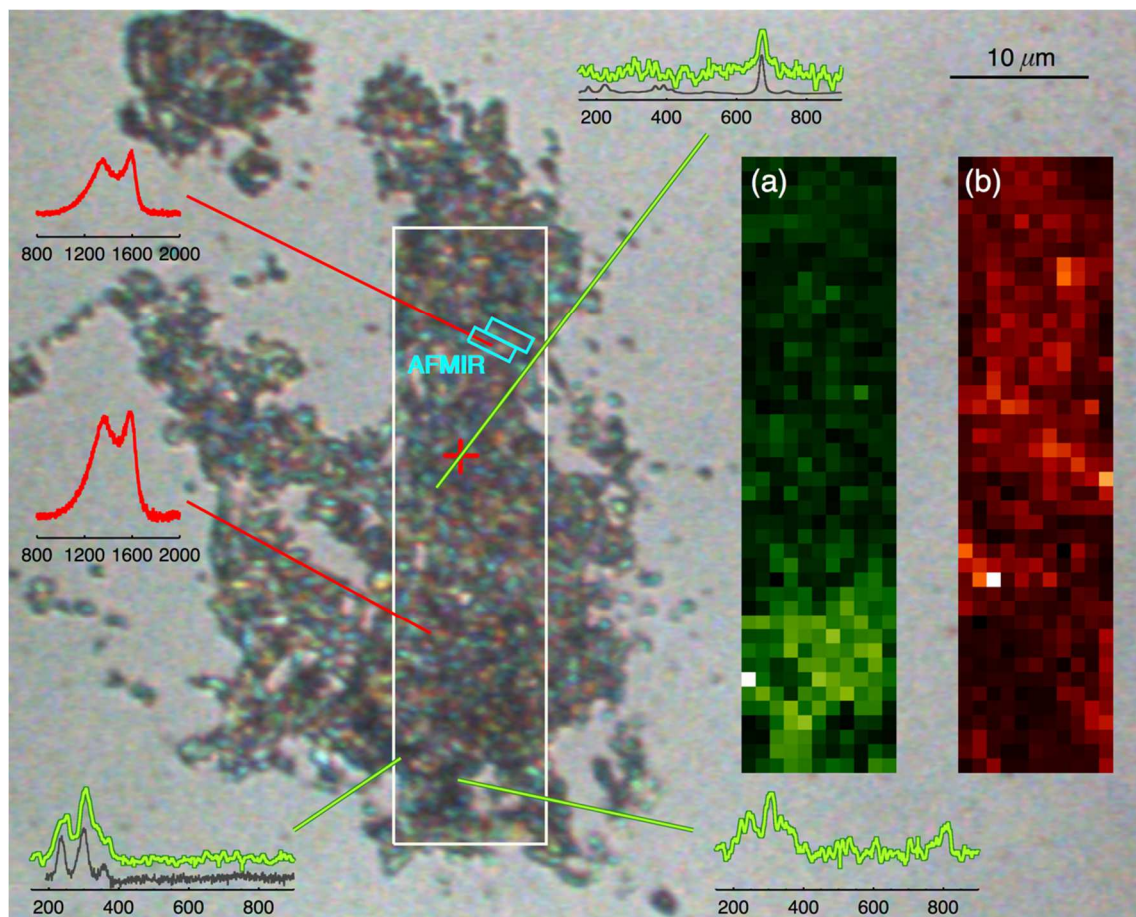


Fig. 14: Raman mapping on the same microtome section as used for AFM-IR. (a) Raman mapping for the 350-200  $\text{cm}^{-1}$  range (tochilinite). (b) Raman mapping for the 1650-1200  $\text{cm}^{-1}$  range (organics). The region mapped with Raman is shown by a white rectangle overlaid on an optical image of the section with the Raman spectra at the region of interest (see text for details). The locations where the two AFM-IR maps were acquired are shown by light blue rectangles.

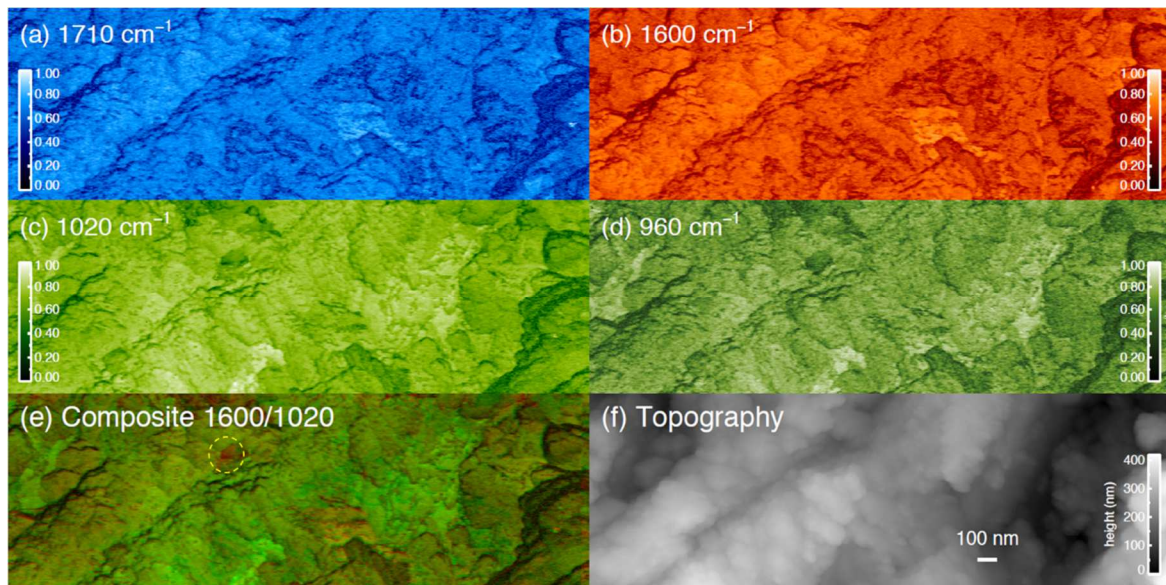


Fig. 15: AFM-IR study of a first area (1×3 microns) of Aguas Zarcas CM lithology: (a, b) IR maps at 1710 cm<sup>-1</sup> and 1600 cm<sup>-1</sup>; (c, d) IR maps corresponding to the silicates at two different frequencies (1020 cm<sup>-1</sup> and 960 cm<sup>-1</sup>); (e) composite image obtained by combining the IR mapping signals at 1600 cm<sup>-1</sup> and 1020 cm<sup>-1</sup>; the yellow dotted circle highlights an area that appears richer in organic matter; (f) AFM topography (height) of the studied area.

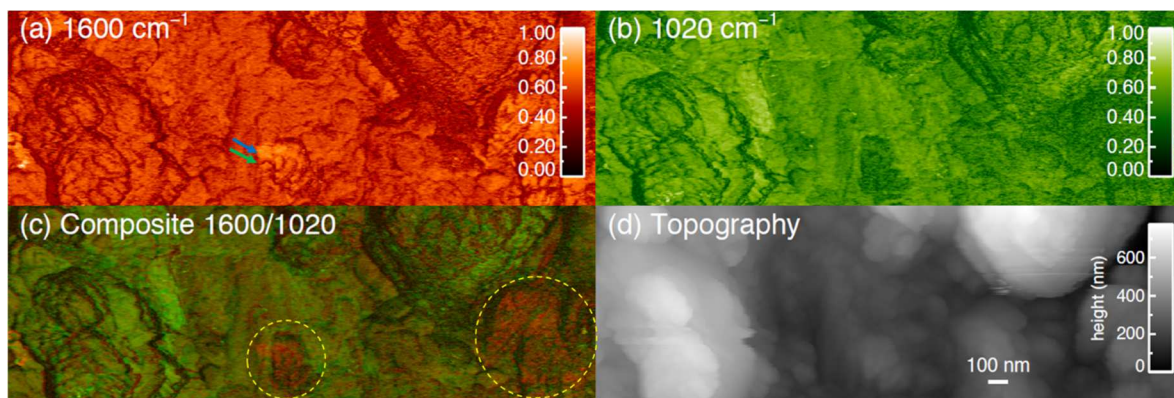
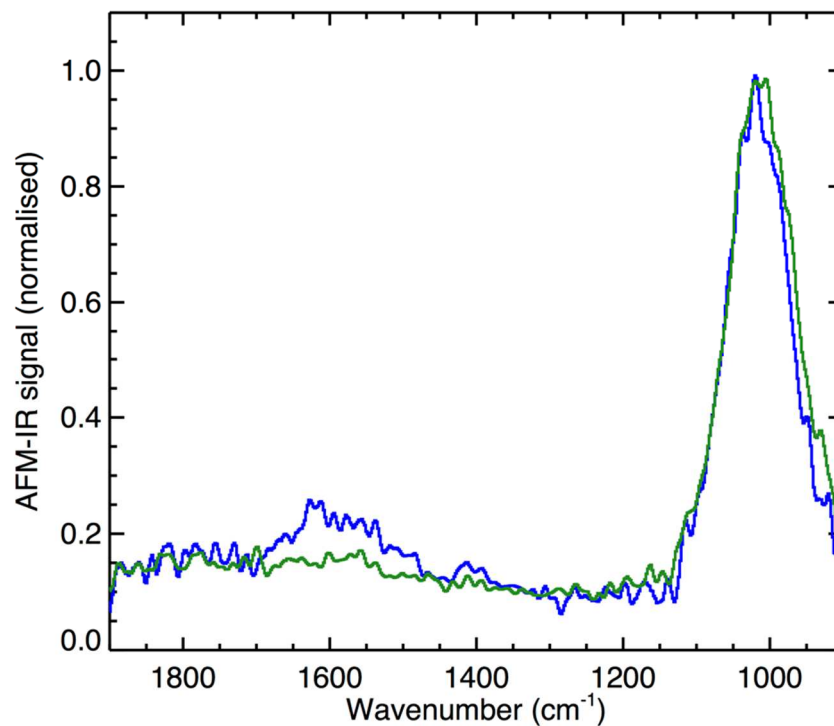


Fig. 16: AFM-IR study of a second area (1×3 microns) of Aguas Zarcas CM lithology: (a, b) IR maps at 1600 cm<sup>-1</sup> (main signature of the organic fraction) and 1020 cm<sup>-1</sup> (main signature of the silicates); (c) composite image obtained by combining both signals from IR maps at 1600 cm<sup>-1</sup> and 1020 cm<sup>-1</sup>; yellow dotted circles highlight areas that appear richer in organic matter; (d) AFM topography (height) of the studied area.



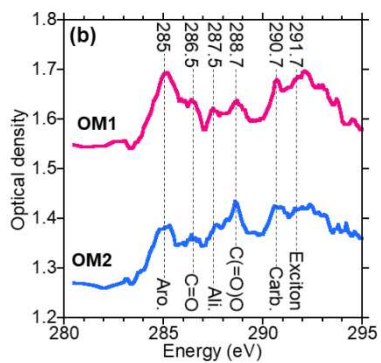
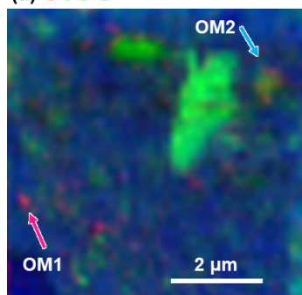


1656

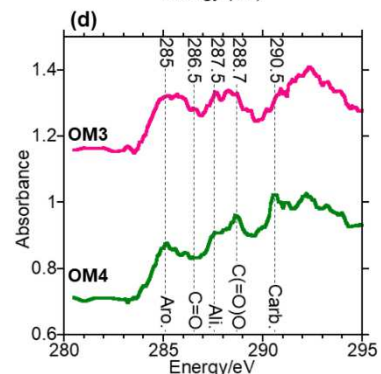
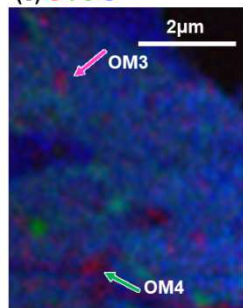
1657 Fig. 17: Tapping AFM-IR spectra of two different positions in the Aguas Zarcas CM  
 1658 lithology, selected for their different responses in the AFM-IR maps. The localization of the  
 1659 spectra is indicated with corresponding colored arrows in Fig. 13. The blue curve is offset by  
 1660 a value of one for clarity. See text for details.

# Met-2

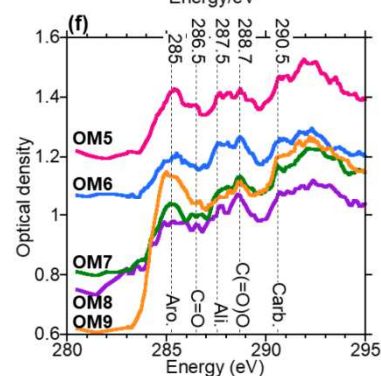
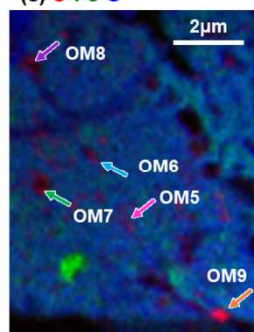
## (a) C-Fe-O



## (c) C-Fe-O

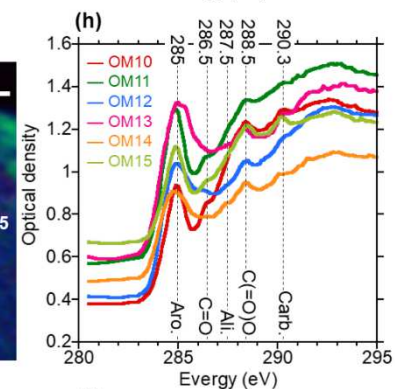
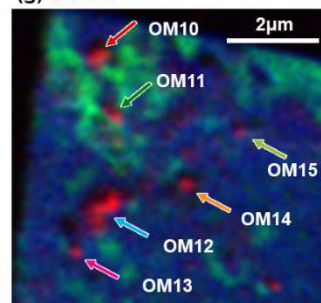


## (e) C-Fe-O



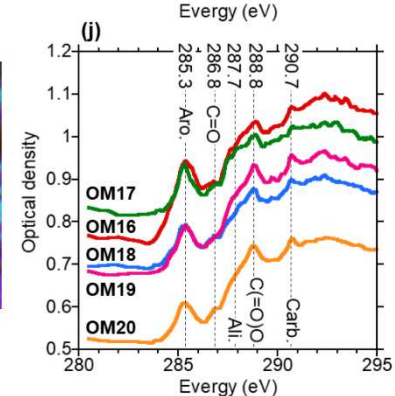
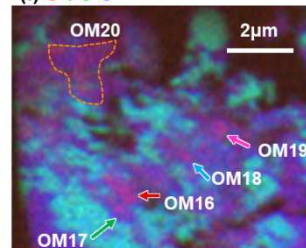
# CM-lithology

## (g) C-Fe-O

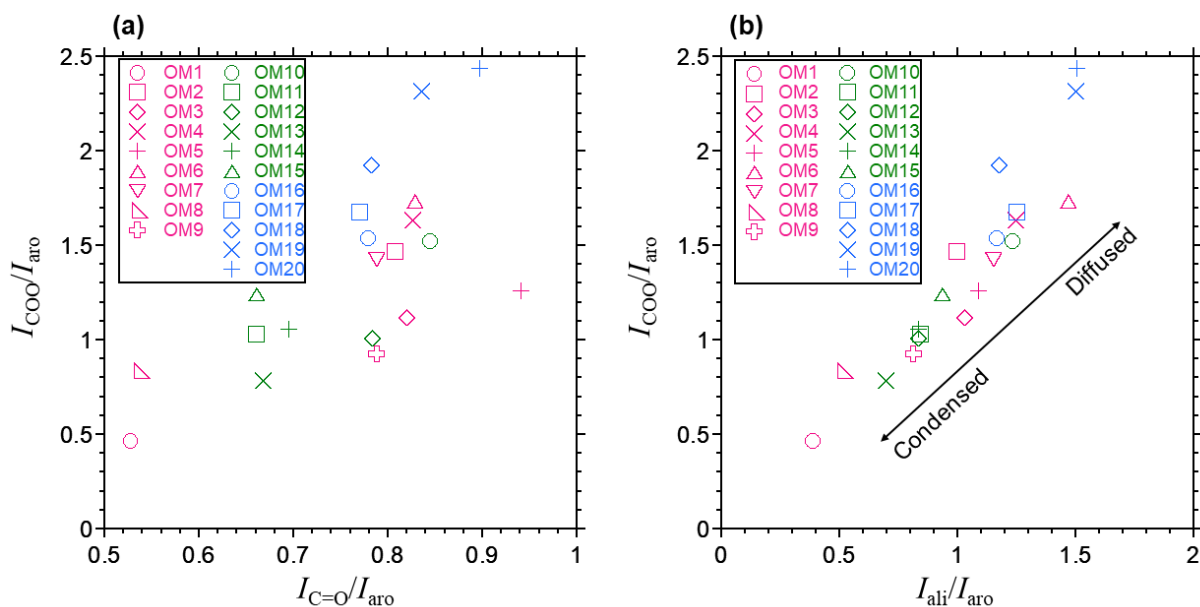


# C1-lithology

## (i) C-Fe-O



1662 Fig. 18: (a, c, e) STXM C–Fe–O elemental maps of the FIB sections from Met-2, and (b, d, f)  
1663 C-XANES spectra of the organic particles OM1 to OM9 (indicated by arrows in a, c, e). (g)  
1664 STXM C–Fe–O elemental map of an FIB section from the CM lithology, and (h) C-XANES  
1665 spectra of the organic particles OM10 to OM15 (indicated by arrows in g). (i) STXM C–Fe–O  
1666 elemental map of an FIB section from the C1 lithology, and (j) C-XANES spectra of the  
1667 organic particles OM16 to OM20 (indicated by arrows in i).

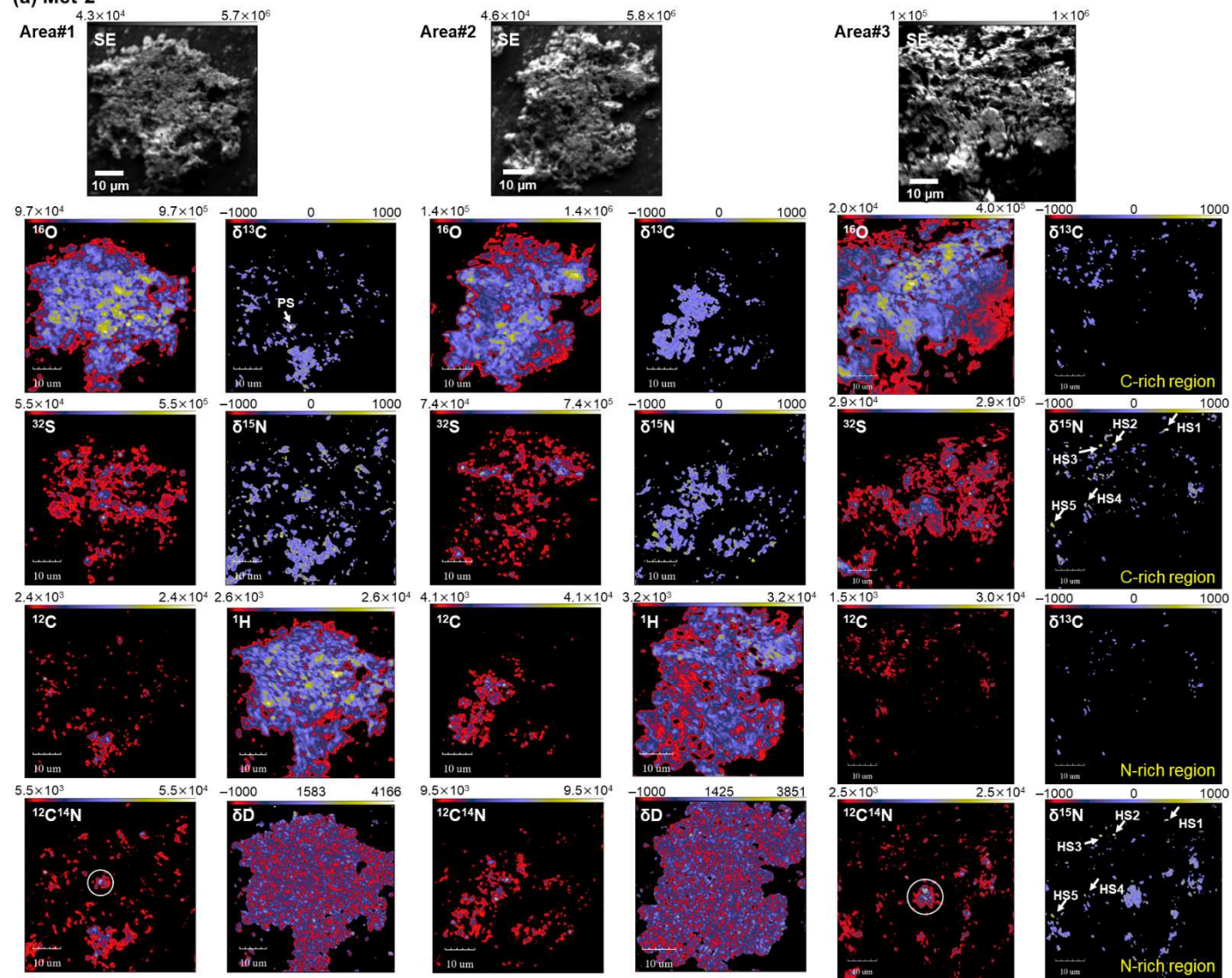


1668

1669 Fig. 19: (a) C-XANES C(=O)O (288.5-288.8 eV) over aromatic (285.0-385.3 eV) peak  
 1670 intensity ratios ( $I_{\text{COO}}/I_{\text{aro}}$ ) and C=O (286.5-286.8 eV) over aromatic peak intensity ratios  
 1671 ( $I_{\text{C=O}}/I_{\text{aro}}$ ). (b) C-XANES C(=O)O over aromatic peak intensity ratios ( $I_{\text{COO}}/I_{\text{aro}}$ ) and aliphatic  
 1672 (287.5-287.6 eV) over aromatic peak intensity ratios ( $I_{\text{ali}}/I_{\text{aro}}$ ). OM1 to OM9 are from Met-2,  
 1673 OM10 to OM15 are from CM lithology, and OM16 to OM20 are from C1 lithology.  
 1674 Condensed OM tends to be aromatic rich, and diffused OM tends to aromatic poor.



(a) Met-2



**(b) C1-lithology**

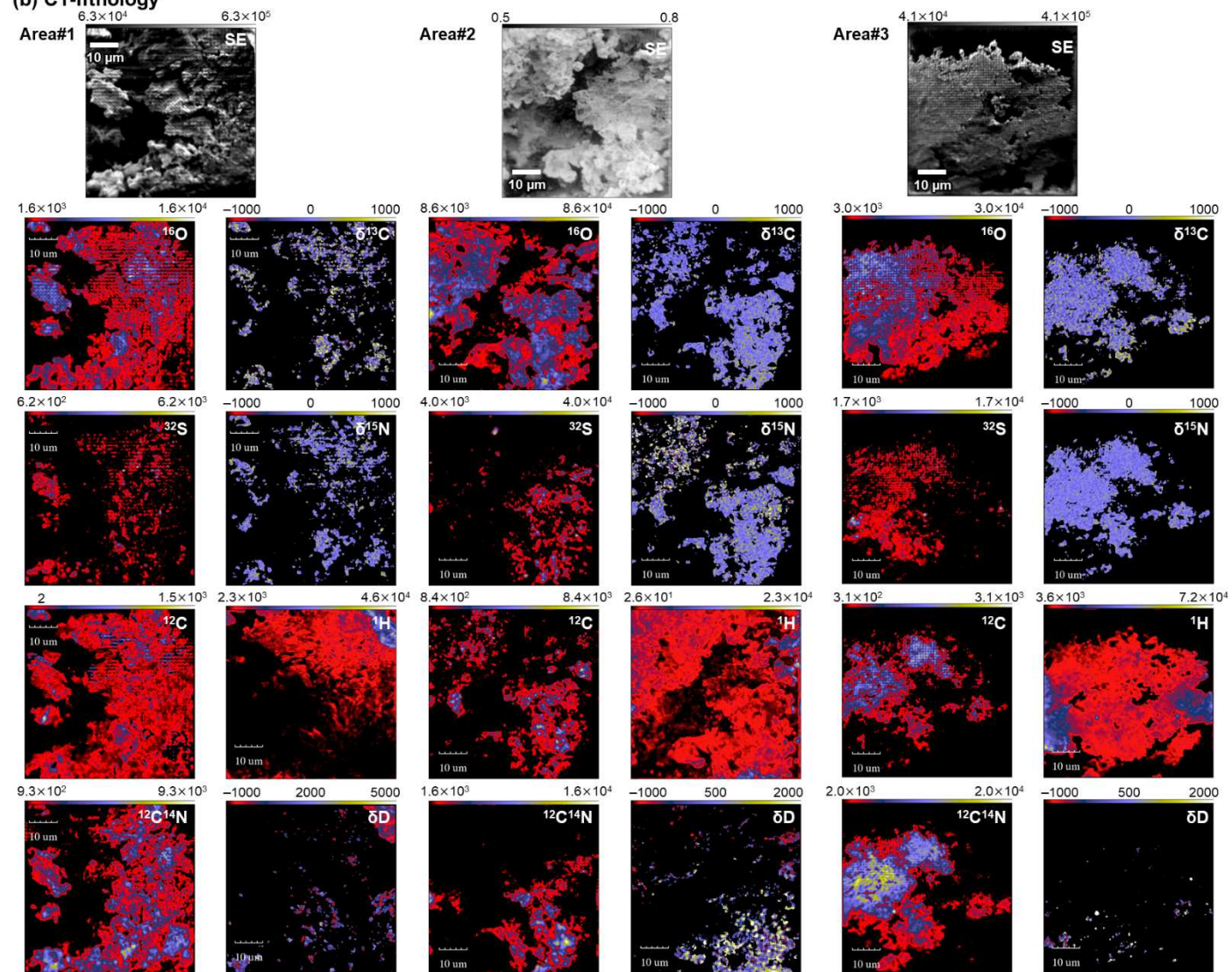


Fig. 20: NanoSIMS secondary ion images and isotopic ratio images of the Aguas Zarcas (a) Met-2 lithology and (b) C1 lithology

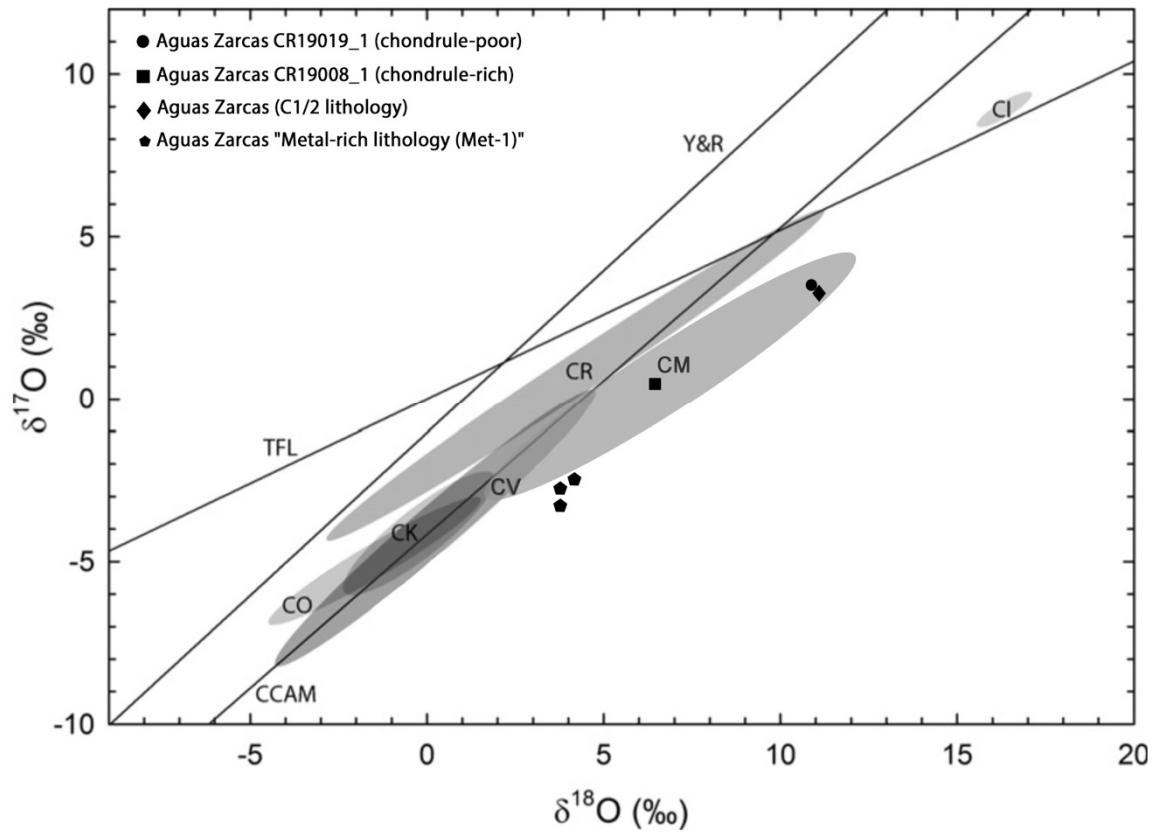
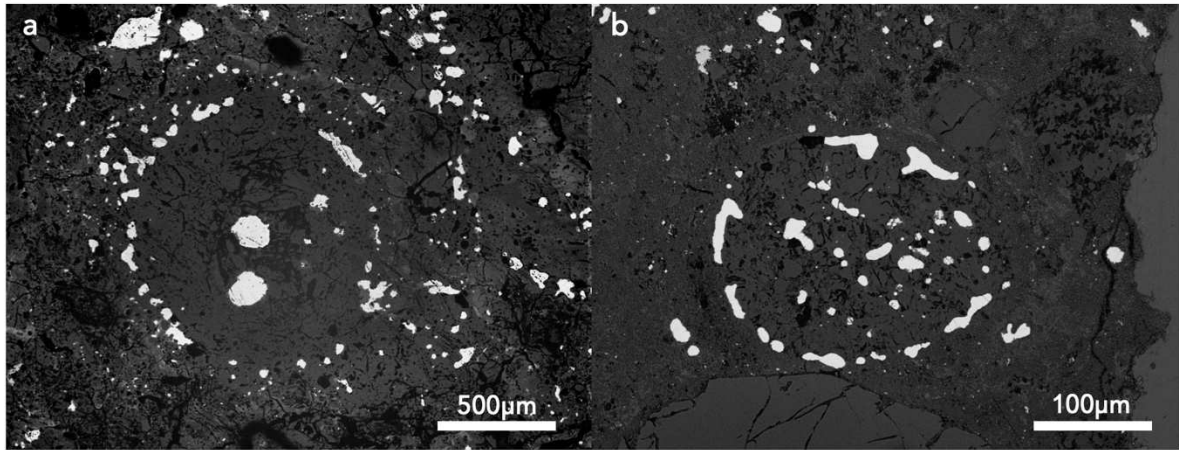


Fig. 21. Three-oxygen isotope diagram showing the isotopic regions of whole rock carbonaceous chondrites from Schrader et al., (2011) updated. The bulk compositions of the different Aguas Zarcas lithologies (data from Kerraouch et al., 2021) are shown with different symbols. CR chondrites data from Schrader et al., (2011) and CM chondrites data from Torrano et al., (2021). Terrestrial fraction line (TFL), Carbonaceous chondrite anhydrous mineral (CCAM) line, and Young and Russell (Y&R) line plotted for reference.



1692

1693 Fig 22. (a) Chondrule from CR chondrite Acfer 209 (reflected light) in comparison with (b)  
1694 chondrule from Met-1 lithology of Aguas Zarcas (reflected light) showing similarity between  
1695 the metal-rich lithology (Met-1) and CR chondrites. Both chondrules surrounded by metal  
1696 with some metal grains inside as well.

1697

1698 **Tables:**

1699 Table 1: Summary of the different lithologies of Aguas Zarcas studied here with their applied analysis.

<i>Fragment</i>	<i>MS-2</i>	<i>CR19.01</i>	<i>CR19.19</i>	<i>MS-2/CR19.01</i>	<i>CR19.29</i>
<i>Lithology</i>	Met-1	Met-2	CM1/2	CM	C1
<i>SEM/EPMA</i>	✓	✓	✓	✓	✓
<i>XRD</i>	✓	✗	✗	✗	✗
<i>H<sub>2</sub>O/CO<sub>2</sub></i>	✓	✗	✗	✗	✗
<i>SIMS (O)</i>	✓	✗	✓	✓	✗
<i>ICPMS</i>	✓	✓	✗	✗	✗
<i>Ti isotopes</i>	✓	✓	✗	✗	✗
<i>Cr isotopes</i>	✓	✓	✗	✗	✗
<i>Te isotopes</i>	✓	✗	✗	✗	✗
<i>Organic matter</i>	✓	✓	✓	✓	✓
<i>SOM</i>	✓	✗	✗	✗	✗
<i>Raman</i>	✗	✓	✗	✓	✓
<i>FTIR</i>	✗	✓	✗	✓	✓
<i>AFM-IR with Raman</i>	✗	✗	✗	✓	✗
<i>STXM/C-XANES</i>	✗	✓	✗	✓	✓
<i>NanoSIMS</i>	✗	✓	✗	✗	✓

1701 Table 2: General characterization of the different lithologies of Aguas Zarcas.

	<i>Met-1</i>	<i>Met-2</i>	<i>CM1/2</i>	<i>CM</i>	<i>C1</i>
<i>Metal and sulfides (vol.%)</i>	3	5	<1	<1	Few $\mu$ m-sized sulfides
<i>Average chondrule sizes (<math>\mu</math>m)</i>	186	136	256	~270	-
<i>Chondrule abundance (vol.%)</i>	30	20	15	20	-
<i>Matrix abundance (vol.%)</i>	55	70	80	~70	~90
<i>CAIs abundance (vol.%)</i>	0.66	-	<1	<1	-
<i>Accretionary rims</i>	present	absent	Present	present	-
<i>Olivine</i>	Fa <sub>0-65</sub>	Fa <sub>0-50</sub>	Fa <sub>0-53</sub>	Fa <sub>0-60</sub>	-
<i>Pyroxene</i>	Fs <sub>0-17</sub> En <sub>60-99</sub>	Fs <sub>0-17</sub> En <sub>60-99</sub>	Fs <sub>10.8</sub> En <sub>60</sub>	Fs <sub>~2</sub> En <sub>~60</sub>	-
<i>TCIs (alteration index)</i>	2.5	-	2.2	2.6-2.8	-

1702



Table 3: The bulk chemical composition of Met-1 and CM1/2 lithologies compared to those of Flensburg (Bischoff et al., 2021) and the average compositions of other CM and CR chondrites (Braukmüller et al., 2018). Oxides are given in wt%; all other element concentrations in ppm ( $\mu\text{g/g}$ ).

ICP-SFMS (wt.%)					
	Met-1	CM1/2	Flensburg	CM*	CR *
<b>TiO<sub>2</sub></b>	0.10	0.10	0.09	0.09	
<b>Al<sub>2</sub>O<sub>3</sub></b>	2.35		2.20	2.25	
<b>FeO</b>	31.21		27.40	28.30	
<b>MnO</b>	0.23		0.22	0.23	
<b>MgO</b>	20.37		19.70	20.10	
<b>CaO</b>	1.87	1.52	1.82	1.76	
<b>Na<sub>2</sub>O</b>	0.69		0.64	0.36	
<b>K<sub>2</sub>O</b>	0.05		0.05	0.05	
<b>P<sub>2</sub>O<sub>5</sub></b>	0.25		0.23	0.23	
ICP-MS (ppm)					
<b>Li</b>	0.000	1.230	-	-	-
<b>Be</b>	0.026	0.031	-	-	-
<b>Sc</b>	2.522	7.472	8.37	-	-
<b>V</b>	66.88	62.97	65.40	67.30	72.90
<b>Mn</b>	1720.7	1495.4	1568.0	1775.0	1834.0
<b>Co</b>	566.9	511.6	536.0	597.0	644.0
<b>Zn</b>	158.3	149.9	154.0	197.0	
<b>Rb</b>	1.634	1.211	1.700	1.600	1.040
<b>Sr</b>	8.752	7.035	10.330	-	-
<b>Y</b>	2.185	1.901	2.260	-	-
<b>Zr</b>	4.968	4.291	4.910	4.730	5.060
<b>Nb</b>	0.377	0.388	0.375	0.368	0.439
<b>Cs</b>	0.101	0.095	0.119	0.119	0.059
<b>Ba</b>	2.932	2.773	3.240	2.980	3.100
<b>La</b>	0.331	0.292	0.343	0.290	0.295
<b>Ce</b>	0.850	0.748	0.876	0.758	0.790
<b>Pr</b>	0.126	0.112	0.131	0.122	0.132
<b>Nd</b>	0.640	0.559	0.661	0.624	0.691
<b>Sm</b>	0.206	0.180	0.215	0.204	0.233
<b>Eu</b>	0.078	0.069	0.081	0.077	0.086
<b>Gd</b>	0.290	0.226	0.296	0.321	0.347
<b>Tb</b>	0.055	0.043	0.055	0.052	0.057
<b>Dy</b>	0.376	0.293	0.296	0.351	0.382
<b>Ho</b>	0.081	0.065	0.082	-	-
<b>Er</b>	0.237	0.192	0.240	0.221	0.245

<b>Tm</b>	0.036	-	0.038	0.035	0.039
<b>Yb</b>	0.226	0.204	0.235	0.229	0.266
<b>Lu</b>	0.035	0.029	0.035	0.035	0.038
<b>Hf</b>	0.153	0.119	0.152	0.139	0.152
<b>Ta</b>	0.020	0.015	0.019	-	-
<b>Pb</b>	1.233	1.112	1.166	1.500	0.466
<b>Th</b>	0.033	0.029	0.043	0.037	0.040
<b>U</b>	0.010	0.008	0.010	0.009	0.010

1707

1708 \* Median CM data (n=14) of Braukmüller et al., (2018).



1709     Table 4: Ti, Cr, and Te isotopic compositions of the Met-1 and CM1/2 lithologies of Aguas Zarcas.

Sample	Weight (mg)	N (Ti)	$\epsilon^{46}\text{Ti}$	( $\pm 2\sigma$ )	$\epsilon^{48}\text{Ti}$	( $\pm 2\sigma$ )	$\epsilon^{50}\text{Ti}$	( $\pm 2\sigma$ )	N (Cr)	$\epsilon^{53}\text{Cr}$	( $\pm 2\sigma$ )	$\epsilon^{54}\text{Cr}$	( $\pm 2\sigma$ )	Te (ng/g)	( $\pm 2\sigma$ )	$\delta^{128/126}\text{Te}$	( $\pm 2$ s.d.)
CM1/2	48.2	13	0.54	0.09	-0.04	0.05	3.02	0.07	5	0.07	0.17	0.97	0.11	-	-	-	-
Met-1	15.4	12	0.55	0.08	0.00	0.04	2.57	0.11	6	0.19	0.11	1.05	0.18	1387	35	0.08	0.02

1710

1711 Table 5: Average isotopic compositions of the entire analyzed regions and C-rich regions in the Aguas Zarcas Met-2 and C1 lithologies obtained by NanoSIMS.

		$\delta^{13}\text{C}$ (‰)	$\delta^{15}\text{N}$ (‰)	$\delta\text{D}$ (‰)
<i>Met-2</i>				
Area#1	Entire	11.7 ± 5.7	25.0 ± 5.3	14 ± 11
	C-rich	14.5 ± 6.7	17.7 ± 7.2	104 ± 24
	$\delta^{13}\text{C}$ -anomalous	2108 ± 305	166 ± 294	
Area#2	Entire	8.0 ± 4.3	15.8 ± 3.7	16 ± 13
	C-rich	10.8 ± 4.2	38.9 ± 4.4	71 ± 31
Area#3	Entire	-29.6 ± 3.8	41 ± 13	
	C-rich	-31.5 ± 4.7	42 ± 17	
	N-rich	-12.3 ± 7.7	48.4 ± 8.3	
	$^{15}\text{N}$ -hotspot #1	46.7 ± 31.4	791.9 ± 95.4	
	#2	-6 ± 32	505 ± 123	
	#3	-153 ± 63	636 ± 141	
	#4	166 ± 131	577 ± 161	
	#5	49 ± 55	464 ± 97	
<i>C1 lithology</i>				
Area#1	C-rich	-30.7 ± 10.1	-10.2 ± 9.3	87 ± 7
Area#2	C-rich	-19.5 ± 4.4	-7.8 ± 8.2	72 ± 6
Area#3	C-rich	-43.2 ± 4.1	-11.3 ± 2.1	18 ± 5

1712 \*errors are 1 $\sigma$

## 1713    **Electronic Annex - Supplemental Materials**

### 1714    **Electron microscopy and Electron microprobe analysis (EPMA)**

1715    The samples were characterized by SEM/EDS at the E-Beam Laboratories of the NASA  
1716    Johnson Space Center and at the Institut für Planetologie (IfP), University of Münster. We  
1717    used a JEOL 6610-LV electron microscope (SEM) at the Interdisciplinary Center for Electron  
1718    Microscopy and Microanalysis (ICEM) at the University of Münster was used to study the  
1719    petrography and mineralogy of some samples. For quantitative analysis, samples and  
1720    appropriate mineral standards were measured at an excitation voltage of 20 kV, and the beam  
1721    current constancy was controlled by a Faraday cup. The attached EDS system was used for  
1722    chemical characterization and analyses of the different mineral constituents (e.g., silicates,  
1723    sulfides, and metals). Olivine (Mg, Fe, Si), jadeite (Na), plagioclase (Al), sanidine (K),  
1724    diopside (Ca), rutile (Ti), chromium-oxide (Cr), rhodonite (Mn), Co-metal (Co), and  
1725    pentlandite (Ni, S) were used as natural and synthetic standards. We used the INCA analytical  
1726    program provided by Oxford Instruments for these analyses.

1727    Some samples were imaged and analyzed at Astromaterials Research and Exploration Science  
1728    (ARES) Office, NASA JSC (Houston), using a JEOL 7600-FE scanning electron microscope  
1729    and JEOL 8530-FE electron microprobe. Natural mineral standards were used. Raman  
1730    analyses were performed using the Ratatoskr instrument at ARES, which is a WITec alpha-  
1731    300R customized for Raman imaging at square-centimeter scales. Analyses were performed  
1732    using a 488 nm excitation laser.

1733    Most quantitative mineral analyses were obtained using a JEOL JXA 8530F electron  
1734    microprobe (EPMA) at the Institut für Mineralogie (University of Münster), which was  
1735    operated at 15 kV and a probe current of 15 nA. These natural and synthetic standards were  
1736    used for wavelength dispersive spectrometry: jadeite (Na), kyanite (Al), sanidine (K),  
1737    chromium oxide (Cr), San Carlos olivine (Mg), hypersthene (Si), diopside (Ca), rhodonite  
1738    (Mn), rutile (Ti), fayalite (Fe), apatite (P), celestine (S), and NiO (Ni).

1739    For analyses of the fine-grained materials (tochilinite-cronstedtite intergrowths (TCIs),  
1740    matrix, dust rims) of the Met-1 and brecciated CM lithologies of Aguas Zarcas the  
1741    concentrations of the following elements were obtained: Na, K, S, Mg, Al, Si, P, Ca, Cr, Ti,  
1742    Mn, Fe, Co, Ni. Oxygen was measured separately and calculated later for each element as an

oxide in wt% for comparison. The analyses were done with variable spot sizes between 5–20  $\mu\text{m}$  depending on the different sizes of TCIs and rims.

Additional quantitative mineral analyses were obtained using a JEOL JXA 8530F electron microprobe (EPMA) were made at 15kV and 20nA at the ARES E-Beam Laboratories.

#### **Modal Analysis by X-ray Diffraction**

Mineral phases in Met-1 were initially characterised using a PANalytical X'Pert Pro scanning X-ray diffractometer (XRD) at the Natural History Museum (NHM), London. Approximately 1 mg of powdered sample was mixed with acetone and smeared onto a zero-background substrate. XRD patterns were then collected from the sample using Co  $K\alpha$  radiation from 5 - 70° (2 $\theta$ ) with a step size of 0.02° and time/step of 0.5 seconds. The mineral phases in the sample were identified by comparing diffraction peaks to the International Centre for Diffraction Data (ICDD) database (PDF-2).

The modal mineralogy of a ~50 mg powdered aliquot of Met-1 was determined using an Enraf-Nonius PDS120 XRD with an INEL curved 120° position-sensitive-detector (PSD) in a static geometry relative to the primary X-ray beam and sample. The X-ray beam (Cu  $K\alpha_1$  radiation) was restricted to 0.24  $\times$  2.00 mm and set at an incident angle of 3.4° to the flat top of the sample which was rotated throughout the measurement. The sample of Met-1 was analysed for 16 hours, while standards of minerals known to be present in the meteorite were analysed under the same experimental conditions for 15 minutes. Mineral abundances were calculated using a profile-stripping method, previously applied to CM chondrites, where the intensities of the mineral standard diffraction patterns were scaled to match the meteorite pattern and then subtracted to produce a residual with zero counts (e.g Howard et al., 2009, 2015; King et al., 2017).

#### **Oxygen isotopes by SIMS**

Oxygen and Mn-Cr isotope compositions in calcite and spinel were determined using the Cameca IMS1280-HR ion microprobe at Heidelberg University (HIP). For oxygen isotopes we used a ~ 1.3 nA, 20 keV  $\text{Cs}^+$  primary ion beam with a raster size of 6  $\mu\text{m}$  (8  $\mu\text{m}$  during pre-sputtering). Negative secondary ions were accelerated to 10 keV. The secondary ion image was limited to 15  $\mu\text{m}$ , the dynamic transfer optical system (DTOS) was activated and sample charging was compensated with the electron gun (NEG).  $^{16}\text{O}$ ,  $^{17}\text{O}$  and  $^{18}\text{O}$  were detected simultaneously in three Faraday cup detectors. The nominal mass resolving power for  $^{16}\text{O}$  and  $^{18}\text{O}$  was 2500 and 7000 for  $^{17}\text{O}$ . The contribution of  $^{16}\text{OH}^-$  on the  $^{17}\text{O}$  peak was

negligible at  $< 0.1\text{‰}$ . Secondary intensities for  $^{16}\text{O}$  and  $^{17}\text{O}$  were  $\sim 1.5 \times 10^9$  cps and  $\sim 6 \times 10^5$  cps, respectively. Prior to each analysis the secondary beam was centered automatically in the field aperture (X and Y) and the entrance slit (X only). Including the time for beam centering the analyses started after a total pre-sputtering time of 90 s and each analysis had 25 cycles with 8 s integration time per cycle. The internal precision reported is the standard deviation of the mean value of the isotope ratios. The baseline of the Faraday cup amplifiers was determined separately with an integration time of 200 s several times per session.

NBS19 limestone (NIST RM 8544,  $\delta^{18}\text{O}_{\text{VSMOW}} = +28.65\text{‰}$ , Brand et al., 2014) was used as reference material for the calibration of the calcite oxygen isotope analyses. For  $\delta^{17}\text{O}_{\text{VSMOW}}$  we assumed a value of  $+14.85\text{‰}$  which was calculated using the mean  $\Delta^{17}\text{O}$  value from Passey et al., (2014) and Barkan et al., (2015). The reference material was on a separate sample holder and was analysed prior to and during the analytical session. The spinel analyses were calibrated *post hoc* using a Burma spinel with  $\delta^{18}\text{O}_{\text{VSMOW}} = +28.39\text{‰}$  and  $\delta^{17}\text{O}_{\text{VSMOW}} = +14.77\text{‰}$  (laser fluorination data). The repeatability (1sd) for  $\delta^{17}\text{O}$ ,  $\delta^{18}\text{O}$  and  $\Delta^{17}\text{O}$  of the calcite calibration was  $0.33\text{‰}$ ,  $0.14\text{‰}$  and  $0.34\text{‰}$ , respectively. For spinel, the repeatability (1sd) was  $0.63\text{‰}$ ,  $0.09\text{‰}$  and  $0.61\text{‰}$ , respectively.

## **Water contents and C-concentrations**

The analyses of the water contents and C-concentrations were performed only for the Met-1 (Metal-rich lithology-1).

Water analysis of the Met-1 was performed at the Institute for Geology, Mineralogy and Geophysics, Ruhr-University Bochum using a Mitsubishi CA 200 moisturemeter. For three analyses about 3 mg of the crushed sample were heated in an HF-oven to  $1000\text{ °C}$ ; the gaseous components were then conducted into the titration cell where the water content was measured by the Karl-Fischer-method. The instrument was tested with an internal laboratory standard (5 wt%  $\text{H}_2\text{O}$ ) prior and after the measurements. The precision of this method is 5 % relatively.

Determination of the  $\text{CO}_2$  content was done using the C/S 500 instrument of ELTRA with an IR-detector. A sample of 23 mg was heated in an oxygen atmosphere up to  $1100\text{ °C}$ . All carbon present reacts to form  $\text{CO}_2$  which is transported in an oxygen flow towards the detector ( $\text{C}_{\text{total}}$ ).

1806 **Bulk chemical analysis**

1807 Two samples of the meteorites Aguas Zarcas, one from the Met-1 of about 0.2 g, and the  
1808 second from CM1/2 lithology were crushed and homogenized. The chemical composition of  
1809 the bulk samples were obtained by using ICP-AES (for Al, Fe, Mn, Mg, Na, Cr, Co, and Ni)  
1810 and ICP-SFMS. The bulk compositions using ICP were performed at the Institut Universitaire  
1811 Européen de la Mer, Université de Bretagne Occidentale in Plouzané, France.

1812 **Titanium, Cr, and Te isotope analyses**

1813 Titanium and Cr isotope measurements were performed on the Met-1 and C1/2 lithology of  
1814 Aguas Zarcas., while the Te isotopic composition was measured only for the Met-1 lithology.

1815 **Titanium isotope analyses**

1816 Powdered aliquots of the CM1/2 (~48.2 mg) and Met-1 (~15.4 mg) lithology were digested in  
1817 HF-HNO<sub>3</sub>-HClO<sub>4</sub> (2:1:0.05) on a hotplate at 180–200 °C for five days and in aqua regia  
1818 (HCl-HNO<sub>3</sub>) at 130–150 °C for another two days. Thereafter, the samples were dissolved in  
1819 12 M HNO<sub>3</sub>, and ~65 mg H<sub>3</sub>BO<sub>3</sub> were added. Ti was separated from the sample matrix via a  
1820 two-stage anion exchange chromatography adapted from the previously established procedure  
1821 from Zhang et al., (2011). In a first step, the sample solutions were loaded onto columns  
1822 prepacked with 2 ml TOGDA<sup>®</sup> anion exchange resin, where Ti was eluted in 20 ml 12 M  
1823 HNO<sub>3</sub>–1 wt.% H<sub>2</sub>O<sub>2</sub>. Afterwards, the Ti cuts were dissolved in 2.5 ml 4 M HF and loaded  
1824 onto clean-up columns filled with 0.8 ml Bio-Rad<sup>®</sup> AG1-X8 anion exchange resin, where Ti  
1825 was eluted in 6 ml 9 M HCl–0.01 M HF.

1826 Titanium isotope measurements were performed in two lines using a Thermo Scientific<sup>®</sup>  
1827 Neptune Plus MC-ICPMS in high resolving power mode (Zhang et al., 2011). Solutions  
1828 containing about 600 ppb Ti in 0.3 M HNO<sub>3</sub> – 0.0014 M HF were introduced through a Cetac  
1829 Aridus II desolvating system, resulting in a  $\sim 3.5 \times 10^{-10}$  A ion beam on <sup>48</sup>Ti. Measurements  
1830 consisted of a 30 s baseline measurement (deflected beam) followed by 40 isotope ratio  
1831 measurements of 4.2 s each. Mass bias was corrected using the exponential law and <sup>49</sup>Ti/<sup>47</sup>Ti  
1832 = 0.749766. The Ti isotope anomalies are reported as parts per ten thousand deviation (ε-  
1833 notation) from the terrestrial OL-Ti bracketing standard (Millet and Dauphas, 2014). The  
1834 sample uncertainty is reported as the Student-t 95% confidence interval (95% CI) based on  
1835 repeated analyzes of the sample solution.

## 1836 **Chromium isotope analyses**

1837 Chromium was collected during the first step of the two-stage anion exchange  
1838 chromatography used for the separation of Ti, where Cr is eluted in 25 ml 12 M HNO<sub>3</sub> (+  
1839 trace H<sub>3</sub>BO<sub>3</sub>) together with most other matrix elements. Aliquots (equivalent to ~30 µg Cr)  
1840 were taken from this solution, dried down, and redissolved in 1 ml 6 M HCl.

1841 Afterwards, Cr was separated from the sample matrix using a single-stage anion exchange  
1842 chemistry for the removal of Fe (Bio-Rad® AG1-X8 anion exchange resin), followed by a  
1843 two-stage cation exchange chromatography (Bio-Rad® AG50W-X8 cation exchange resin) as  
1844 described by Schneider et al., (2020), including a four-day conversion of Cr[III]Cl<sub>3</sub>/Cr[II]Cl<sub>2</sub>  
1845 to Cr<sup>3+</sup>.

1846 Chromium isotope measurements were performed using a Thermo Scientific® Triton Plus  
1847 Thermal Ionization Mass Spectrometer in static mode. The sample solutions (containing ~500  
1848 ppm Cr in 6 M HCl) were loaded on 4-6 filaments and each filament was measured multiple  
1849 times, with total ion beam intensities of  $\sim 1.4 \times 10^{-10}$  A on <sup>52</sup>Cr. Instrumental mass fractionation  
1850 was corrected assuming a constant <sup>50</sup>Cr/<sup>52</sup>Cr = 0.051859 and using the exponential law. The  
1851 data are reported in ε<sup>i</sup>Cr values (*i* = 53, 54) as the parts per ten thousand deviation from the  
1852 terrestrial NIST SRM3112a Cr standard. The sample uncertainty is reported as the Student-t  
1853 95% confidence interval (95% CI) based on repeated analyses.

## 1854 **Organic matter**

1855 We studied organic matter in four lithologies of Aguas Zarcas, but with different methods. A  
1856 small fragment of Met-1 was sent to the Research Center for Environmental Health,  
1857 Muenchen, German, and has been studied by Soluble organic matter analysis method. Met-2,  
1858 C1 lithology and CM chondrite lithology, have been studied by a combination of several  
1859 methods in Japan at the Faculty of Engineering, Division of Materials Science and Chemical  
1860 Engineering, Yokohama National University and the Japan Agency for Marine-Earth Science  
1861 Technology (JAMSTEC), in collaboration with other laboratories in other countries. But the  
1862 results were all consistent.

## 1863 **Soluble organic matter analysis**

1864 The soluble organic matter (SOM) was analyzed following the same procedures used  
1865 previously to enable a comparison of the compositional profiles (Schmitt-Kopplin et al., 2010;

Popova et al., 2013), and the data were obtained from solid specimen with a weight of a very few mg. The small fragment Aguas Zarcas CM chondrite (pre-rain and post-rain) as well of its metal-rich lithology (Met-1) were washed with LC/MS grade methanol (Fluka) to remove surface contamination; this washing fluid was discarded. All fragments were consecutively crushed and ground in an agate mortar with an agate pestle for ~20 sec under 400 $\mu$ l LCMS grade methanol. The solutions were centrifuged at 16000 rpm for 3 minutes. The obtained supernatant was directly used for ultra-high resolution mass spectrometry as described initially (Schmitt-Kopplin et al., 2010). Briefly we used a Bruker Solarix 12 Tesla Fourier transform (FT) ion cyclotron resonance (ICR) mass spectrometer (MS) located at the Helmholtz Zentrum, Munich, Germany. The resolution ( $> 400,000$  at  $m/z$  400) and the mass error ( $< 0.2$  ppm) were sufficiently precise to compute exact molecular formulae in the C, H, O, N, S, Mg space. The van Krevelen or elemental diagrams were used to visualize the chemical space of FT-ICR MS data by plotting assigned molecular formulas according to their hydrogen to carbon (H/C),  $m/z$  and oxygen to carbon (O/C) ratios.

## **Raman spectroscopy**

Raman analysis and peak fitting were conducted following the procedure described in Kiryu et al., (2020). The samples were pressed on clean Au or KBr substrates and analyzed using a Raman microspectrometer (RAMANtouch; Nanophoton) at JAMSTEC, Yokosuka, with a 532 nm laser. The spot size was  $<1 \mu\text{m}$  using a 100 $\times$  objective with the numerical aperture of 0.90, and the laser power at the sample surface was  $<700 \mu\text{W}$ . The spectral range was 100–2600  $\text{cm}^{-1}$  with a 600 grooves/mm grating. The exposure time for each spectrum was 20 s and two accumulations were obtained for each analytical spot to permit discarding of cosmic ray events in the detector. At least 10 spectra were collected at carbon-rich regions from each sample. The Raman shift was calibrated daily using a silicon wafer prior to analyses. The peak positions, the FWHM, and the peak intensity ratio ( $I_D/I_G$ ) of D and G bands ( $\sim 1355 \text{ cm}^{-1}$  and  $\sim 1585 \text{ cm}^{-1}$ , respectively) were determined by peak fitting to the Lorentzian and BWF (Breit–Wigner–Fano), respectively—so called L–BWF model Ferrari and Robertson (2000)—with a linear baseline correction between 900–1800  $\text{cm}^{-1}$ .

Raman mapping measurements were also performed on the same microtome section as the one used for AFM-IR measurements (see AFM-IR section), using a DXR Raman microspectrometer, with a laser at 532 nm at 500  $\mu\text{W}$  power. The calibration was achieved on a silicon wafer, and checked to be within 1  $\text{cm}^{-1}$  with a diamond feature at 1332  $\text{cm}^{-1}$  for measurements on the diamond substrate. A  $\times 100$  objective with a numerical aperture of 0.90



1899 was used to map a rectangle area of 11 microns by 43 microns, along the largest dimension of  
1900 the section. A one micron step sampling was used (for a total of 473 spectra covering the  
1901 4000  $\text{cm}^{-1}$  to 150  $\text{cm}^{-1}$  range), each with 2 scans of 10 s per spot; the total integration  
1902 including displacements took slightly less than 3 hours. The spectra were corrected by  
1903 subtracting the relative contribution of the substrate in regions where the sample is partly  
1904 transparent or on the border of the map, recording the substrate surface signal.

## 1905 **IR spectroscopy**

1906 FTIR analysis was conducted following the procedure described in (Kebukawa et al., 2020).  
1907 A small amount of the clast was pressed on KBr plates ( $\sim 5 \times 5 \times 1 \text{ mm}^3$ ). IR absorption  
1908 spectra were collected using a micro-FTIR (JASCO FT/IR-6100+IRT-5200), equipped with a  
1909 ceramic IR light source, a germanium-coated KBr beam splitter, a mercury-cadmium-telluride  
1910 (MCT) detector, and  $\times 16$  Cassegrain mirrors, at Yokohama National University. A total of  
1911 256-512 scans of IR transmission spectra were accumulated with a wavenumber resolution of  
1912 4  $\text{cm}^{-1}$ , in the wavenumber range of 7000-400  $\text{cm}^{-1}$ , with a  $20 \times 20 \text{ }\mu\text{m}^2$  aperture. For the  
1913 mapping measurements, A total of 64 scans of IR transmission spectra were accumulated with  
1914 a wavenumber resolution of 8  $\text{cm}^{-1}$ , with a  $50 \times 50 \text{ }\mu\text{m}^2$  aperture at each point. Background  
1915 spectra were acquired through blank areas of the KBr adjacent to the samples.

## 1916 **AFM-IR**

1917 Sulfur embedded ultramicrotomed thin-sections from CM lithology (CR19-001) were  
1918 prepared for AFM-IR. A meteorite grain was embedded in a molten (115°C) sulfur droplet  
1919 with a glass needle. The sulfur droplet subsequently solidified and was then attached onto an  
1920 epoxy stub using glue. The sulfur droplet was sliced into  $\sim 100 \text{ nm}$ -thick sections with a Leica  
1921 ultramicrotome using a DIATOME diamond knife. The sections were floated onto deionized  
1922 water and transferred to a diamond substrate (Diamond Express II, S. T. Japan).

1923 We performed AFM-IR analysis using a NanoIR2 system from Bruker. In this setup, the IR  
1924 beam was focused on the topside of the sample onto the AFM cantilever. The system was  
1925 coupled to a multi-chip quantum cascade laser source (MIRcat, Daylight Solutions; tunable  
1926 repetition rates range of 0–2 MHz; spectral resolution of 0.1  $\text{cm}^{-1}$ ) that covers a portion of the  
1927 mid-IR range, from 1900  $\text{cm}^{-1}$  to 900  $\text{cm}^{-1}$ . The data were acquired using the tapping AFM-  
1928 IR mode described in Mathurin et al., (2018). The probes used were tapping AFM-IR  
1929 cantilever with a resonance frequency at 75 kHz, gold-coated to avoid artifact effects due to  
1930 the silicon IR absorption. The IR-mapping acquisition parameters were 0.2 Hz scan rate and a

3.33 nm step size for all wavenumbers. The AFM-IR maps were recorded at several selected frequencies, targeted to sample organics (1710 and 1600  $\text{cm}^{-1}$ ) and silicates (1020 and 960  $\text{cm}^{-1}$ ). Composite two colour maps combining the 1600  $\text{cm}^{-1}$  and 1020  $\text{cm}^{-1}$  maps were built to compare the spatial distribution of organics and silicates. Before combining them, individual images were realigned to compensate for possible small drifts between consecutive AFM-IR map recordings. The realigning was done using an algorithm maximising the spatial correlation on the topography of the sample. Because the silicate signal is dominating in absolute intensity, and thus contrast, each colour image was normalized by setting the maximum signal to unity before combining them. Local spectra were acquired at a fixed position by tuning the laser at the different wavenumbers covering 1900  $\text{cm}^{-1}$  to 900  $\text{cm}^{-1}$  with a 1  $\text{cm}^{-1}$  step. Spectra presented here are average of eight individuals spectra obtained at each position.

#### **FIB for STXM**

We have chosen typical area in matrix of Aguas Zacas for preparing ultra-thin sections utilizing two FIBs (Hitachi Tech SMI-4050 and SMJ-4000L) at the Kochi Institute of Core Sample Research, JAMSTEC. The sections ( $\sim 10 \times 10 \times 0.1 \mu\text{m}$ ) were extracted using an FIB SMI-4050 with a Ga<sup>+</sup> ion beam at 30 kV then finished with lower accelerating voltage of 5 kV. These sections were mounted on a commercial FIB grid. Subsequently, the sections were transferred into an FIB-SEM SMJ-4000L to remove damaged layers on surface of the sections with broad Ar-ion beam at 1 kV (Kodama et al., 2020).

#### **STXM**

Carbon X-ray absorption near-edge structure (C-XANES) analyses were performed using the scanning transmission X-ray microscopes (STXM) at BL-13A of the Photon Factory, High Energy Accelerator Research Organization (KEK) (Takeichi et al., 2016) and BL4U at UVSOR Synchrotron (Ohigashi et al., 2013). Measurement conditions were mostly similar to these described in Kebukawa et al., (2019b); Kebukawa et al., (2020). The elemental maps were obtained by acquiring pairs of images below ( $I_L$ ) and on the absorption edges ( $I_H$ ), at 280 and 292 eV, respectively for C *K*-edge, 525 eV and 539 eV for O *K*-edge, and 705 eV and 709 eV for Fe *L*<sub>3</sub>-edge, with a dwell time of 5 ms, and taking the  $-\ln(I_H/I_L)$  for each pixel, with 0.1-0.2  $\mu\text{m}$  steps per pixel. The C *K*-edge-XANES spectra were acquired with the energy step sizes ( $\Delta E$ ) of 0.1 eV in 283-295.5 eV region, 0.5 eV in 280-283 eV and 295.5-301.0 eV regions, and 1 eV in 301-320 eV region, with a dwell time of 3-7 ms and 0.1-0.2  $\mu\text{m}$  steps per

1963 pixel. Three-point smoothing was applied to the raw C-XANES spectra to reduce noises.  
1964 STXM/XANES data analysis was performed using a software aXis2000  
1965 (<http://unicorn.mcmaster.ca/aXis2000.html>).

## 1966 **NanoSIMS**

1967 Small fragments Met-2 of Aguas Zarcas were pressed on Au thin foil. Matrix areas on the thin  
1968 sections were chosen for analysis by a raster ion imaging with the JAMSTEC NanoSIMS 50L  
1969 at Kochi Institute for Core Sample Research, JAMSTEC. A typical measurement involved  
1970 rastering a focused positive Cs primary beam ( $\sim 200$  nm $\phi$ ,  $\sim 3$  pA) across  $56 \times 56$  or  $60 \times 60$   
1971  $\mu\text{m}^2$  areas ( $512 \times 512$  pixels) for 20 cycles with an acquisition time of 5 ms/pixel (1,310  
1972 sec/frame). The  $^{12}\text{C}$ ,  $^{13}\text{C}$ ,  $^{16}\text{O}$ ,  $^{12}\text{C}^{14}\text{N}$ ,  $^{12}\text{C}^{15}\text{N}$  and  $^{32}\text{S}$  were measured as negative secondary  
1973 ions simultaneously in six electron multipliers. Secondary electrons were detected along with  
1974 the secondary ions. The ion images allow for the regions of organic matter in the fragment as  
1975 well as their C and N isotopic ratios. The  $^{16}\text{O}$  enable the outline of silicates or oxides in the  
1976 fragment.

1977 In a separate analysis, the H isotopes ( $^1\text{H}$  and  $^2\text{D}$ ) and  $^{12}\text{C}$  were subsequently measured as  
1978 negative secondary ions together with secondary electron. A focused Cs<sup>+</sup> primary beam  
1979 ( $\sim 200$  nm $\phi$ ,  $\sim 3$  pA) was rastered over  $50 \times 50$  or  $60 \times 60$   $\mu\text{m}^2$  areas and  $512 \times 512$  pixel  
1980 images were acquired for 20 cycles with an acquisition time of 5 ms/pixel (1,310 sec/frame).

1981 Each measurement was only started after stabilization of the secondary ion intensities  
1982 following a pre-sputtering procedure of approximately 10 min. The sample was coated with a  
1983 10 nm Au thin film to mitigate electrostatic charging on the surface. The final images were  
1984 generated from regions that had statistically enough counts. The OM regions were chosen by  
1985 distributions of  $^{12}\text{C}$  within a section applying 10% threshold of total  $^{12}\text{C}$  ion counts. The H, C  
1986 and N isotopic compositions of organic matter in the measured areas were calculated  
1987 following analytical routines using a standard organic material (1-hydroxybenzotriazole  
1988 hydrate;  $\text{C}_6\text{H}_5\text{N}_3\text{O} \cdot x\text{H}_2\text{O}$ : HOBt) (Ito et al., 2014).

1989    **References**

- 1990    Barkan E., Musan I., and Boaz L. (2015) High-precision measurements of  $\delta^{17}\text{O}$  and  $^{17}\text{O}_{\text{excess}}$   
1991         of NBS19 and NBS18. *Rapid Communications in Mass Spectrometry* **29**, 2219–2224
- 1992    Brand A.B., Coplen T.B., Vogl J., Rosner M., and Prohasa, T., (2014) Assessment of  
1993         international reference materials for isotope-ratio analysis (IUPAC Technical Report).  
1994         *Pure and Applied Chemistry* **86**(3), 425–467
- 1995    Passey B. H., Hu, H., Ji, H., Montanari S., Li, S., Henkes, G.A., Levin, N.E., (2014) Triple  
1996         oxygen isotopes in biogenic and sedimentary carbonates. *Geochim. Cosmochim. Acta*  
1997         **141**, 1–25.

1998 **Supplemental Materials** Table S1: Oxygen Isotopic Compositions of Calcite Grains in the  
1999 Met-1 lithology and CM Chondrites (CM-clast1, CM-clast2, CM-clast3 and CM1/2  
2000 lithology).

	$\delta^{17}\text{O}$	2sd	$\delta^{18}\text{O}$	2sd	$\Delta^{17}\text{O}$	MgO	FeO
<b>Met-1 (CAI)</b>							
@0	+16.90	0.5	+36.28	0.6	-2.1	0.87	0.17
@2	+16.70	1.1	+35.88	1.0	-2.1	2.79	0.13
@5	+18.35	0.9	+36.49	0.8	-0.7	0.07	0.06
@8	+15.63	1.1	+33.44	1.6	-1.9	0.13	0.47
@9	+17.78	0.5	+37.45	0.5	-1.8	0.24	0.34
@10	+14.09	1.9	+32.06	2.2	-2.7	0.27	0.51
Mean	+16.6	1.0	+35.3	1.1	-1.9		
2sd	3.1		4.1		1.3		
<b>Met-1 (matrix)</b>							
@11	+18.4	0.6	+37.8	0.4	-1.4	0.05	0.68
@12	+9.2	0.6	+23.8	0.3	-3.3	1.89	5.44
@13	+10.4	0.8	+22.0	0.2	-1.2	0.02	0.80
@14	+8.0	1.0	+16.2	0.4	-0.5	0.00	0.70
@15	+19.4	0.8	+39.8	0.6	-1.4	0.03	0.62
@18	+16.9	0.8	+36.7	0.6	-2.3	0.00	0.56
@19	+9.8	0.6	+20.0	0.3	-0.7	0.01	0.71
@50	+20.4	0.8	+41.6	0.6	-1.3		
@51	+16.3	0.5	+34.9	0.4	-2.0		
@52	+18.5	0.6	+38.9	0.6	-1.9		
@53	+17.4	0.6	+37.2	0.9	-2.1		
@54	+19.5	0.7	+40.1	0.6	-1.5		
@55	+9.8	0.6	+19.2	0.2	-0.3		
@56	+14.7	1.0	+31.8	0.7	-1.9		
@57	+15.4	0.6	+33.4	0.6	-2.1		
@58	+17.6	0.7	+34.5	0.5	-0.5		
@59	+17.5	0.6	+36.8	0.6	-1.7		
@60	+19.4	0.6	+40.9	0.8	-2.0		
@62	+16.4	0.6	+36.5	0.5	-2.7		
@63	+19.9	0.7	+41.5	0.7	-1.8		
@64	+14.5	0.6	+32.8	0.5	-2.7		
Mean	+15.7	0.7	+33.2	0.5	-1.7		
2sd	7.9		16.0		1.5		
<b>CM-Clast2</b>							
@20	+19.3	0.7	+38.8	0.6	-1.0	0.00	0.77
@22	+16.2	0.6	+31.4	0.5	-0.2	0.02	0.93
@23	+17.5	0.8	+34.4	0.5	-0.5	0.05	0.59
@24	+13.6	0.8	+28.3	0.6	-1.3	0.00	1.12
@37	+17.5	0.7	+36.0	0.5	-1.3		
@38	+17.6	0.6	+36.4	0.7	-1.5		
@39	+17.9	0.6	+35.7	0.7	-0.8		
@40	+17.5	0.6	+36.8	0.4	-1.8		
@41	+16.7	0.5	+34.1	0.7	-1.2		
Mean	+17.1	0.6	+34.7	0.6	-1.1		
2sd	3.1		6.3		1.0		
<b>CM-Clast1</b>							
@25	+11.6	0.9	+21.8	0.8	+0.1	0.04	0.99

@26	+16.9	0.5	+34.6	0.4	-1.2	0.00	1.11
@27	+16.5	0.7	+33.0	0.8	-0.8	0.03	0.79
@28	+17.4	0.5	+34.7	0.6	-0.8		
@29	+17.5	0.8	+34.7	0.5	-0.7		
@42	+16.9	0.7	+34.9	0.5	-1.4		
@43	+17.1	0.5	+34.8	0.3	-1.1		
@44	+17.9	0.6	+37.0	0.5	-1.5		
@45	+18.4	0.8	+36.9	0.6	-0.9		
@47	+16.7	0.6	+32.7	0.5	-0.4		
@49	+17.3	0.6	+34.1	0.4	-0.5		
Mean	+16.7	0.6	+33.6	0.5	-0.8		
2sd	3.6		8.2		0.9		

---

**CM-Clast3**


---

@30	+18.6	0.7	+36.6	0.7	-0.5		
@31	+17.5	0.7	+33.4	0.8	+0.0		
@34	+19.1	0.7	+37.6	0.5	-0.6		
@35	+14.1	0.5	+28.6	1.0	-0.9		
@36	+16.6	0.8	+33.6	1.2	-1.0		
Mean	+17.2	0.7	+34.0	0.8	-0.6		
2sd	4.0		7.0		0.8		

---

**CM1/2 lithology**


---

@0	+20.5	0.5	+42.2	0.5	-1.6		
@1	+19.8	0.7	+37.7	0.2	+0.0	0.04	0.97
@2	+20.7	0.5	+40.6	0.6	-0.6	0.08	0.93
@3	+20.6	0.6	+41.9	0.6	-1.2	0.01	0.90
@4	+18.3	0.7	+35.6	0.4	-0.3	0.00	0.89
@5	+11.7	0.8	+27.8	0.7	-2.9	0.01	0.84
@6	+20.2	0.6	+40.1	0.5	-0.8	0.08	0.73
@7	+18.6	0.6	+37.8	0.6	-1.2	0.01	0.79
@8	+18.9	0.6	+37.8	0.3	-0.9	0.08	1.24
@9	+19.2	0.7	+38.3	0.5	-0.9	0.00	0.90
@10	+20.6	0.6	+41.0	0.6	-0.8	0.02	0.67
@11	+16.6	0.6	+31.9	0.6	-0.1	0.04	0.11
@13	+18.7	0.6	+37.5	0.5	-0.9		
@14	+20.2	0.7	+40.4	0.5	-0.9	0.01	0.76
@15	+16.1	0.6	+34.6	0.3	-2.0	0.01	0.85
@16	+16.1	0.7	+32.5	0.9	-1.0	0.12	0.90
@17	+19.1	0.8	+36.0	1.1	+0.3	0.03	1.11
@18	+20.1	0.6	+39.0	0.2	-0.3	0.00	0.90
@19	+14.9	0.8	+30.9	0.6	-1.3	0.05	0.72
@20	+12.7	1.5	+25.2	2.6	-0.5		
@21	+13.5	0.7	+27.1	0.3	-0.7		
@22	+18.8	0.6	+38.1	0.9	-1.1		
@23	+18.2	0.7	+37.7	0.9	-1.5		
@24	+17.1	0.7	+35.1	1.4	-1.3		
@25	+17.8	0.8	+36.2	1.2	-1.2		
@26	+17.2	0.6	+35.0	0.3	-1.2		
@27	+15.4	1.4	+30.4	2.0	-0.5		
@28	+14.7	0.7	+32.7	0.7	-2.4		
@30	+17.2	0.6	+36.8	0.2	-2.0		
@31	+20.6	0.6	+40.3	0.6	-0.5		
@32	+20.2	0.6	+40.3	0.4	-0.9		
@33	+18.4	0.6	+36.4	0.6	-0.7		
@35	+19.2	0.7	+39.8	1.0	-1.6		

@36	+18.7	0.9	+37.7	1.2	-1.1
@37	+11.5	0.6	+25.9	0.3	-2.0
<i>Mean</i>	<i>+17.8</i>	<i>0.7</i>	<i>+35.9</i>	<i>0.7</i>	<i>-1.0</i>
2sd	5.2		9.1		1.4

<b>Spinel</b>					
CAI*	-47.3	1.1	-46.3	0.2	-22.6
CAI*	-49.4	0.9	-50.0	0.2	-22.7
CAI-1	-46.3	0.8	-45.4	0.2	-22.0
CAI-2	-48.6	0.8	-49.1	0.2	-22.3
CAI-3	-44.3	1.1	-41.0	0.3	-22.4
CAI-4	-44.2	0.8	-41.5	0.3	-22.1
<i>Mean</i>	<i>-46.7</i>	<i>0.9</i>	<i>-45.6</i>	<i>0.3</i>	<i>-22.3</i>
2sd	4.3		7.4		0.5

2001

2002